5. Diffusion/Reaction Application

Diffusion of the reactants from the surface of the catalyst to the interior of its pores constitutes one of the resistances in a reaction system catalyzed by the solid surface. In reactor modeling for the reactions with strong diffusion limitations, simplified approaches are selected as described in the Problem Statement. The most frequently used simplifications may be illustrated as the Figure 5.1 for the endothermic reactions.

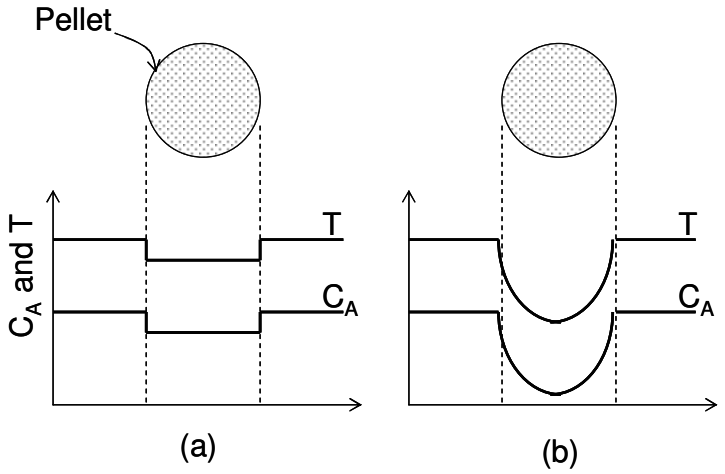

Figure 5.1 Illustration of reactor modeling simplifications for endothermic reactions as: (a) isothermal particle, and (b) uniform and symmetric distributions (re-produced from Levenspiel, 1972).

Isothermal particle, where temperature is constant throughout the particle, can be illustrated as Figure 5.1(a). The uniform and symmetric temperature and composition distributions can be sketched as Figure 5.1(b). These simplifications with the main assumptions such as the usage of lumped transport parameters would be preferable for the high N tubes. However, for the low N tubes where the presence of tube wall has an effect on the large proportion of the entire particles, these simplifications and assumptions would be misleading regarding the strong temperature gradient due to the wall heat flux. Therefore, the objective of this part was to improve the understanding of intra-particle

transport phenomena by explicitly including conduction, species diffusion and reaction with realistic 3D external flow and temperature fields. Regarding the different particle activity levels, as described in Chapter 1, two different endothermic reactions were considered: MSR and PDH.

5.1 Model development

Two types of WS models were selected for this study: a full cylinders packing was used as the generic model, and a 4-hole cylinders packing to represent the commercial interest. The models were re-meshed to implement prism layers on the external and internal surfaces of the particles, including the tube wall. The fluid side prism structure was the one used in Case-c, described in section 4.1.1.2, and the solid side prism layers covered at least 3% of the particle radius from the surface. The mesh specifications for full cylinders and 4-hole cylinders packing were given in Appendix 4.

The total model sizes were found to be 2.03 $x10^6$ cells for the full cylinders model, and 3.46 $x10^6$ cells for the 4-hole cylinders. The grid structures of full cylinders and 4-hole cylinders models are shown in Figures 5.2 and 5.3 respectively.

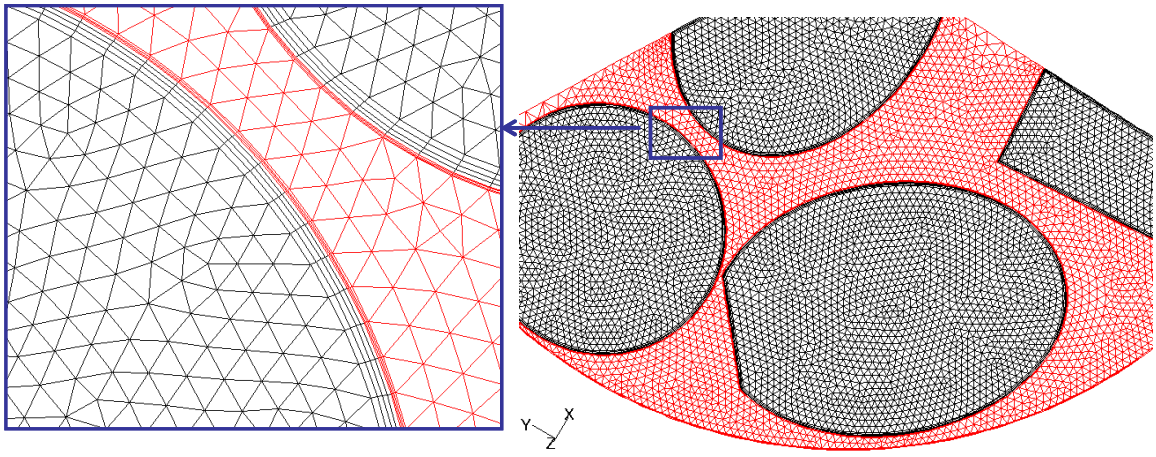

Figure 5.2 Grid structure of full cylinders model, and enlarged view of an arbitrary section.

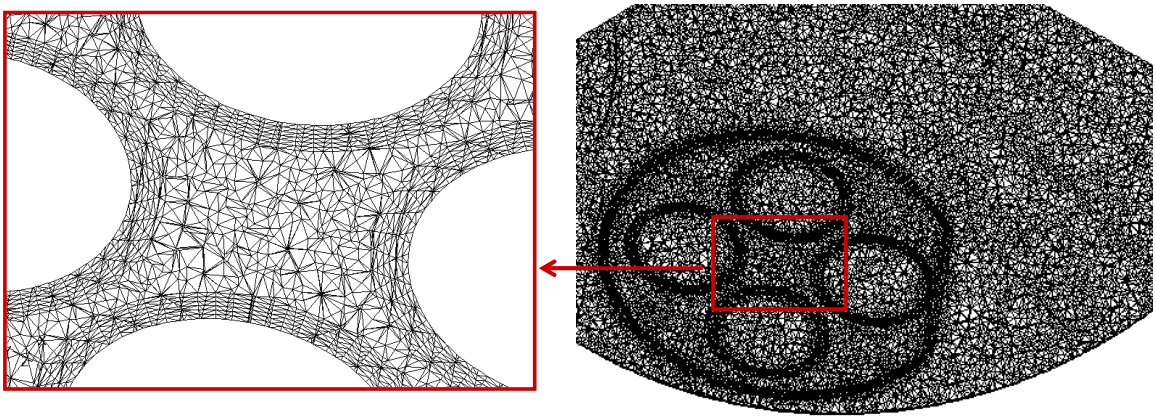

Figure 5.3 Grid structure of 4-hole cylinders model, and enlarged view of an arbitrary section.

In Figure 5.2, the top plane view mesh structure is shown where the fluid cells were colored by red and solid cells colored by black. An arbitrary section was enlarged to represent the prism structure in fluid and solid in detail. In Figure 5.3, the middle plane view mesh structure is shown. In the enlarged view, the fluid cells were removed to make the view clear.

In order to enable the intra-particle transport processes, the catalyst particles were converted into the *porous* structure from *solid*, which was the default setting and used for the particles in the previous part of this work. FLUENT defines additional *surface walls* which covers the *solid* volumes. So, once the solid volumes were converted into *porous*, those *surface walls* had to be converted into *interior* surfaces. This was a necessity, because the solid walls are impermeable, so they would prevent the species transport takes place between the pellet and the bulk fluid. Note that, in heterogeneous reactions, the three main mechanisms may be described as the adsorption of the reactants from the bulk fluid on the pellet, reaction, and desorption of the products to the bulk fluid.

FLUENT essentially considers the porous structure as a fluid zone. Porous media are modeled by the addition of a momentum source term to the standard fluid flow equations. The porous model allows setting additional inputs to model porous region including the

porosity value and velocity field information in the region. The porosity value was set to 0.44 as Hou and Hughes (2001) used for the steam reforming catalyst. Additionally, the velocity components were fixed and set to zero in the porous media to create a comparable pellet structure with the solid particles.

The simulations were first run to determine an initial isothermal constant-composition flow solution in the segment with periodic top and bottom conditions. This flow field was used subsequently to perform the energy and species solution in the non-periodic domain. It was observed that the changes in the flow field had minor effects on the reaction rates when the momentum and turbulence iterations were included to the energy and species iterations (Dixon et al., 2007).

The RNG κ-ε turbulence scheme was selected with EWT, and the SIMPLE pressure-velocity coupling algorithm with the first order upwind scheme was utilized. The convergence was monitored by the pressure drop value for the flow runs, and checking the energy balance and the reaction rates in the test particle for energy and species simulations in addition to the residuals. The computations were carried out on a Sun Microsystems SunFire V440 with 4 x 1.06 GHz processors.

5.1.1 MSR operating conditions

The same reactor conditions and fluid properties were used here as given in Table 3.1. Since the particles were converted into porous, the thermal conductivity of the pellets was set as 1.717 w/m-K to obtain the effective thermal conductivity as 1.0 w/m-K (as given in Chapter 3 for alumina) accounting for the pellet porosity. The other pellet properties were the same as given in Chapter 3.

Species transport in the porous pellets was modeled by effective binary diffusivities calculated from straight-pore Knudsen and molecular diffusion coefficients, and corrected using pellet porosity and tortuosity. The details of these hand calculations are given in Appendix 5(a). The dilute approximation method based on the Fick's law was selected, and diffusive flux values were calculated according to equation (1.25) by FLUENT. The

hand-calculated effective diffusivity values for each species, given in the Appendix 5(a), are defined as $D_{i,m}$ values. Actually, the multi-component method was additionally tested by defining the binary diffusivities, D_{ij}, and no significant difference was observed in the results. Therefore, the results shown in the next sections for MSR reaction were obtained by the dilute approximation method.

5.1.2 PDH operating conditions

The reactor conditions and the fluid properties are given in Table 5.1. The inlet mass fractions were 0.90 for C_3H_8, 0.05 for C_3H_6, and 0.05 for H_2.

The pellet properties were same as for the MSR particles. The diffusivities were calculated with the same procedure as the MSR calculations, and the values are given in the Appendix 5(b). For this reaction there were differences in the results for dilute approximation and multi-component methods, and therefore both results were represented in the relevant section.

Table 5.1: Reactor conditions and fluid properties for PDH reaction

T_{in} [K]	q_{wall} [kW/m^2]	P [kPa]	ρ [kg/m^3]	c_p [J/kg.K]	k_f [W/m.K]	μ [Pa.s]
874.15	2.0	0.101	1.8081	2180.25	0.0251	$8.01.10^{-6}$

5.2 Introducing MSR diffusion/reaction

A used-defined code was created to describe the sinks/source terms in the catalyst particles. In the user-defined code, the species source/sinks terms were defined as the following:

$$S_{Species,i} \equiv \rho_S (\alpha_{i,1} r_1 + \alpha_{i,2} r_2 + \alpha_{i,3} r_3) M_i \qquad (5.1)$$

where $\alpha_{i,j}$ represents the stoichiometric coefficient of component i in the reaction j. For example, for the reactions I, II, and III as given in equations (1.72), (1.73), and (1.74), the stoichiometric coefficients for CH_4 are:

$$\alpha_{CH4,I} = -1.0 \quad \alpha_{CH4,II} = 0.0 \quad \alpha_{CH4,III} = -1.0$$

Whereas the stoichiometric coefficients for H_2 are:

$$\alpha_{H2,I} = 3.0 \quad \alpha_{CH4,II} = 1.0 \quad \alpha_{CH4,III} = 4.0$$

The heat generation by the reactions was calculated by the same method as described in equation (4.4). As in the previous user-defined code, the code must return back to the main code the derivatives of the source terms with respect to the dependent variables of the transport equation, which are the mass fractions of the species, and temperature in this case. The algorithm of the species source/sinks calculations is shown in Figure 5.4.

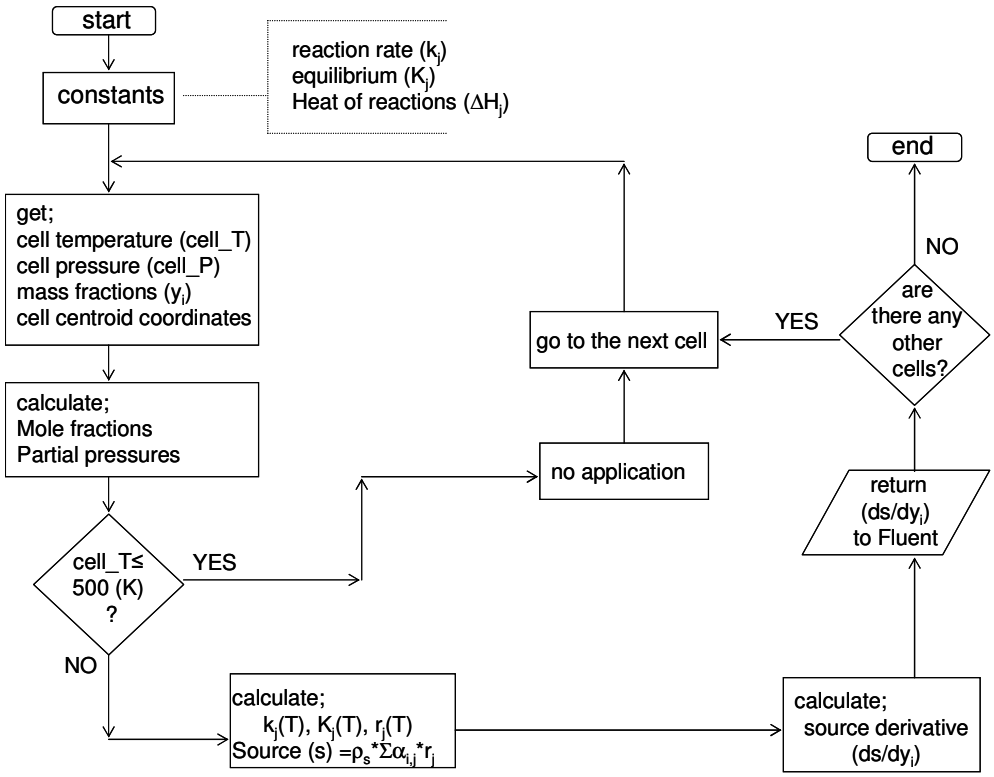

Figure 5.4 The algorithm for the species sinks/source calculations for diffusion /reaction application

The steps of the algorithm shown in Figure 5.4 were similar to the ones shown in Figure 4.13. One of the major differences was the mole fractions were not constant here, and they were calculated with the mass fractions that were obtained from the main computational domain by the code. The code has 5 sub-codes corresponding to energy term, and the terms for each species except the one with the largest mass fraction. Since the mass fraction of species must sum to unity, the N^{th} mass fraction was determined by N-1 solved mass fractions. When the species transport is turned on in the main computational domain of FLUENT, a list of the constituent species can be entered as fluid mixture. One has to keep in mind that the order of the species in that list is important. FLUENT considers the last species in the list to be the bulk species. Therefore, the most abundant species, that is the one with the largest mass fraction, must be set as the last one in the list (Fluent, 2005). In the MSR case this is water (H_2O).

The heat generation algorithm was similar to the species sinks/source one. The differences were; the source calculation where equation (5.1) was used instead of equation (4.4), and the derivative terms which were based on the temperature, not species mass fractions. The code is given in Appendix 3(c).

5.3 MSR diffusion/reaction application results

The full cylinders and 4-hole cylinders WS models were used for the MSR reaction implementation.

5.3.1 Full cylinders model

First, the flow results were obtained and compared to those from the solid particle model. Then, the reaction/diffusion application was done.

5.3.1.1 Flow simulation

To solve the momentum and turbulence equatios, the URF's at 0.05 less than the default values were used. The flow pathlines, released form the bottom surface for the porous particle model is shown in Figure 5.5(a). The pathlines are used to illustrate the flow for tube inlet conditions, and show the deflection of the flow around the porous regions. Flow features, such as regions of backflow and jet flow correspond to those in solid particle model shown in Figure 5.5(b).

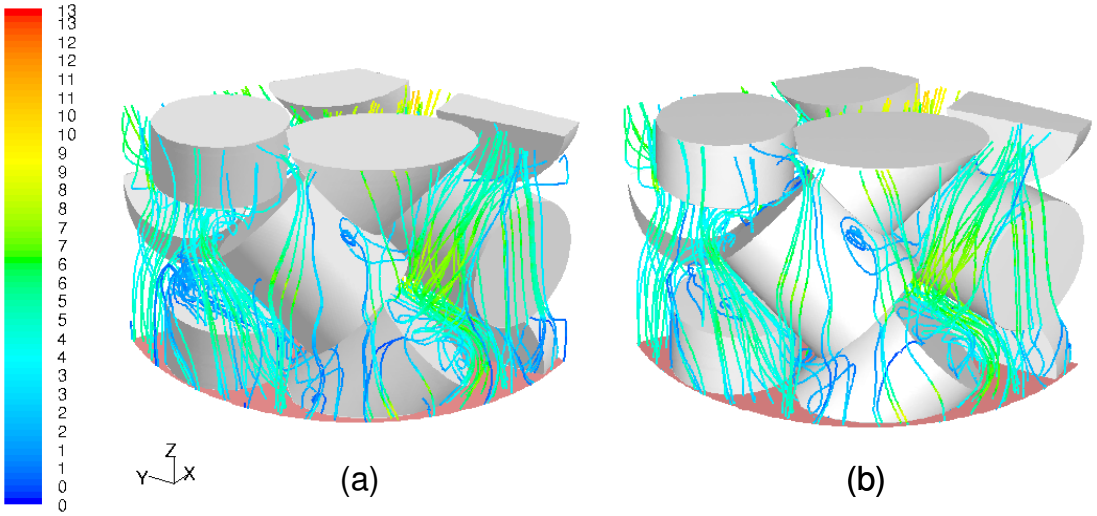

Figure 5.5 The flow pathlines released from bottom, and colored by velocity magnitude (m/s) for (a) porous particle model, (b) solid particle model.

Additionally, middle plane velocity magnitude contours are shown in Figure 5.6(a) and 5.6(b) for porous particle and solid particle models respectively. The porous particle settings created very similar results to the solid particle simulations.

A quantitative comparison may be carried out by considering the radial profiles of axial velocities for both porous and solid particle models, which is shown in Figure 5.7. Note that, the velocity profiles for both cases were almost same. These results confirmed that the change in treatment of the particles did not induce any significant changes in the simulations.

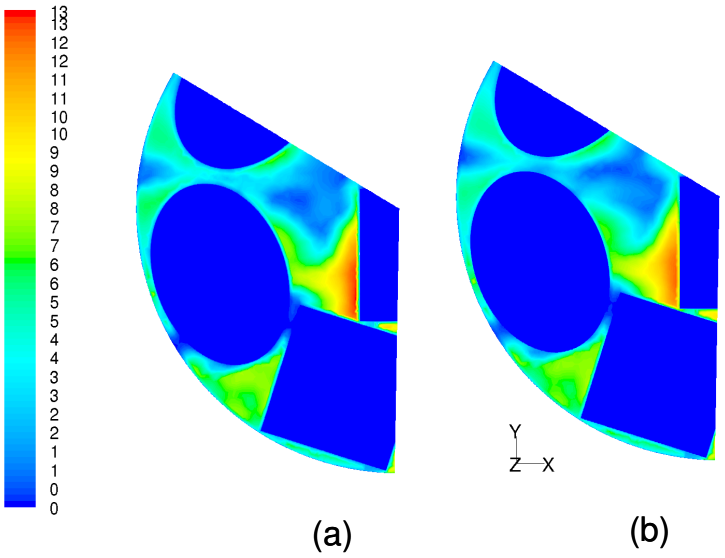

Figure 5.6 The middle-plane view velocity magnitude contours (m/s) for (a) porous particle model, (b) solid particle model.

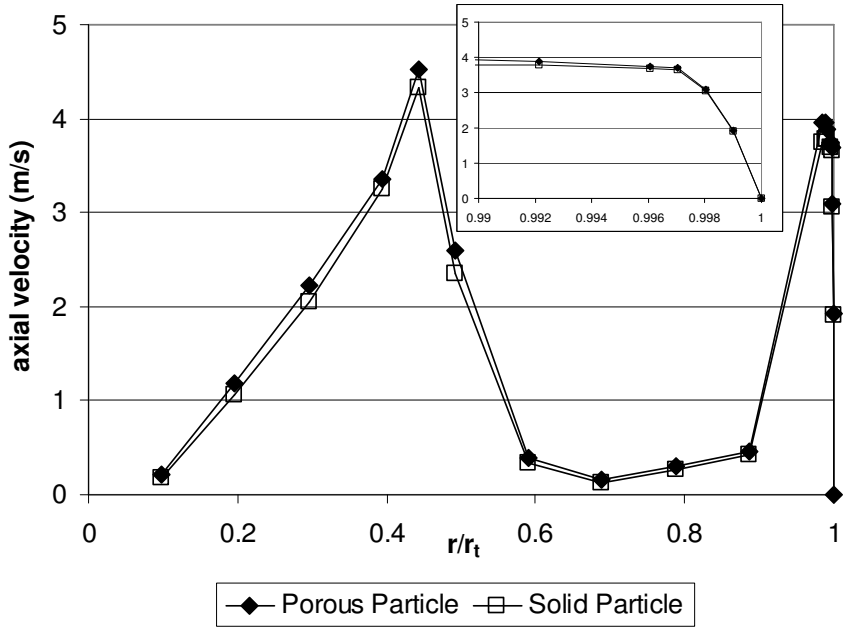

Figure 5.7 Radial profiles of axial velocities for porous and solid particle models.

5.3.1.2 Energy and species simulation

The energy and species balance equations were solved with URF's of 0.05 less than default values. For the converged solution, the residuals plot, the methane consumption rate for particle 2, and the heat balance plots are given in Appendix 6(a).

The diffusion/reaction implementation may be investigated by the variations of the temperature and species on the test particle surface and inside of the particle, by the radial profiles obtained for the entire model, and by the reaction engineering parameter effectiveness factor.

Particle surface variations: As a test particle, the particle number 2 surface temperature contours with the real position of the particle in the bed, and the open form of the surface are shown in Figures 5.8(a) and 5.8(b) respectively. The hotter spot on the front section of the particle 2 can be noticed as a result of the wall heat transfer. The open form of the particle 2 surface shows the significance of the wall heat transfer in a better way. The back surface of the particle 2 was 50 degrees colder than the front surface. As a result of the endothermic effects of the reactions, the lower surface temperatures have to be expected than the bulk fluid value (824.15 K). However, the tube wall heat transfer over-compensated for the endothermic effects of the reactions on the surfaces closest to the tube wall, which resulted in the hotter sections.

The cooler sections of the back surface may also be related to the relatively increased velocity field as shown in Figure 5.7 at $r/r_t \approx 0.40$. This particular radial position corresponds to the back of particle 2, and the heat transfer rate between the bulk phase and the particles in that region may be interrupted by the high velocity flow convection.

The local deviations on the particle 2 side surface are further shown for CH_4 and H_2 mass fractions in Figure 5.9. As can be noticed, the depletion in CH_4 results in the production in H_2. The local circular region which showed methane mass fraction minima, and corresponding hydrogen mass fraction maxima, at the S=0.03 m must be related to the vertex type of flow feature which occurred on that part of the surface.

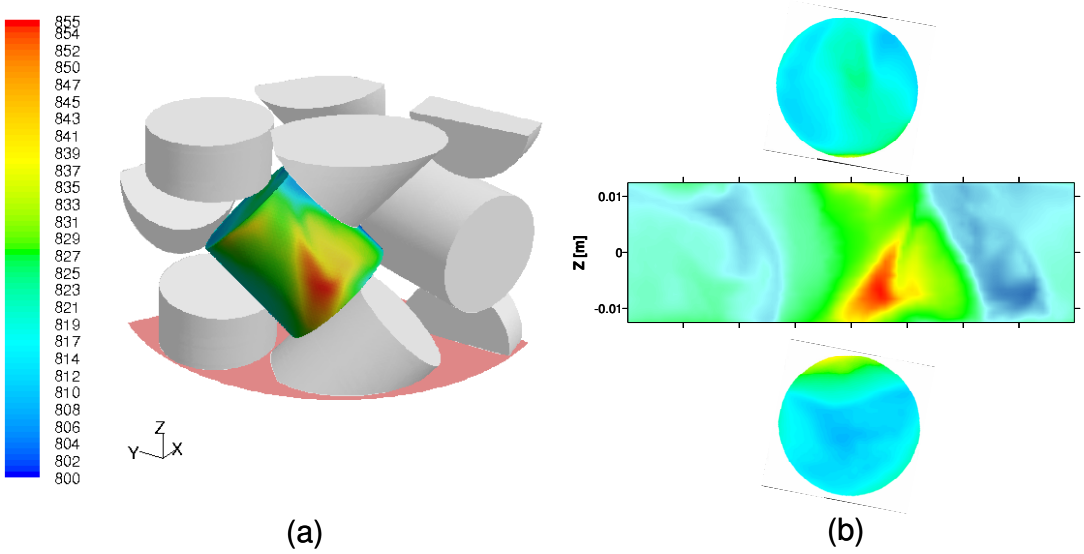

Figure 5.8 The full cylinders particle 2 surface temperature contours (K) for (a) the position of the particle in the bed, (b) the open form of the surface.

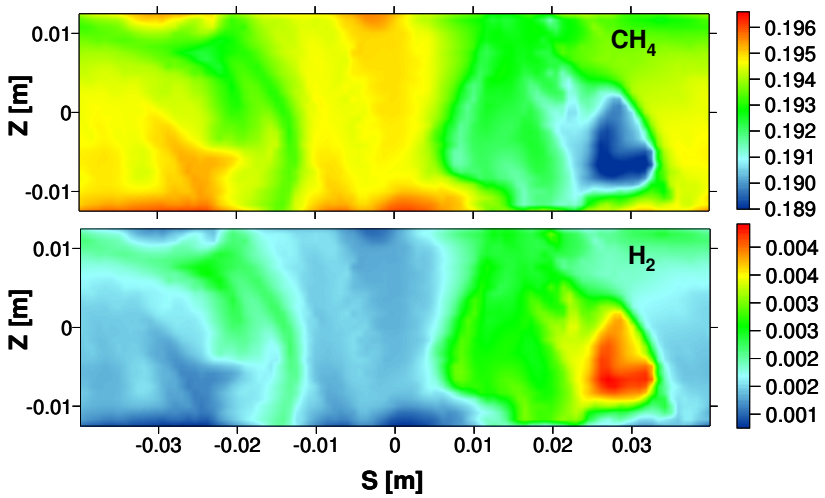

Figure 5.9 The full cylinder particle 2 side surface mass fraction contours for CH_4 and H_2.

The intra-particle variations: To investigate the intra-particle variations, the same vertical planes as used in Chapter 4 were utilized here, and shown in Figure 5.10(a).

In the figure, the radial center of the planes were scaled as the origin, and the two ends as r/r_p=-1.0 and r/r_p=+1.0, where r is the radial position in the particle, and r_p is the particle radius. In the axial direction, the origin was set to the lower corners, and the particle relative height was scaled as L/L_p=1.0 where L is the axial position in the particle, and L_p is the particle length.

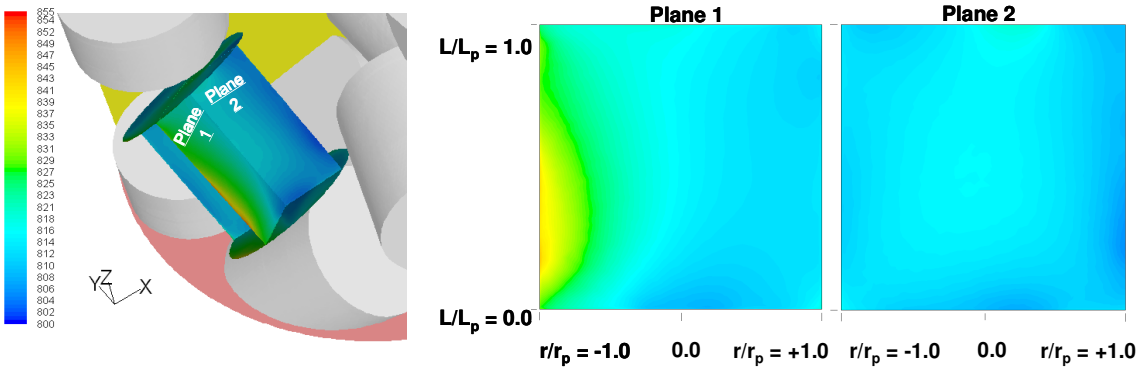

Figure 5.10 (a) Visual planes to investigate the intra-particle variations, and (b) the temperature contours on those planes for full cylinders model.

At the r/r_p=-1.0 of the plane 1, which is the closest section of the particle to the tube wall, the temperature was very high. Note that, this high temperature region was not on the axial center, L/L_p=0.50, of the particle. This is because of the rotated position of the particle, and as a result of this rotation, the lower end of the particle was closest to the tube wall. For the other positions on the plane 1, the temperature did not vary so much. For the entire plane 2, approximately 10 degrees of temperature variation was observed.

Although we have shown the intra-particle temperature variation with the reaction heat effects approximation method (Figure 4.15), different intra-particle temperature fields were observed in Figure 5.10(b). If we compare the plane 1 contours, the hotter spots can be seen in both figures with qualitative and quantitative differences. Although in Figure 4.15 the contours were given for different activity levels, which affected the magnitude of

the temperature, the hotter spot was located on the lower corner for every activity level. However, it was located at slightly higher position along the particle length for the contours obtained by the diffusion/reaction application approach. Additionally, on the hotter spots relatively lower temperature value was observed by the diffusion/reaction application method. These observations can be related to the methodologies behind the two approaches. The approximation method considers the uniform activity closer to the surface of the particle, and intra-particle temperature field is calculated with the constant bulk fluid species concentration values. On the other hand, the activity in diffusion/reaction application is defined by the physics, and temperature and species concentrations are calculated based on that. Obviously, considering the bulk species concentrations in the pellet, and setting the constant activity in the approximation method, creates a higher intra-particle temperature field for the reaction to proceed. However, if the concentrations are calculated according to the temperature filed, reaction again proceeds to reduce the reactants, and therefore reduce the intra-particle temperatures. In the diffusion/reaction application method the hotter spot was seen only at the closer point of the particle to the tube wall. However, in the approximation method the hotter spot on the lower corner of the particle was due to the combined effect of activity set on the side and on the bottom surfaces. The same effect was not seen on the top corner as standing relatively far from the tube wall.

As the benefit of diffusion/reaction application, the intra-particle species variations could also be investigated. Regarding the same visual planes, the CH_4 and H_2 mass fraction contours are shown in Figure 5.11.

As a result of the high temperature and corresponding reaction rate, a strong depletion of methane near the tube wall was observed in plane 1 contours of Figure 5.11. Accordingly, the increased hydrogen production was noticed on the same region. More uniform species distributions were observed in plane 2 contours as a consequence of very reduced near wall effects.

A more quantitative comparison can be obtained from the plots of CH_4 consumption rate, r_{CH4}, which is the sum of rates of reactions I and III, given in equations (1.72) and (1.74), as shown in Figure 5.12.

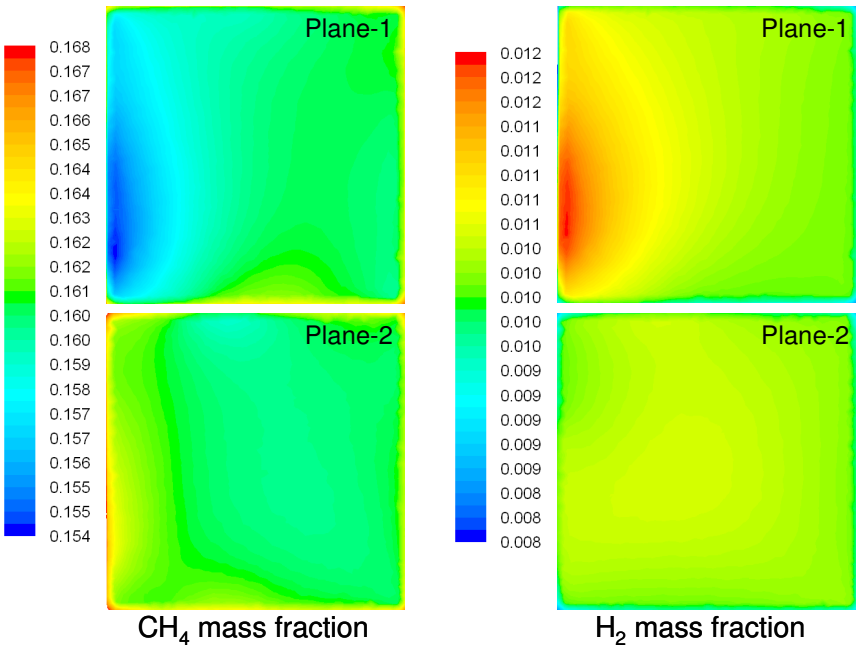

Figure 5.11 CH_4 and H_2 mass fraction contours on Plane-1 and Plane-2 for full cylinders model.

The plots show the change of CH_4 consumption rate along the length of the pellet for different radial positions. As can be seen from plane 1 plot, at the near wall region, the reaction rate was very high as a result of high temperature. For the radial positions away from the near wall region, the rates were reduced down. After the second half of the pellet, from r/r_p =0.0 to r/r_p =+1.0, the rates were almost the same.

Plane 2 reaction rates were almost the same for all radial positions with the same magnitude as the results obtained in the second half of plane 1. The main difference was seen at r/r_p=+0.97, where the CH_4 consumption rate was lower than the other radial position results. The lower temperature at that position, which is shown in Figure 5.9(b), created the lower reaction rates.

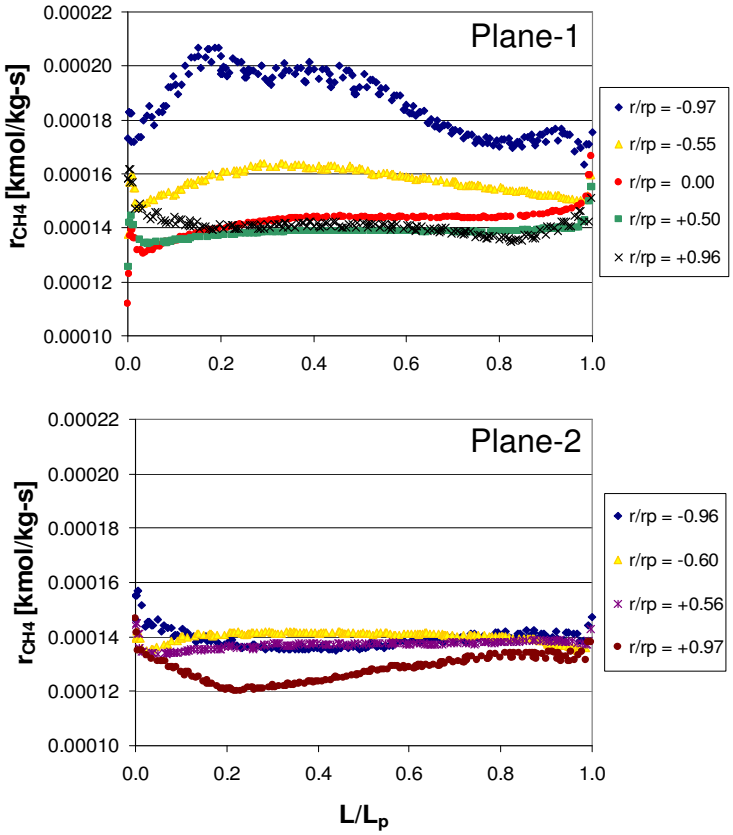

Figure 5.12 The CH_4 consumption rate plots for planes 1 and 2.

All the observations on plane 1 and plane 2 discussed here showed the strong temperature dependence of the MSR reactions.

The radial profiles: The radial temperature profiles, obtained similarly as described in Chapter 3, are shown in Figure 5.13. Additionally, temperature profiles for individual phases are shown in the same figure. The S-shape overall profile exhibits the combined effects of these phases along with the void fraction profile which is shown in Figure 4.18 previously for the full cylinders model.

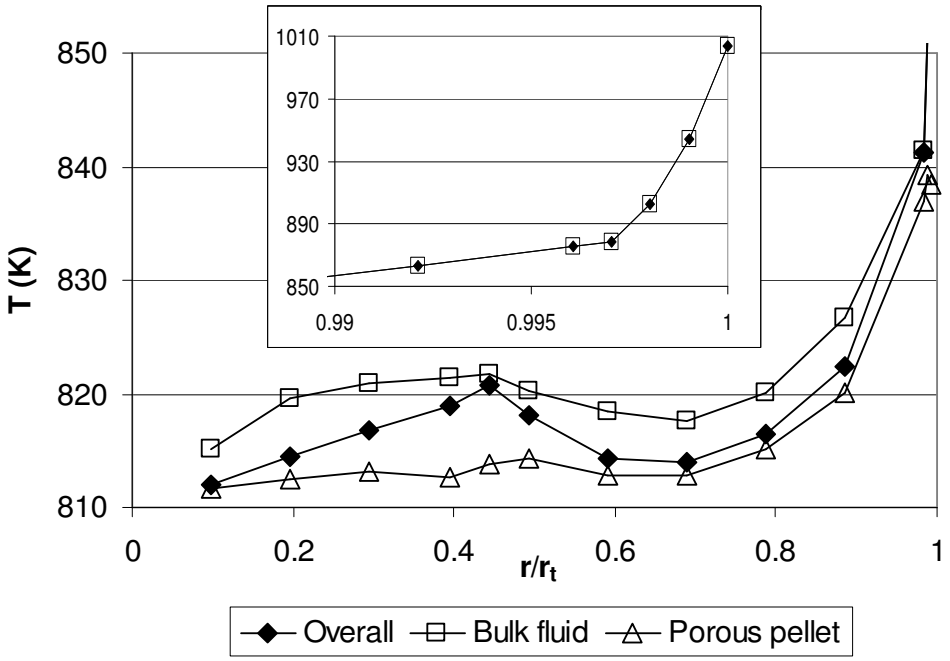

Figure 5.13 Radial temperature profiles, MSR full cylinders model.

The CH_4 and H_2 mass fraction profiles were also obtained for the same radial positions for which the temperature profile was obtained, and are shown in Figure 5.14. The strong S-shape overall CH_4 profile was observed which was again strongly influenced by the void profile. The bulk fluid values did not change much from the initial values. However, the overall mass fractions inside the pellet were influenced by the void fractions, especially for the radial positions of $r/r_t \approx 0.40$ and $r/r_t \approx 1.00$ where the maximum local voidage values were observed. The mirror effect can be noticed between the CH_4 and H_2 profiles as a result of the nature of the reactions: CH_4 is consumed and H_2 is produced.

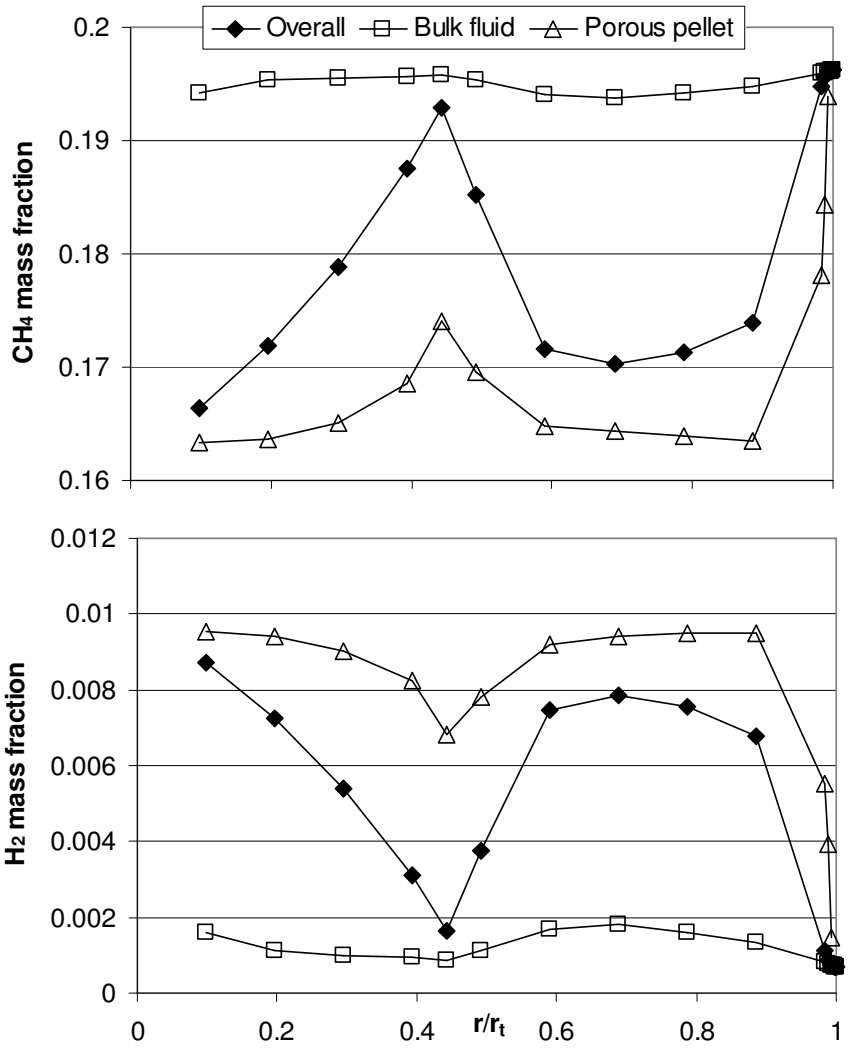

Figure 5.14 Radial CH_4 and H_2 profiles for full cylinders model.

The effectiveness factor: As described in Chapter 1 and defined in equation (1.54), the diffusion resistance on the reaction rate can be expressed with the effectiveness factor, η. It has been known that there are strong diffusion limitations on the MSR reaction, and most of the kinetic studies neglect them (Xu and Froment, 1989a). In the context of the requirements of quick analysis and process improvement implementations for todays design engineering environment, the concept of intra-particle gradients and effectiveness factor is quite valuable in reasoning and decision making (Rase, 1990).

To calculate the effectiveness factor, based on the definition, we needed the averaged reaction rate in the catalyst particle, and the reaction rate on the particle surface. For the reaction rate inside of the particle, the rates were calculated for each computational cell, and the volume averages were taken. This was done by a user-defined code, and it is given in Appendix 3(d) for the particle 2. The reaction rates were then returned to FLUENT and obtained from its user interface.

For the surface reaction rate calculation, the surface temperatures, and species mole fractions were exported in an ASCII file for each surface cell. Using this ASCII file, a spreadsheet was prepared to calculate the reaction rates for each cell, and then the area averaged values were obtained.

These calculations were carried out for the three reactions of interest, and the effectiveness factors for particle 2 were obtained by the equation (1.54) as:

$$\eta_{reaction-III} = \frac{1.01952\times10^{-5}}{1.21931\times10^{-4}} = 0.0836 \qquad \eta_{reaction-I} = \frac{8.43953\times10^{-7}}{5.20169\times10^{-6}} = 0.1622$$

$$\eta_{reaction-II} = \left|\frac{-1.47770\times10^{-7}}{2.43370\times10^{-7}}\right| = 0.6072$$

As can be noticed, the surface reaction rates were higher than the particle reaction rates, which results in the effectiveness factors of less than unity. It can also be noted that, the reaction-III is the dominant reaction as compared to the others, by an order of magnitude of the reaction rates. So, the low effectiveness factor for the dominant reaction is in agreement with the industrial observations (Stitt, 2005), and with the pseudocontinuum modeling results (Pedernera et al., 2003).

The reaction-II, which is known as the water-gas-shift reaction (WGSR), is strongly equilibrium limited due to the thermodynamic constraints at high temperatures. Therefore, there is a strong tendency to proceed in the reverse direction. The negative reaction rate obtained for WGSR in the particle was due to this phenomenon. However, the surface reaction rate was in the forward direction, which implied that the CO_2 and H_2 diffused to the bulk fluid more easily, and since the equilibrium level was not reached, the

reaction proceeded in the forward direction which resulted in a positive reaction rate value.

In order to calculate the effectiveness factors for a pellet that is not affected by the tube wall, particle number 12 was additionally considered, although it was not entirely in the model. This particle is standing at the back of particle 2 at the same axial position as shown in Figure 5.15.

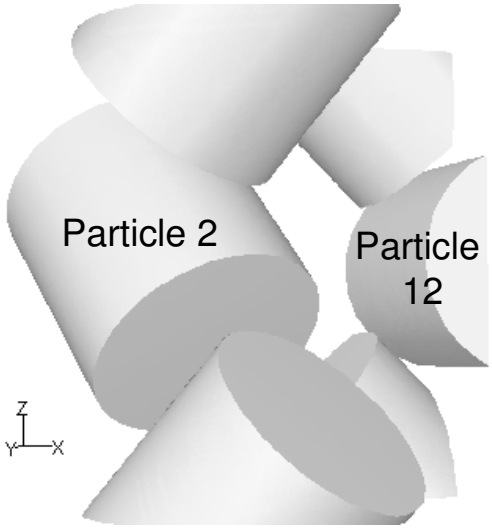

Figure 5.15 Particle 2 and 12 relative positions in WS model.

The reaction rates for particle 12 were calculated as described above and the effectiveness factors were found to be:

$$\eta_{reaction-III} = \frac{1.11173\times10^{-5}}{1.23545\times10^{-4}} = 0.1106 \qquad \eta_{reaction-I} = \frac{9.26538\times10^{-7}}{3.86538\times10^{-6}} = 0.2399$$

$$\eta_{reaction-II} = \left|\frac{-1.78318\times10^{-7}}{2.27753\times10^{-7}}\right| = 0.7829$$

When the effectiveness factors of particle 2 and particle 12 are compared, the higher values for the particle away from the wall can be noticed, although this difference was not too much.

The wall effect on the effectiveness factor, as an averaged reaction engineering parameter, may be utilized to obtain the radial effectiveness factor profiles for the entire

model. Again, regarding the definition of the η, we needed the surface reaction rates for each radial position. For this reason, particle surface planes were created in addition to the available visual radial planes. In Figure 5.16(a) the previously generated radial plane is shown at r/r_t = 0.89 as an example case where the particles were colored by red, and the fluid was colored by yellow. The particle surfaces plane, which is shown in Figure 5.16(b) for the same radial position, was created considering only the outer shell intersections of the particles at the same radial position.

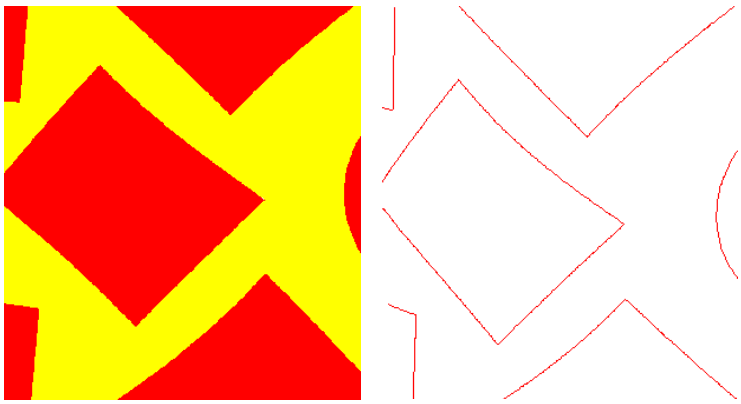

Figure 5.16 (a) the particle and fluid regions, and (b) the particle surfaces for the radial position of r/r_t = 0.89.

The temperatures and the species mole fractions were obtained from these surface planes for each radial position, and reaction rates were calculated on a spreadsheet. The obtained surface reaction rate radial profiles are shown in Figure 5.17 for reactions I and III. The increasing trend of the surface reaction rates can be noticed for both of the reactions towards the tube wall where the maximum values were reached. Figure 5.17 also represents the near wall effects on the particle surfaces which directly reflected to the surface reaction rates. Fluctuations were observed around the r/r_t = 0.40 position for both of the reactions. The reason for these changes can also be related to the local bed voidages. The reaction rates had to be calculated utilizing the temperature and species

information for the less solid surface area in the related radial positions. Therefore, the area averaged values were more sensitive to the maximum or minimum values as a result of their contribution to the final averaged value.

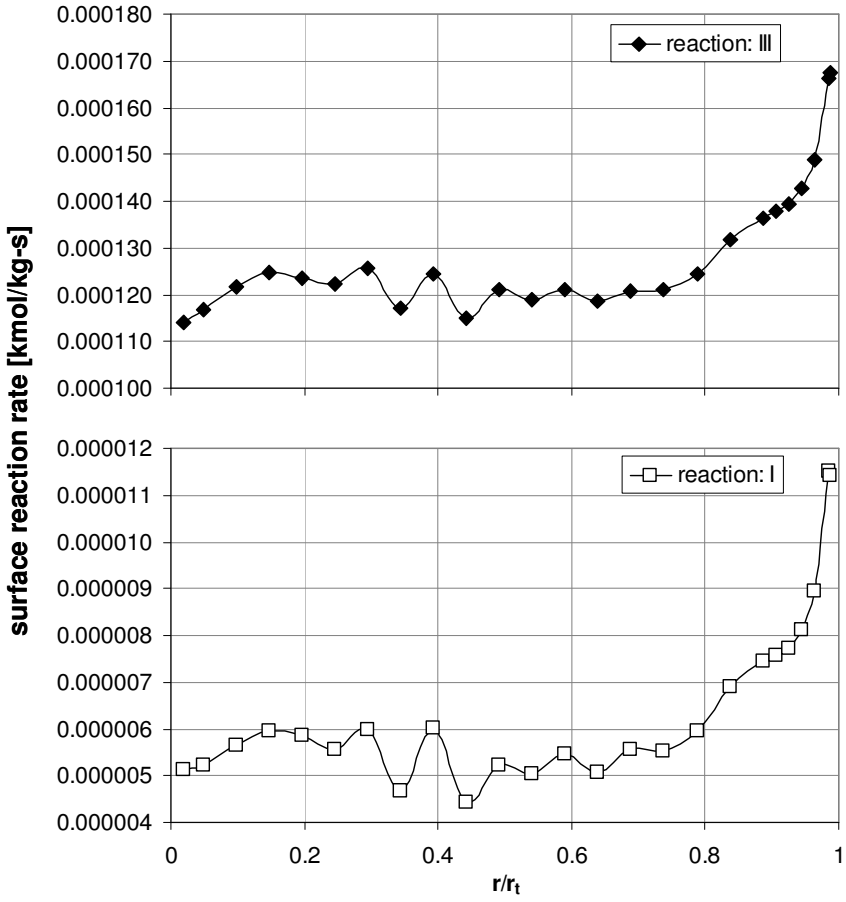

Figure 5.17 The surface reaction rate profiles for reactions I and III.

To obtain the radial effectiveness factor profiles, a representation of the reaction rate profile inside the pellets was necessary. The available pellet reaction rates for particles 2 and 12 were utilized for this purpose. If the particle 2 reaction rate is considered as the pellet reaction rate closest to the wall, and the particle 12 reaction rate is considered as the

pellet reaction rate at the center of the tube, the reaction rate profile may be obtained by the following expression:

$$r_{pellet}(r) = r_{particle\_2} \times \frac{r}{r_t} + r_{particle\_12} \times (1 - \frac{r}{r_t}) \qquad (5.2)$$

where r is the radial position in the reactor tube, r_t is the tube radius. According to this expression the pellet reaction rate profiles were obtained as linear curves.

Utilizing the pellet and surface reaction rate profiles, the effectiveness factor profiles were obtained as shown in Figure 5.18.

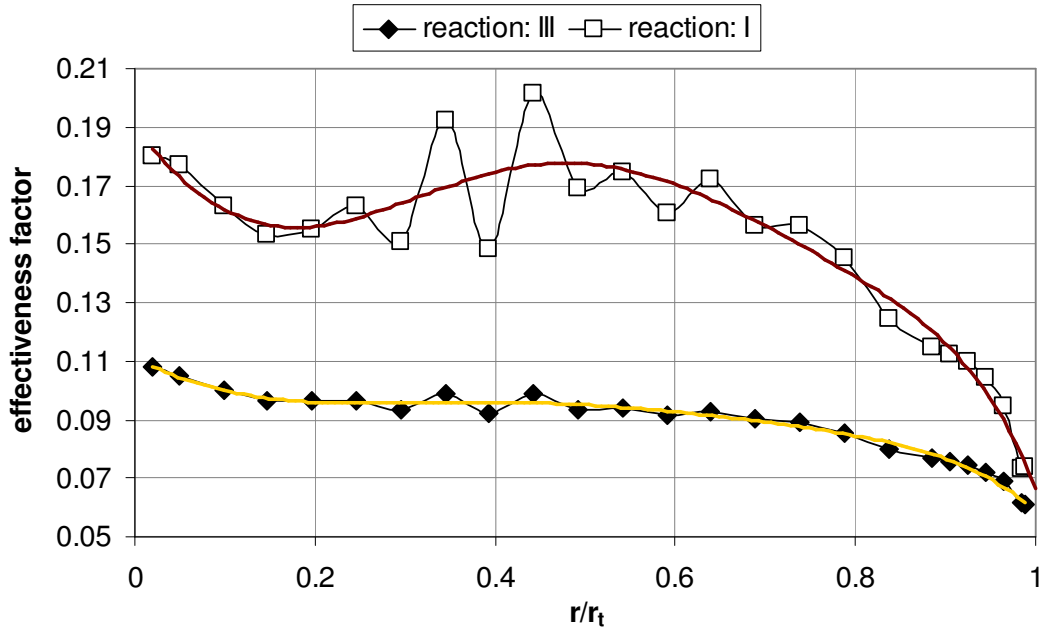

Figure 5.18 The effectiveness factor profiles for reactions I and III.

The polynomial trend-lines were added to the above figure with a yellow color for reaction III, and a red color for reaction I. Towards the near wall region, the effectiveness factors decreased for both reactions as a combined effect of surface reaction rate shown in Figure 5.17, and pellet reaction rates calculated by equation (5.2). Higher effectiveness

factors of reaction I than reaction III were observed, although they came closer in the near wall region.

The other method of obtaining the pellet reaction rate profile may be to consider the step change in pellet reaction rates instead of setting a linear change as described above. This can be done by considering particle 12 reaction rate from $0.0 \leq r/r_t < 0.5$, and particle 2 reaction rate for $0.5 \leq r/r_t \leq 1.0$ as the pellet reaction rate profile. Then, the effectiveness factor profiles can be obtained with the same surface reaction rate values used above. The comparison of the effectiveness factor profiles obtained by a linear and by a step change in the pellet reaction rates is shown in Figure 5.19 for only the dominant reaction.

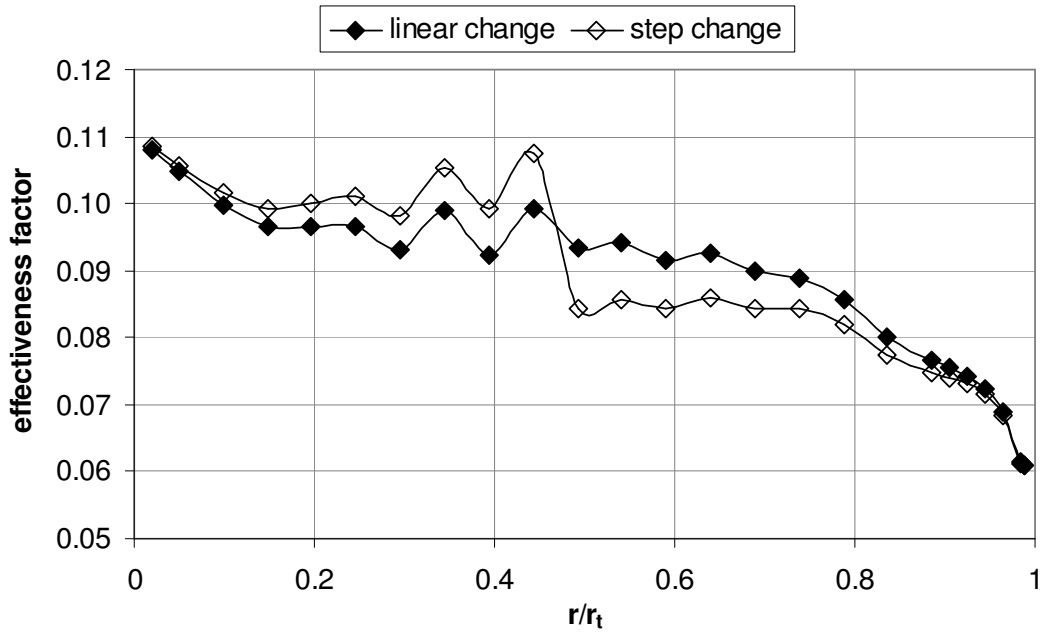

Figure 5.19 The effectiveness factor profiles for reaction III with linear and step change in pellet reaction rates.

As can be seen in Figure 5.19, the step change effect is noticeable in the center of the model, and there was not a smooth transition as in the linearly varied one. However, in total, the trends were quite similar in both cases.

There is an order of magnitude difference observed in effectiveness factors obtained by us and Pedernera et al. (2003) where they have focused on the axial middle location of the reactor. The methodological difference was that, we have utilized the realistic 3D flow field around the explicitly positioned realistic catalyst particles, and considered the interactions between the bulk fluid and the pellets in our modeling. However, Pedernera et al. considered the pseudocontinuum approach to make one-dimensional particle simulations, as summarized in Chapter 2.

We will make use of our effectiveness factor profile in Chapter 6 where we will compare the results obtained in this chapter with the explicitly created pseudocontinuum model.

5.3.2 4-hole cylinder model

As in the full cylinders model simulations, first the flow solution was obtained, and then the reaction/diffusion was applied.

5.3.2.1 Flow simulation

The flow simulation was carried out by solving the momentum and turbulence equations as before. The URF's were selected as 0.05 less than the default values. The flow pathlines, released from the bottom surface are shown in Figure 5.20.

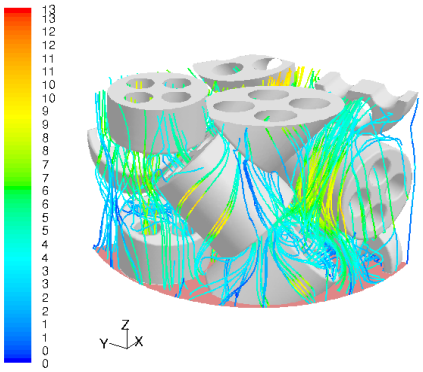

Figure 5.20 The flow pathlines released from bottom, and colored by velocity magnitude (m/s) for 4-hole model.

5.3.2.2 Energy and species simulation

To reach the converged energy and species simulation, iterations were started with the URF values of 0.05 for 3000 iterations. After the residuals were flattened out, the factors were increased to 0.20 for 500 iterations. Then, they were raised to 0.50 for 500 iterations more. Finally the simulations were completed with the URF's of 0.80, totally in 21000 iterations. The residuals plot, the methane consumption rate for particle 2, and heat balance change during the iterations are given in Appendix 6(b).

Particle surface variations: The surface temperature contour of particle 2 is shown in Figure 5.21(a) for the exact location of the particle in the bed, and in Figure 5.21(b) for the open form of it.

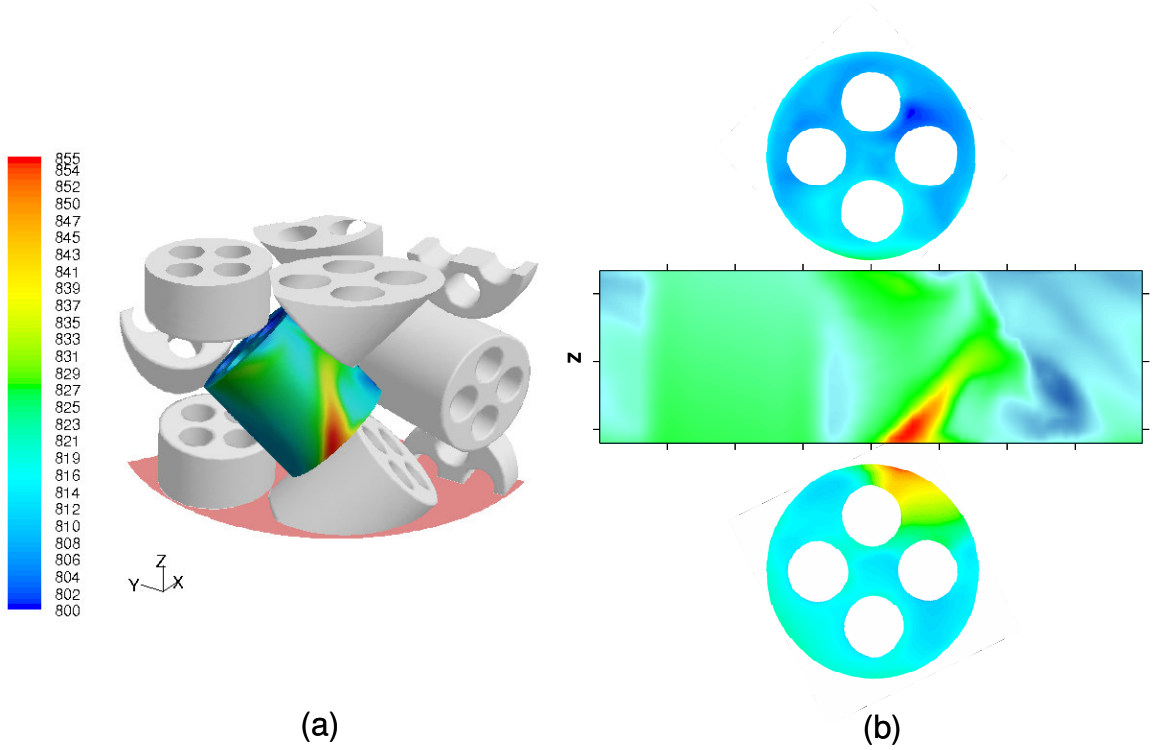

Figure 5.21 The 4-holes particle-2 surface temperature contours (K) for (a) the position of the particle in the bed, (b) the open form of the surface.

The hotter section on the particle surface for the closest point to the tube wall can be noticed for this model in a slightly less pronounced way as compared to the full cylinders model shown in Figure 5.8. The hotter section originated from the lower corner of the particle, and propagated upwards with the flow convection. The related hotter region of the particle bottom surface can be seen in the open form of the surface, and mostly the closest internal hole to that section was influenced by the wall effect. This situation may be clearly seen in Figure 5.22. The internal hole that was affected by the tube wall is shown with a dashed line bordered rectangle.

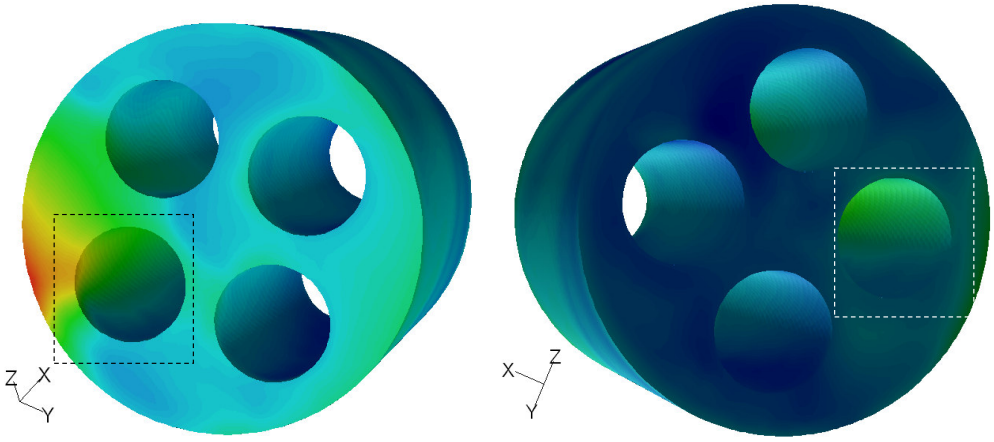

(a) (b)

Figure 5.22 The 4-hole cylinders model particle 2 detailed view (a) bottom, (b) top.

Previously, the flow field comparison of the models with different sizes and numbers of internal holes was investigated (Nijemeisland, 2002), and it is not the scope of our work. On the other hand, to emphasize the benefit of multi-hole catalyst particles regarding the diffusion/reaction taking place in them, the above observation may be coupled to the Figure 5.23 where the pathlines passing through the holes of the particle 2 are shown. In Figure 5.23(a), the pathlines are colored by the velocity magnitude which represents the different velocity fields inside the holes, whereas in Figure 5.23(b), they were colored by the static temperature which shows the temperature difference of the fluid passing through the holes. The hole with the hotter surface, shown in Figure 5.22, is represented by the dashed lines in Figure 5.23. Although the velocity passing through that hole was higher than the other holes, the fluid heated up while passing through that hole. This was achieved by conduction from the inside wall of that hole to the fluid, and by convection in the fluid. Ultimately, these phenomena are triggered by the tube wall heat transfer. Increasing the particle fluid contact area, or GSA, with introducing multiple holes, and effects of transport phenomena may be further investigated by intra-particle temperature and species variations.

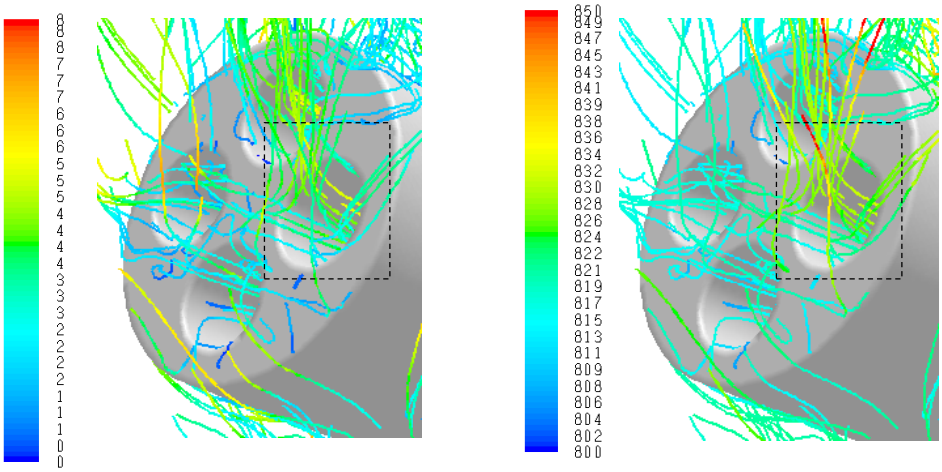

(a) (b)

Figure 5.23 The pathlines of flow passing through the holes of particle 2, colored by (a) the velocity magnitude (m/s), and (b) the static temperature (K).

The intra-particle variations: To investigate the intra-particle temperature and species variations, the 45 degree rotated versions of plane 1 and plane 2 along the particle axis were generated as plane 3 and plane 4 which intersect the internal holes in the model. The plane 1 and plane 2 temperature contours are shown with their original positions in Figure 5.24(a), and with the transformed versions in Figure 5.24(b).

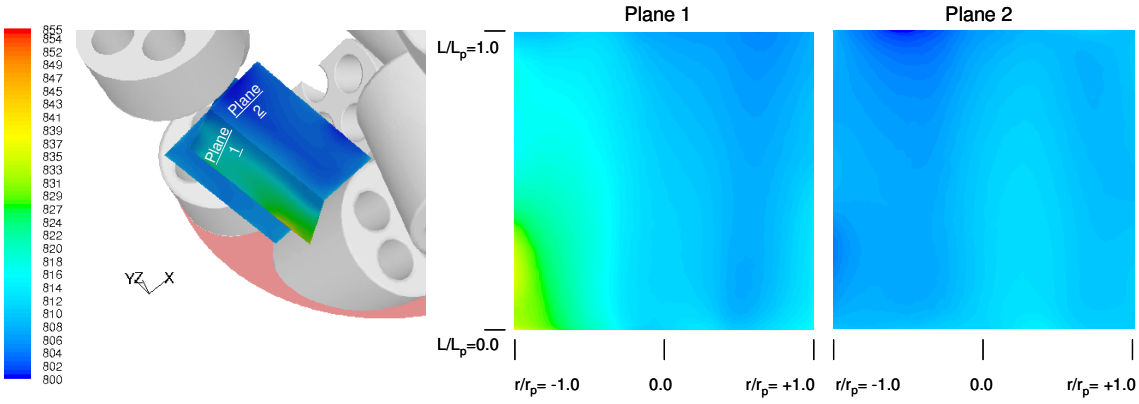

(a) (b)

Figure 5.24 (a) Visual planes 1 and 2 to investigate the intra-particle variations, and (b) the temperature contours on those planes for 4-hole cylinders model.

The maximum temperature was reached on the lower left corner of plane 1, and the particle gradually cooled down towards the inside of it due to the reaction heat effects. The relatively cooler and hotter longitudinal patterns were seen on the planes in Figure 5.24(b) as a result of the contribution of the surfaces of the inner holes located close by. Additionally, the CH_4 and H_2 mass fraction contours on the same planes are shown in Figure 5.25. The strong methane depletion and hydrogen production can be noticed on the lower left corner of the plane 1 where the higher temperature region was seen in Figure 5.24(b). Right after that, at the position $r/r_p \approx -0.5$, the sudden increase in CH_4, and a decrease in H_2 mass fractions were observed with a small spot on the bottom of plane 1. This position was very close to the nearest hole, and plane 1 was almost intersected by that hole. Therefore, the species mass fractions were influenced by the bulk fluid values in that point. Since the intra-particle temperature value at that position was similar to the fluid temperature, we have not seen a difference in the temperature contour.

The plane 2 CH_4 and H_2 contours can be directly supported by the temperature contours. At the position of $-1.0 < r/r_p < 0.0$, as a result of the lower temperatures, the higher methane and lower hydrogen mass fractions were seen. However, the effects of increase in temperature at $0.0 < r/r_p < 0.5$ on the methane and hydrogen quantities were noticeable.

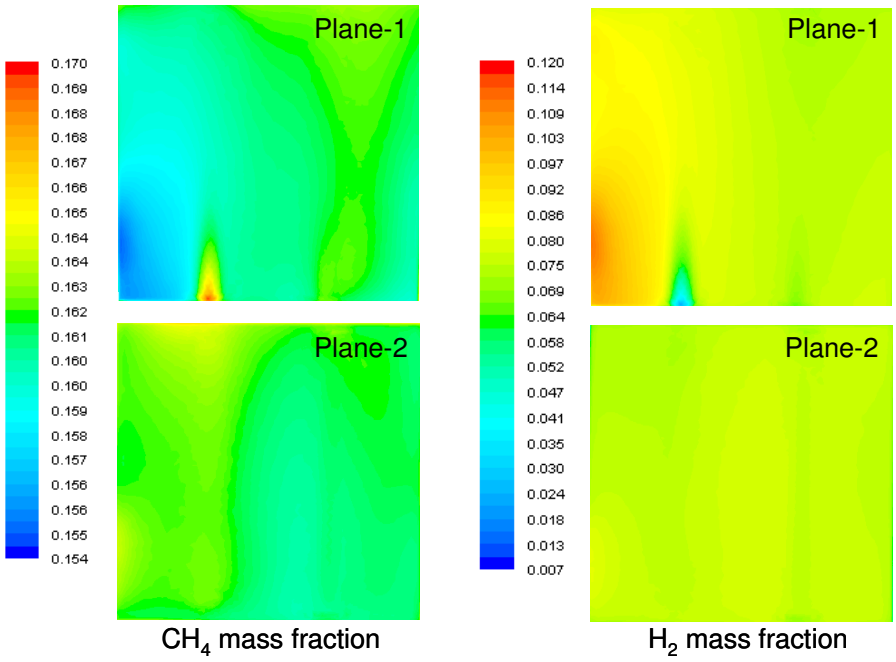

Figure 5.25 CH_4 and H_2 mass fraction contours on Plane-1 and Plane-2 for 4-hole cylinders model.

The plane 3 and plane 4 temperature contours are shown in Figure 5.26. These planes were created at the positions where the holes are intersected almost at their centers. The temperature difference of different holes can be seen well here as a supporting argument to the above. Fluid passing through the closest hole to the tube wall has the higher temperature. The temperature of the catalyst region closest to the tube wall was also higher.

The species distributions on planes 3 and 4 are presented in Figure 5.27. Note that the scales are different in plane 3 and 4 than plane 1 and 2 in order to capture the fluid values. It was observed that, the fluid region mass fractions mostly stayed at the inlet conditions. From the fluid to the pellet regions, a sharp transition was noticed due to the strong diffusion limilations.

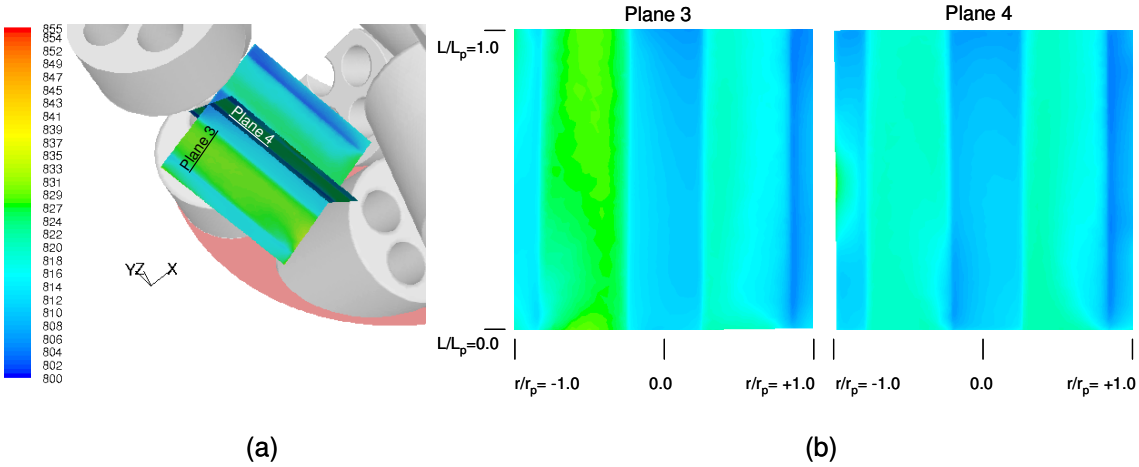

Figure 5.26 (a) Visual planes 3 and 4 to investigate the intra-particle variations, and (b) the temperature contours on those planes for 4-hole cylinders model.

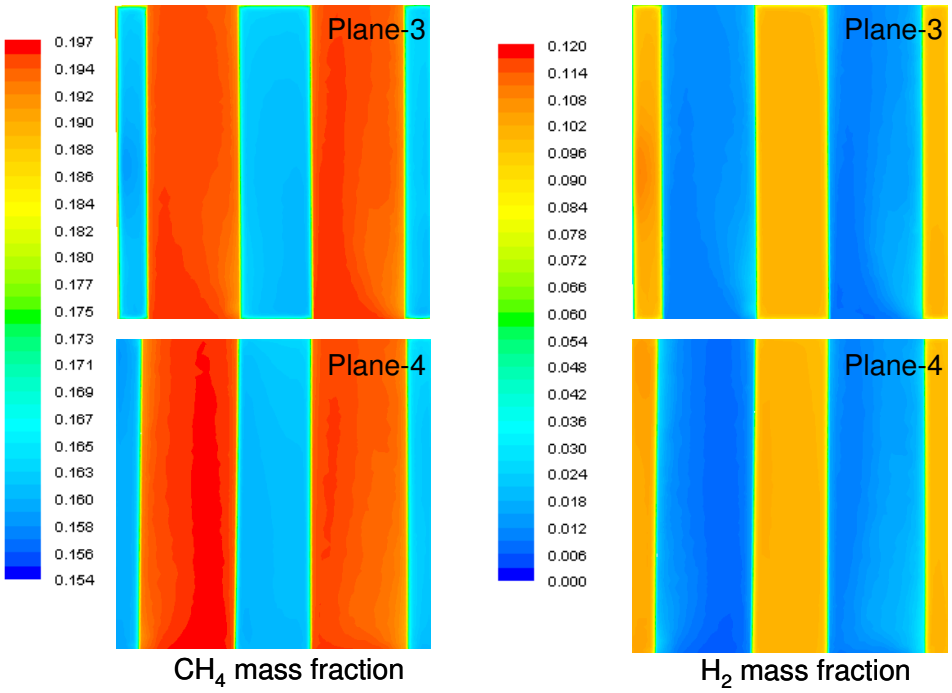

Figure 5.27 CH_4 and H_2 mass fraction contours on Plane-3 and Plane-4 for 4-hole cylinders model.

The radial profiles: As in the full cylinders case, similar radial profiles were obtained. In Figure 5.28 the overall (pseudohomogeneous), and fluid and solid region temperature profiles were shown. Again, a similar combined effect of the fluid and solid regions was observed on the overall profile with the local porosity influence. Additionally, the overall temperature profile was lower than in the full cylinders model, as in the case of the reaction approximation discussed in Chapter 4.

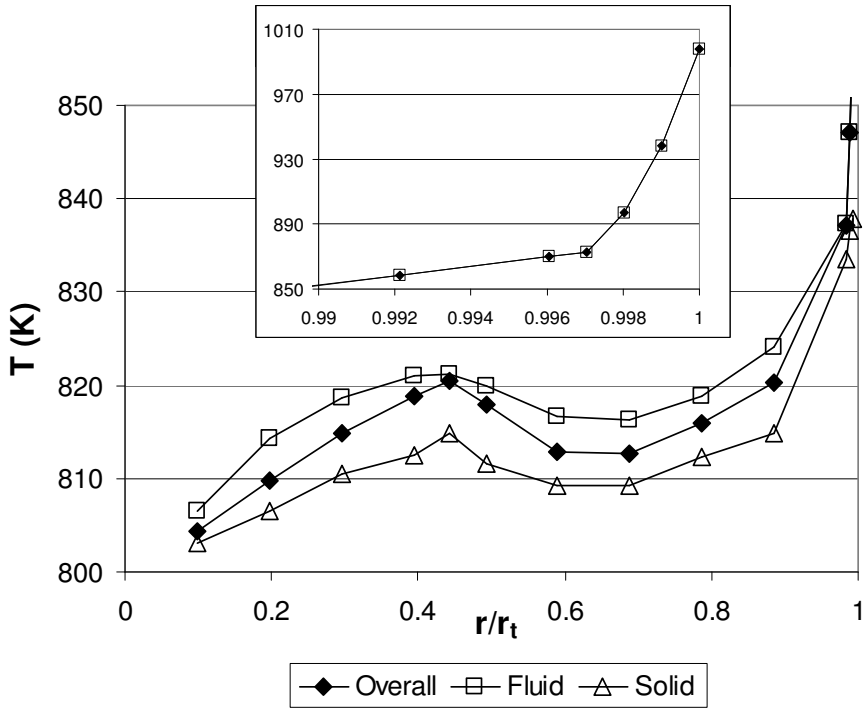

Figure 5.28 Radial temperature profiles, MSR 4-hole cylinders model.

The CH_4 and H_2 mass fraction profiles are presented in Figure 5.29. Similar features are observed in the species profiles with the full cylinders, except the noticeable difference in the overall profiles in the region $0.6 < r/r_t < 0.9$. The bed porosity profiles of full and 4-hole cylinders were shown in Figure 4.16, and there was a significant difference in that region: the 4-hole cylinders model had a higher voidage than the full cylinders. As a result of that, the fluid region compositions influenced the overall species profiles to create higher CH_4 and lower H_2 contents in $0.6 < r/r_t < 0.9$.

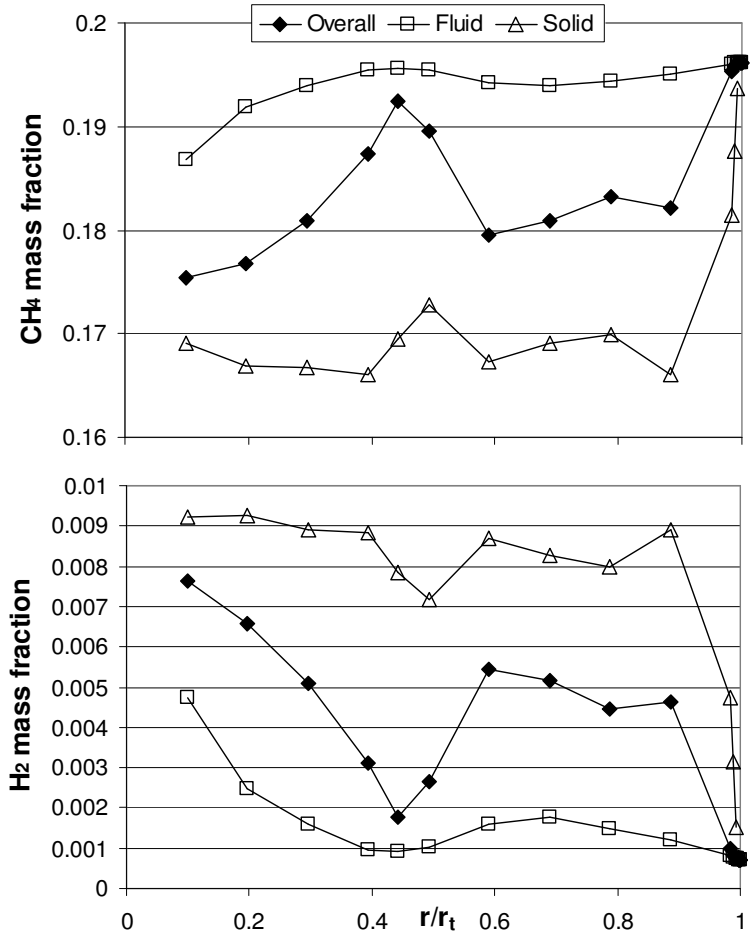

Figure 5.29 Radial CH_4 and H_2 profiles for 4-hole cylinders model.

The effectiveness factor: For the 4-hole cylinders model particles 2 and 12, the effectiveness factors were obtained with the same procedure described for the full cylinders model. For reactions I and III, the values are found to be:

Particle 2

$$\eta_{reaction-III} = \frac{2.51065\times10^{-5}}{1.14770\times10^{-4}} = 0.21875 \qquad \eta_{reaction-I} = \frac{1.85686\times10^{-6}}{4.50823\times10^{-6}} = 0.41250$$

Particle 12

$$\eta_{reaction-III} = \frac{2.13930\times10^{-5}}{1.12563\times10^{-4}} = 0.19005 \qquad \eta_{reaction-I} = \frac{1.60310\times10^{-6}}{4.94254\times10^{-6}} = 0.32430$$

At a first glance, we have obtained higher effectiveness factors for the front particle than for the back particle, contrary to the findings of the full cylinders model. Probably for 4-hole cylinders model, particle 12 is not the best choice to consider as a representative back particle. Since particle 12 was not entirely in the model, the section where inner holes were located stayed outside of the model, and we did not see the effect of the inner holes on the surface reaction rates, and ultimately on the effectiveness factors.

When we compare the effectiveness factors of reaction III for 4-holes and full cylinders models, we see a 260% increase due to the 66% GSA improvement with inner holes inclusion.

5.4 Introducing PDH diffusion/reaction application and results

The PDH diffusion/reaction implementation was applied only to the full cylinders model by the same procedure utilized in the MSR reaction application. The user-defined code created for this purpose is given in Appendix 3(e).

The flow solution was obtained for 4000 s^{-1} Gas Hourly Space Velocity (GHSV) (Jackson and Stitt, 2004) at steady-state condition which corresponds to the Reynolds number of 350 based on superficial velocity and the particle diameter of a sphere of equivalent volume to the cylindrical particle. Although, in general, this value is quite low to be considered as in the turbulent region, the complex flow field in fixed bed reactors has been modeled with different turbulent schemes by many researchers for even lesser Reynolds number values (Romkes et al., 2003; Guardo et al, 2004). We have selected the RNG κ-ε turbulence scheme with EWT approach for this study.

The flow solution was obtained by URF's of 0.05 less than default values and the flow pathlines are shown in Figure 5.30. Relatively smooth flow features were observed as a result of the lower superficial velocity setting.

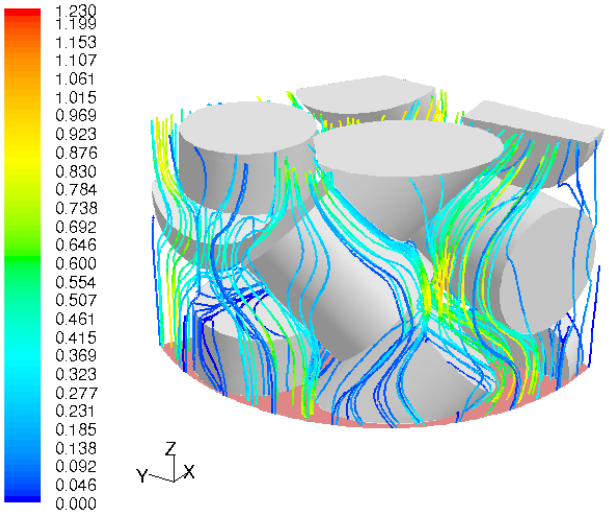

Figure 5.30 Flow pathlines released from bottom, and colored by velocity magnitude (m/s) for PDH reaction.

The PDH diffusion/reaction implementation was carried out with two different diffusion coefficient settings as described before. For the dilute approximation method, the pre-calculated $D_{i.m}$ values were defined, whereas for the M-C method, the binary diffusivities, D_{ij}, were set into the materials menu of FLUENT, and $D_{i.m}$ values were calculated by FLUENT with equation (1.26). The main difference in these two methods was that the pre-calculated $D_{i.m}$ values were obtained by us from molecular and Knudsen diffusivities for dilute approximation method, whereas, the $D_{i.m}$ values were calculated by FLUENT from the mass fractions and binary diffusivities only for M-C method. As mentioned before, these values are given in Appendix 5(b).

The diffusion/reaction application results are compared for particle surface variations, intra-particle variations, and effectiveness factors

Particle surface variations: The test particle surface temperature contours are shown in Figure 5.31. Thirty to forty degrees higher surface temperatures were obtained by the dilute approximation method. Significantly hotter sections along the particle axis were noticed on the front of the test particle as opposed to the hotter spots seen at the lower corner of the test particle in the MSR reaction applications.

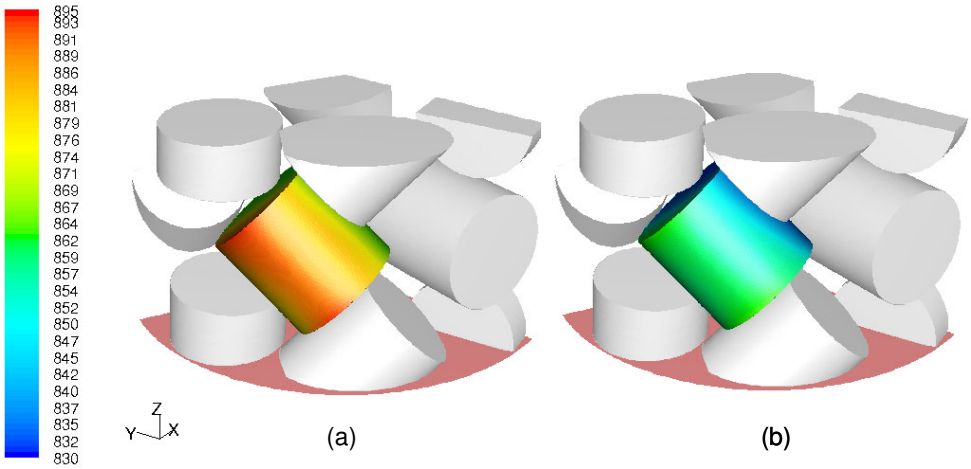

Figure 5.31 Surface temperature contours (K) obtained with the simulations by (a) dilute approximation method, and (b) M-C method.

The intra-particle variations: Figure 5.32 shows the intra-particle temperature variation on planes 1 and 2 for both cases.

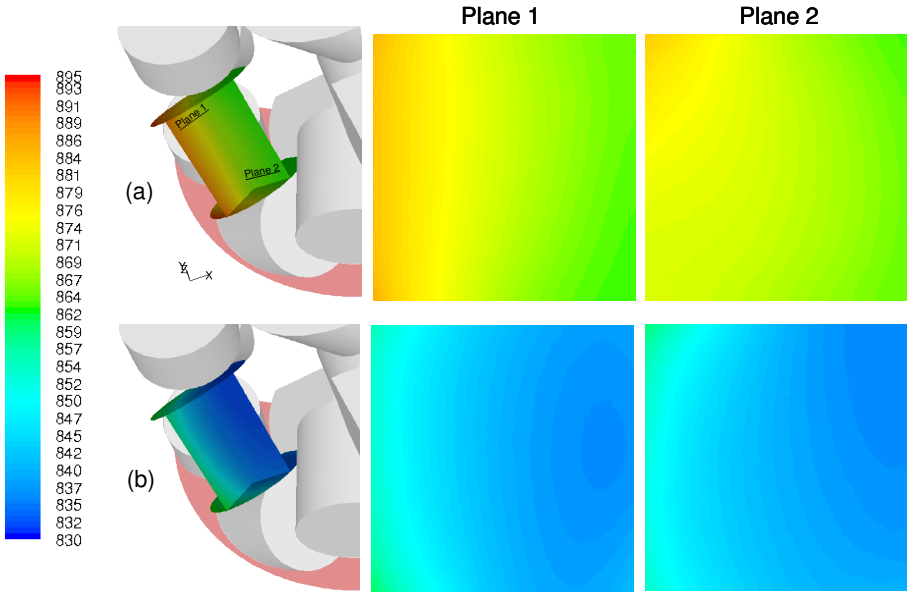

Figure 5.32 Intra-particle temperature contours (K) on the planes 1 and 2 for the simulations of (a) dilute approximation method, and (b) M-C method.

Plane 1 temperature contours of the dilute approximation, as shown in Figure 5.32(a), presented a uniform axial transition throughout the particle. On the other hand, the intra-particle temperature transition was different in the M-C method; the corners stayed at higher temperature, but the central location in the axial direction was cooled down more. The plane 2 contours were similar, and the left section of the particle was hotter than the right section in that plane for both cases. The tube wall heat transfer effect was not expected there; however, due to the lower velocity observed in the fluid near to that part of the surface which did not create a strong resistance between fluid and solid, the temperature stayed relatively closer to the bulk value.

The surface and intra-particle temperatures were lower for the results obtained by the M-S method where 80% more heat uptake was observed.

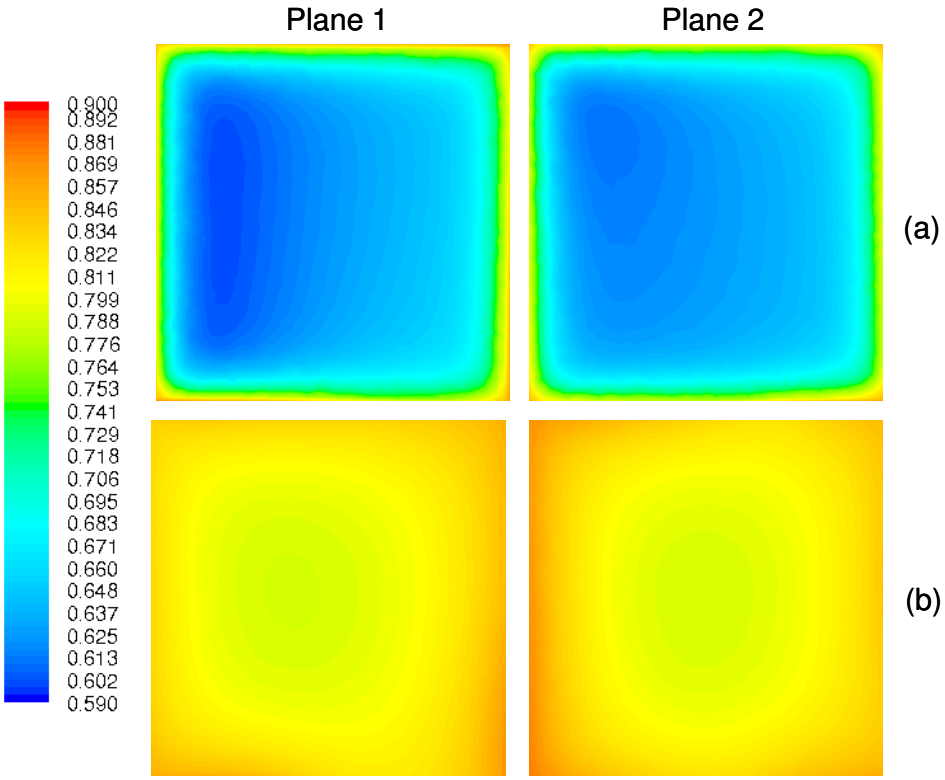

Figure 5.33 Intra-particle C_3H_8 mass fraction contours on the planes 1 and 2 for the simulations of (a) dilute approximation method, and (b) M-C method.

The propane (C_3H_8) mass fraction contours are shown in Figure 5.33 for planes 1 and 2 for both cases. As in the temperature contours, there were significant differences for C_3H_8 mass fraction qualities and quantities for both cases. As a result of high intra-particle temperatures observed for dilute approximation simulations, the C_3H_8 consumption rate was high, and lower mass fractions were observed in most of the particle. The reaction mostly took place in the outer region of the particle; therefore a sudden change was seen in that region. The near wall effect was noticed in the particle close to the tube wall along the particle axis in plane 1. The M-C method simulation results, on the other hand, were quite different, and lower C_3H_8 consumption rate was observed which resulted in higher C_3H_8 mass fraction contours on both planes. The reaction took place inside of the particle not in the outer shell, which presented the higher activity level of the particle with M-C method. Additionally, a more uniform C_3H_8 distribution was seen with the simulations carried out with M-C diffusion method.

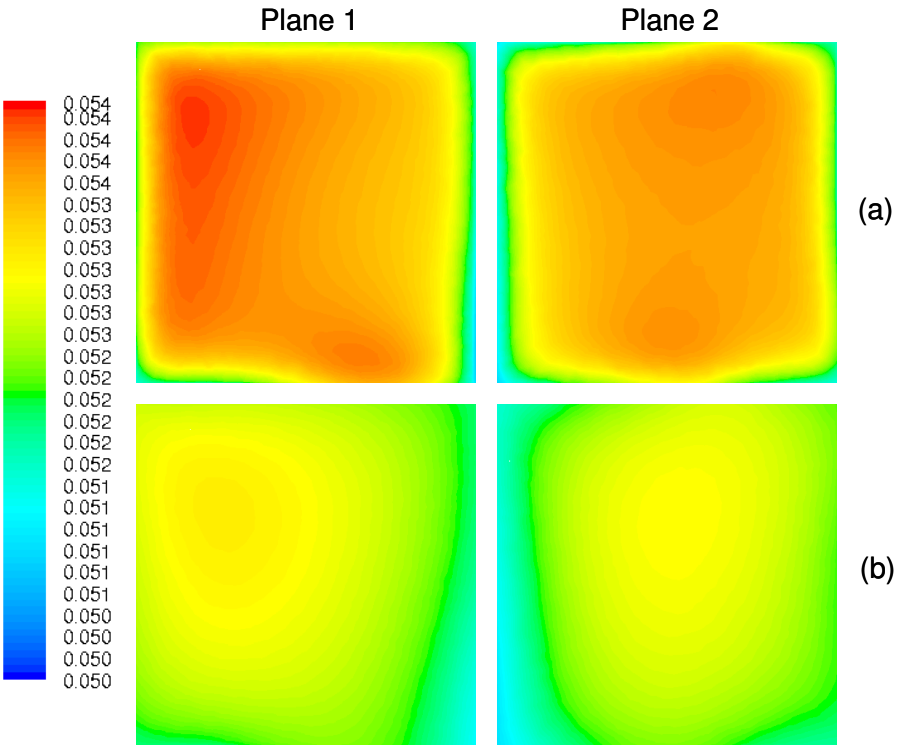

Figure 5.34 Intra-particle H_2 mass fraction contours on the planes 1 and 2 for the simulations of (a) dilute approximation method, and (b) M-C method.

The hydrogen production rate may be compared with the H_2 contours on the same planes for both cases. As expected, more hydrogen production was observed mostly in the outer shell with the dilute approximation method. Whereas the hydrogen mass fractions were low, and the particle was mostly active through its center with the M-C method. However, the H_2 distribution was not as uniform as the C_3H_8 distribution.

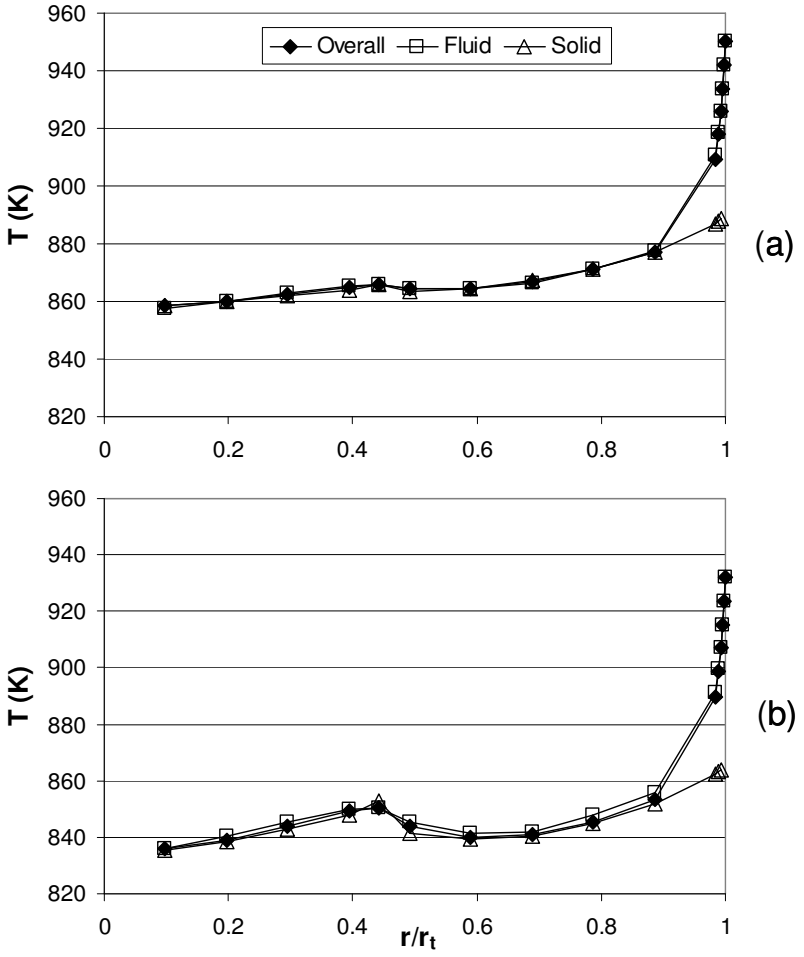

Figure 5.35 Radial temperature profiles for PDH with (a) the dilute approximation, and (b) M-C method simulations.

The radial profiles: As shown in Figure 5.35(a) and (b), the dilute approximation method temperature profiles were higher than the M-C method results as a supporting

observations of temperature contours. For the dimensionless radial position $0.0< r/r_t <0.9$, there were no differences in solid and fluid phase profiles, and in overall profile as a consequence, with the dilute approximation method. There was some difference seen in M-C method results. However, the main discrepancy was noticed in the near wall region between the solid phase and the fluid and overall phase results for both methods. The heat is transferred from the tube wall, and is not carried up as efficiently with the flow convection due to the low velocity flow field. Therefore fluid temperatures stayed high, and as a result of the heat sinks in the solid region due to the endothermic nature of the reaction, solid temperatures kept low in the near wall region. The overall temperatures were almost the same as the fluid phase values in that region, because of having very high local bed voidages explicitly in that area.

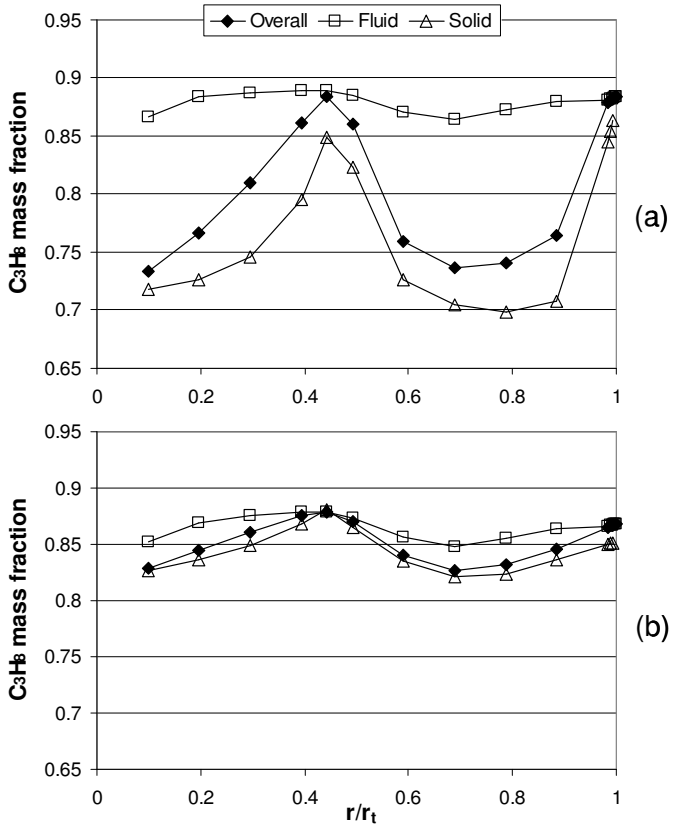

Figure 5.36 Radial C_3H_8 mass fraction profiles for PDH with (a) the dilute approximation, and (b) M-C method simulations.

The propane mass fraction radial profiles are shown in Figure 5.36. At a first glance, strong "S" shape overall and solid region profiles were seen for the dilute approximation results as well as a strong difference between the fluid and solid profiles. Local high voidages at r/r_t =0.44 and r/r_t =0.98 affected the solid phase and overall profiles to create local maxima. The solid and fluid phase profiles were close to each other in M-C method application. These profiles can be coupled to the contour graphs shown in Figure 5.33. The sudden change in the C_3H_8 mass fractions contour graph was noticeable in the radial profiles presented in the Figure 5.36(a) for the dilute approximation method, and the moderate change in the M-C method contour graph was predictable from the radial profiles shown in Figure 5.36(b).

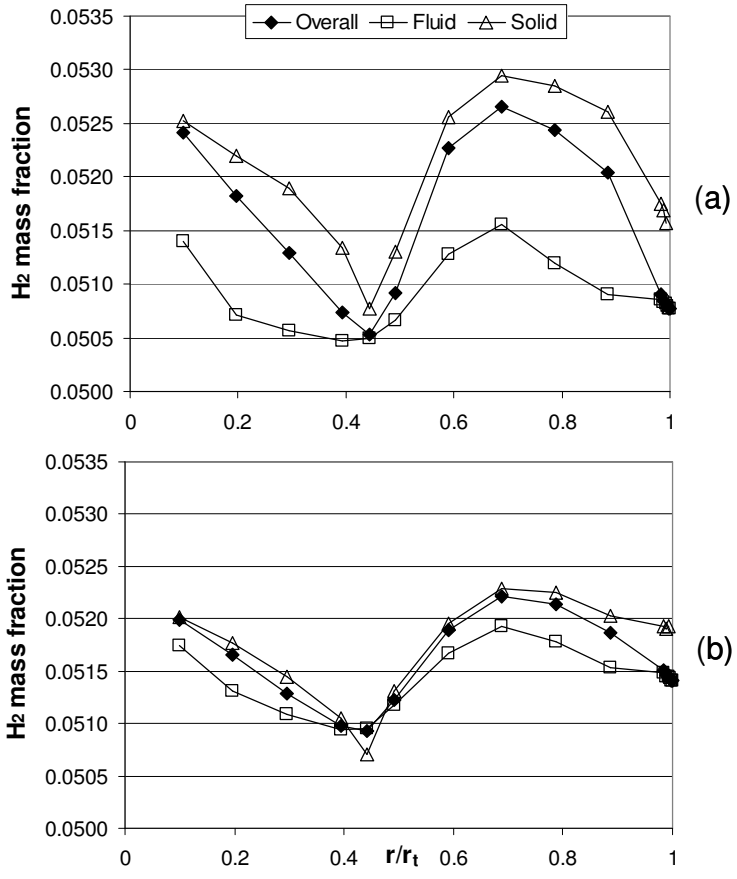

Figure 5.37 Radial H_2 mass fraction profiles for PDH with (a) the dilute approximation, and (b) M-C method simulations.

The hydrogen mass fraction profiles are presented in Figure 5.37. Similar observations were made as for the propane mass fraction profiles, and closer fluid and solid region profiles were seen in the M-C method results. As expected, there was a relation between the hydrogen contour graph and mass fraction profiles shown in Figures 5.34 and 5.37(b).

The effectiveness factor: For dilute approximation method and M-C method results, the effectiveness factors were calculated for front (particle 2) and back (particle 12) particles.

The dilute approximation

$$\eta_{particle-2} = \frac{1.17374\times10^{-3}}{4.86436\times10^{-3}} = 0.2410 \qquad \eta_{rparticle-12} = \frac{1.22889\times10^{-3}}{4.23179\times10^{-3}} = 0.2900$$

M-C method

$$\eta_{particle-2} = \frac{1.89617\times10^{-3}}{2.74443\times10^{-3}} = 0.6910 \qquad \eta_{rparticle-12} = \frac{2.10446\times10^{-3}}{2.66879\times10^{-3}} = 0.7885$$

The higher effectiveness factors were obtained with the M-C method results than the dilute approximation method by almost a factor of 2.8. The effectiveness factor values can be coupled to the intra-particle contours and radial profile observations.

To understand the reason of having different effectiveness factors with dilute approximation and M-C method, the relative sizes of the molecules must be considered. The C_3H_8 and C_3H_6 molecules are alike each other, and much bigger than the H_2 molecule (almost 9 times in molecular volumes). Therefore, the C_3H_8/H_2 and C_3H_6/H_2 binary diffusivity values are much bigger than the C_3H_8/C_3H_6 one. Note that, for the dilute approximation, the effective diffusivities are calculated by considering the molecular and Knudsen diffusivities. So, in dilute approximation case, Knudsen diffusion dominates the effective diffusivity calculations. However, for the M-C method, the effective diffusivities are calculated utilizing the binary diffusivities where molecular difference plays an important role. Therefore, the calculated effective diffusivities for dilute approximation method are order of magnitude smaller than the ones calculated by

FLUENT with only binary diffusivities as given in Table 5.2. As a result of this difference, higher particle effectiveness for M-C method was obtained.

Table 5.2 Effective diffusivities used in different cases (m^2/s)

	Dilute approximation	M-C
$D_{C_3H_8,m}$	$4.2x10^{-6}$	$8.2x10^{-5}$
$D_{C_3H_6,m}$	$3.7x10^{-6}$	$5.0x10^{-5}$
$D_{H_2,m}$	$1.9x10^{-5}$	$2.9x10^{-4}$

Since the species molecular sizes are comparable to each other for MSR reaction compounds, there were no differences observed between the results of different diffusivity settings, and therefore only dilute approximation results were shown in the previous section.

As expressed in the PDH reaction introduction given in Chapter 1, and in the literature overview in Chapter 2, this reaction has been mostly investigated with the coke formation in modeling studies regarding different reactor types than the one used here to increase the yield and conversion. On the other hand, this reaction has been known with the high effectiveness factor, or with the high particle activity (Jackson and Stitt, 2004), and this was the main reason that we have considered this reaction in our study to implement our diffusion/reaction application to a different activity level reaction than the MSR. Although we have not considered different features of this reaction as described above, based on our observations the M-C method may be considered as more suitable selection for diffusive flux modeling in the PDH reaction.

5.5 Conclusions

The diffusion/reaction implementation method has been applied to two different reactions, MSR and PDH, and two different geometrical models with full and 4-hole cylinders packings.

The MSR reaction application results showed strong temperature gradients and induced species fields within the wall particles. Strong diffusion limitations affected the temperature and species parameters to create non-symmetric and non-uniform fields. All these observations were contrary to the conventional assumptions used in reactor modeling. Based on our observations the usage of conventional modeling methods may result in mis-evaluations of reaction rates, and ultimately the design considerations may be affected such as the mis-prediction of the tube lives.

The PDH reaction was considered to study the reaction with lower diffusion limitations. Based on the different diffusion coefficient settings, different particle activity levels, or effectiveness factors were obtained. Regarding the larger molecular sizes of propane and propene as compared to hydrogen, the realistic diffusion modeling would be achieved by the multi-component method where the effective diffusivities calculated by the binary diffusion coefficients.

6. Pseudo-continuum Modeling

The representative reactor models with valid parameters can be invaluable tools for the decision making processes during the design and operation. In real world problems, on the other hand, the time constraints and economic facts force some compromise with ideal models to establish the suitable procedures in design and operation. Therefore up to the present, several types of models have been developed to satisfy the operating conditions as summarized in Chapter 1.

In reality the fixed bed reactor character is heterogeneous, regarding the fluid flow between the catalysts, the transport processes between the fluid and catalyst, and reaction taking place on the catalyst pores. The major flow is in the axial direction, and energy flow can be in both axial and radial directions with the influence of wall heat transfer (Rase, 1990). However, due to the mentioned constraints, to minimize these complexities, simplified models such as pseudo-continuum (P-C) models have been used. Basic reactor simplifications, besides the presented pellet behavior in Figure 5.1, may be additionally illustrated in Figure 6.1 for endothermic conditions.

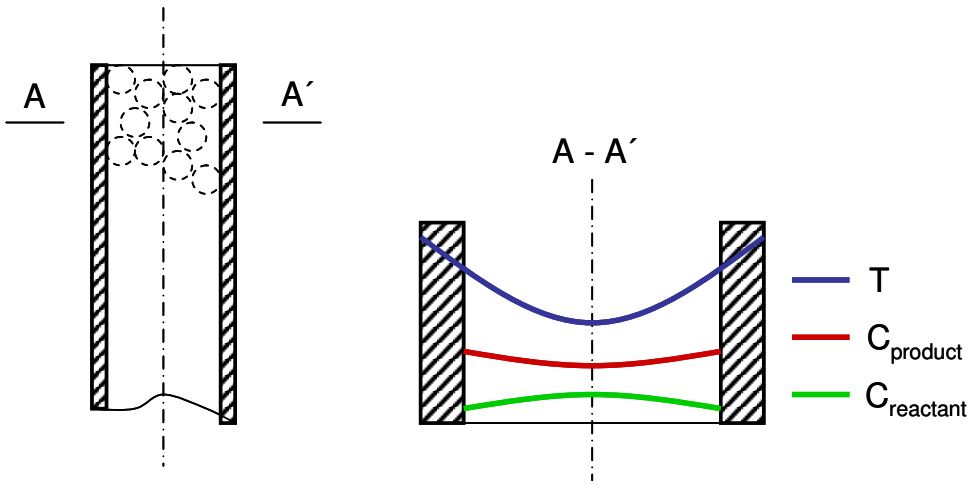

Figure 6.1 Basic reactor simplifications for the endothermic conditions (Re-produced from Rase, 1990).

As presented in the sketch, endothermic reaction heat is removed at the center of the tube, which means that the radial gradient of temperature mostly exists on the tube wall. Because of this gradient, concentration gradients will also occur.

The fluid behavior is usually considered with a constant superficial velocity, or with some general smooth shape radial velocity profiles through the packed bed. For large N (tube-to-particle diameter ratio) tubes, the deviation from a constant velocity is confined to only a small fraction of the cross-section adjacent to the tube wall. Whereas, for the low N tubes, a substantial portion of the cross-section is affected by the wall. A representative plot is shown in Figure 6.2 regarding the flat, correlation based, and DPM results based radial profiles of axial velocities.

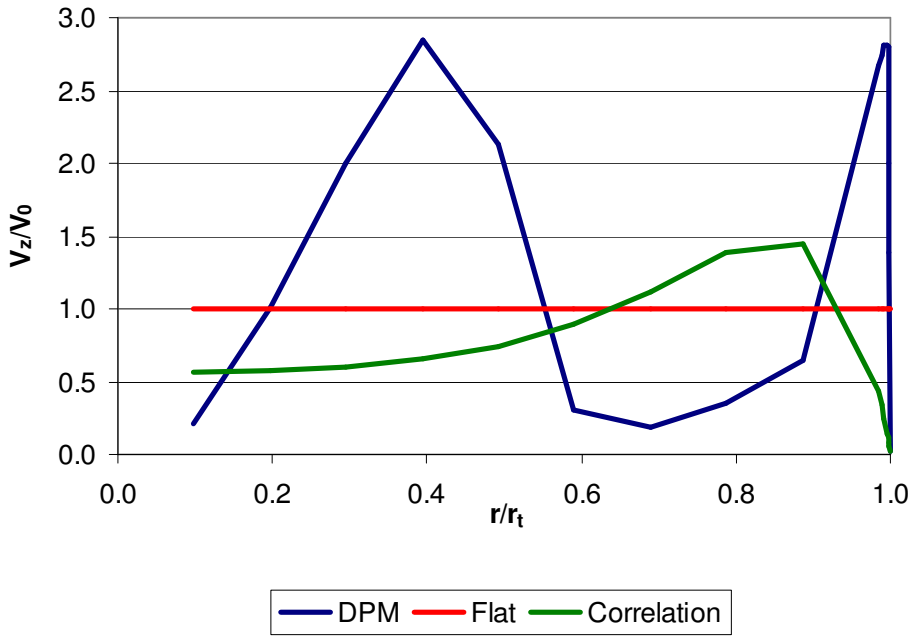

Figure 6.2 Radial profiles of dimensionless axial velocities for flat, correlation based, and DPM results based settings.

The correlation-based smooth curve was obtained from Tsotsas and Schlunder (1988) for which the details are given in Appendix 7(a), and DPM results were from our CFD simulation of full cylinders packing WS model. Although the flat and the smooth curve

velocity profiles cannot exist with the presence of realistic packing, especially for the low N tubes, the influence of the wall region is thought to be lumped into the parameters applicable for heat and mass transfer as a conventional approach. Therefore with these lumped parameters, the near-wall effects are aimed to not to be ignored by the selection of either flat or smooth curve profiles.

Our aim here was to create a best P-C model with the appropriate parameters or correlations to obtain the profiles of the parameters, and compare the energy and species simulation results with previously obtained 3D DPM results by CFD as given in Chapter 5.

6.1 Model development

The P-C models are basically represented by 2D partial differential equations as summarized in Chapter 1, and numerical methods are used to reach the solution. Therefore, researchers mostly create codes in different programming languages to solve these 2D equations.

Since our aim was to establish a comparative study with 3D DPM simulation results, we did not want to introduce scaling problems with the utilization of 2D P-C model. Therefore we have generated a 3D model by GAMBIT as shown in Figure 6.3(a) as a P-C model with just fluid phase as in the conventional approach. The 10 layers of prism structure were implemented on the tube wall with the same features as applied in WS models. The outside of the prism region was meshed with tetrahedral UNS grid elements of 0.000762 m size. Total model size was 350,000 cells. The mesh structure is shown with an enlarged view of an arbitrary section in Figure 6.3(b) for the top surface.

The “velocity inlet” boundary condition was selected for the bottom surface, and “outflow” condition was applied for the top to ensure mass conservation without any additional operating condition setting (i.e. temperature and composition) for the outlet. As in the WS models, the side walls were set as symmetric.

The energy and species simulations were performed by FLUENT 6.2.16 with the pre-defined velocity profile. For a flat profile, as in Figure 6.2, the constant superficial velocity was defined for all the computational cells. For the radial position dependent curves, shown in Figure 6.2 as smooth curve and DPM, a user-defined code was prepared to express the correlation or radial-position-dependent velocity function, and defined within each computational cell by just one momentum iteration. The reason for that iteration was not to solve the flow, but to propagate the radial position dependence of the local superficial velocities on each cell.

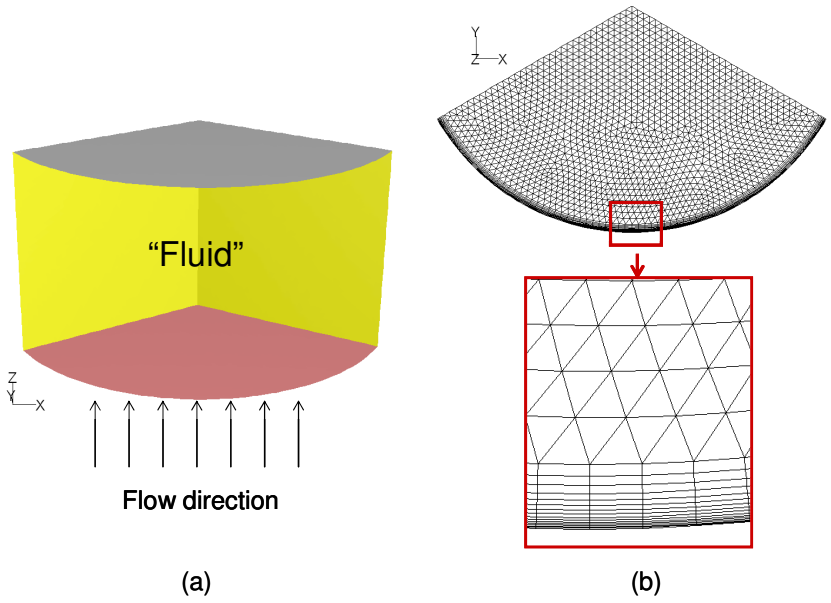

Figure 6.3 3D P-C model (a) general view, and (b) mesh structure.

Except for the thermal conductivity, the same fluid properties and reactor operating conditions were used as given in Table 3.1. For the thermal conductivity we have either used a constant effective value (k_{er}), or a radial k_{er} profile.

6.2 Thermal conductivity determination

In order to obtain the most appropriate P-C model, different correlations were selected from literature to calculate and define different operating conditions and effective

transport parameters. For the k_{er} determination, a separate study was carried out where only wall heat transfer was considered, and the obtained radial temperature profiles with different velocity settings were compared to the DPM results

Case-1: The first case was to consider the constant k_{er} value for entire domain. To calculate alternative k_{er} values, the prediction methods defined by Dixon (Dixon and Cresswell, 1979; Dixon, 1988), and Bauer and Schlunder (1978a, 1978b) were utilized. The details of correlations are given in Appendix 7(b). Similar values were calculated with the both methods as 87.4 w/m-K from Dixon, and 84.0 w/m-K from Bauer and Schlunder.

The temperature profile was obtained utilizing the flat velocity profile as shown in Figure 6.2, and Dixon's correlation result for the k_{er}. Figure 6.4 represents the comparison of this temperature profile with the DPM result. As can be seen, the Case-1 temperatures in the core of the bed were in quite good agreement, whereas at the near wall region, the DPM predictions were not captured by the constant k_{er} setting. Obviously, the near wall heat transfer phenomenon was not defined in the P-C model with the constant velocity and thermal conductivity settings.

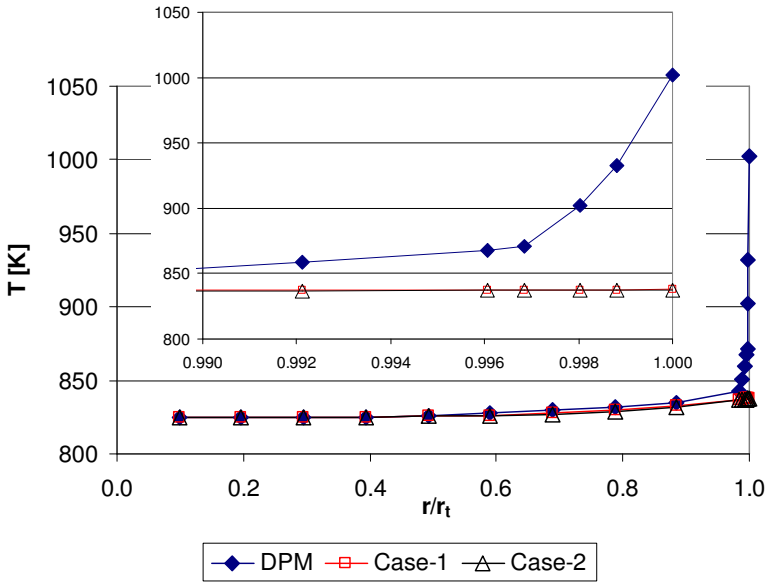

Figure 6.4 Radial temperature profiles based on DPM, Case-1, and Case-2 results.

Case-2: To be able to capture the near wall heat transfer phenomenon, a smooth curve velocity profile, shown in Figure 6.2, was utilized instead of using flat velocity profile. This application was carried out by a user-defined code, as given in Appendix 7(a). The resulting temperature profile was also shown in Figure 6.4, and apparently no significant improvement was observed. From Case-1 and Case-2 results, although the smooth curve velocity profile provided a viscous damping near the wall, the limiting factor seemed to be the k_{er} setting.

Case-3: Instead of using the constant k_{er} value, the Winterberg and Tsotsas (2000) correlation was utilized to obtain the effective thermal conductivity curve. The details of the correlation and the prepared user-defined code to define the correlation into FLUENT are given in Appendix 7(b). Authors considered two parameters, the slope parameter K_1 and the damping parameter K_2, in their expressions which are not à priori fixed, but subject to determination by comparison of the results obtained by this correlation and available experimental data. It was additionally noted that, different pairs of K_1 and K_2 may be almost equally successful in describing the same experimental data. Therefore we have considered three different pairs of K_1 and K_2, and the results are shown in Figure 6.5 along with the DPM results. The results obtained with the pair (b) captured the fluid temperature adjacent to the tube wall, however it was not successful at the dimensionless radial position of $0.900 < r/r_t < 0.998$. The pair (c) and DPM results were mostly in agreement, however, near wall effects could not be predicted in spite of the slight improvement as compared to Case-1 and Case-2 near wall region results. The results obtained by pair (a) were in between the other pairs.

Generally, the benefit of the effective thermal conductivity correlation was seen with this application. We have better results than the constant k_{er} setting, at the near wall region, and the core of the tube modeled well, as expected and observed in the other cases.

The sudden temperature increase in the near wall region of DPM must be related to the boundary layer resolution, which must be coupled to the sudden damping in the DPM velocity profile at that region as shown in Figure 6.2. Therefore, the next step would be the consideration of DPM velocity profile.

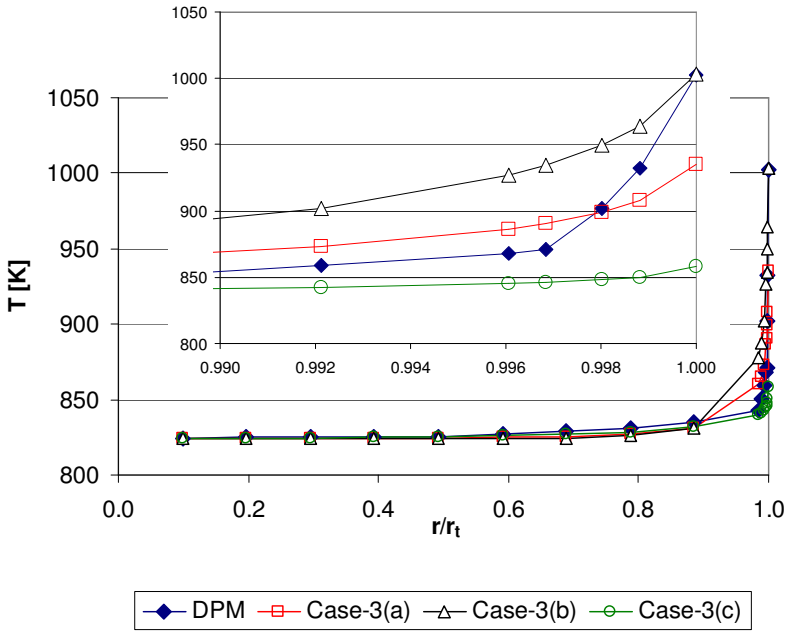

Figure 6.5 Radial temperature profiles based on DPM, and Case-3 results.

Case-4: The DPM velocity profile was exactly reproduced by polynomial functions, and set into FLUENT by a user-defined code which is given in Appendix 7(a). Similarly, three different pairs of K_1 and K_2 were considered, and the obtained temperature profiles are shown in Figure 6.6.

The results obtained by the pair (b) captured the fluid temperature adjacent to the tube wall, and better temperature values were seen in $0.900 < r/r_t < 0.998$, as compared to the Case-3. The maximum deviation was less than 40 degrees at $r/r_t = 0.997$. On the other hand, pair (c) captured the near wall temperatures very well up to $r/r_t = 0.997$. However, at $r/r_t = 0.999$, 80 degrees difference was observed with the DPM results. Pair (a) can be

considered as one of the optimum profiles to compensate for the deviations mentioned for pairs (b) and (c).

Additionally, at r/r_t = 0.9, a slight disagreement was noticed between the DPM and all the pair results. In spite of that, the most representative temperature profiles were obtained utilizing the DPM-fitted velocity profile, and the k_{er} profile.

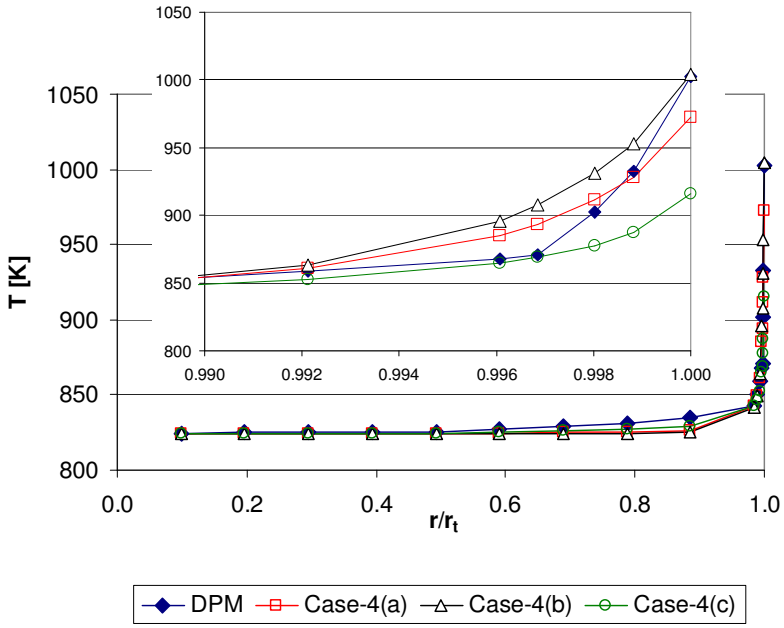

Figure 6.6 Radial temperature profiles based on DPM, and Case-4 results.

6.3 P-C modeling for MSR reaction

The MSR reaction was introduced in P-C modeling with a similar user-defined code as was utilized in DPM simulations with source/sinks terms to express the effects of reaction on temperature and species quantities. The important difference in P-C modeling was that these source/sinks terms were considered for the entire fluid domain and the calculations incorporated the pseudo-solid phase by the bed voidage term, $[1-\varepsilon(r)]$, in the source/sinks terms as expressed below for the energy and species balance equations:

$$u_s \rho c_p \frac{\partial T}{\partial z} - k_{er}\left(\frac{\partial^2 T}{\partial r^2} + \frac{1}{r}\frac{\partial T}{\partial r}\right) = \rho_B (-\Delta H) r_A \eta [1-\varepsilon(r)] \quad (6.1)$$

$$u_s \frac{\partial C}{\partial z} - D_{er}\left(\frac{\partial^2 C}{\partial r^2} + \frac{1}{r}\frac{\partial C}{\partial r}\right) = \rho_B r_A \eta [1-\varepsilon(r)] \quad (6.2)$$

The right hand side of the equations (6.1) and (6.2) is the source/sinks term which was defined by a user-defined code. Additionally we have introduced another term, effectiveness factor, η, in our P-C model to express the diffusion limitations. As a reminder, from DPM simulations we have obtained different effectiveness factor values for front (number 2) and back (number 12) particles, as well as the effectiveness factor profile as shown in Figure 5.18. We have used all three of them separately in this part of the work to make a comparison.

The effective diffusivity (D_{er}) values were calculated form correlations provided by Specchia et al. (1980), Bauer and Schlunder (1978a; 1978b), and Rase (1990), and found to be 0.002150, 0.005659, and 0.007485 m^2/s respectively. Details of these correlations are provided in Appendix 7(c). The results were not significantly affected when these different values were used as effective diffusivities in P-C modeling.

In general, the main modeling parameters can be considered as velocity, effective thermal conductivity, effective diffusivity, bed voidage, and effectiveness factor. Either constant values or spatial functional terms are utilized for these parameters. Since we have previously investigated the velocity and k_{er} parameters, a further consideration was carried out for the effectiveness factor and bed voidage in this section. The energy and species solutions were reached with the residuals in the order of 10^{-8} within a few iterations (~20).

The effectiveness factor investigation: Although the most suitable velocity and k_{er} settings were already seen in the previous section, as the basic application in the P-C modeling, a flat velocity profile, constant effective parameters and bed voidage were utilized in this investigation. For k_{er}, the value obtained from Dixon correlation, for the bed voidage the value of WS model with full cylinders packing, and for the D_{er} the one

obtained by Bauer and Schlunder correlation were utilized. As a result of the energy and species simulations, the obtained overall heat uptake values (Q), tube wall temperatures (TWT) and methane conversions (X_{CH4}) are given in Table 6.1 with the DPM results to make a comparison. Equation (2.2) was used for the X_{CH4} calculations. The temperature and, methane and hydrogen mass fraction profiles are presented in Figure 6.7.

Table 6.1 P-C modeling results for different effectiveness factors, and DPM results.

	η-front particle	η-back particle	η-profile	DPM
Q [w]	214.5	288.5	215.0	253.2
TWT [K]	836.2	835.6	836.4	1004.8
X_{CH4} [%]	0.356	0.488	0.354	0.530

The DPM TWT value was not reached by any P-C model as a consequence of flat effective thermal conductivity and axial velocity profiles. Although the overall heat uptake value of DPM was not reproduced, comparable values of Q were obtained with different effectiveness factor settings. If we compare the front and back particle results, we see a reduced heat uptake as a result of lower η-front particle. This can be explained with the influence of the reduced effectiveness factor on the RHS of the equation (6.1). The higher diffusion barrier due to the lower η reduces the reaction heat effect, and therefore less heat is transferred into the pseudo-positioned particles to establish the energy balance. The η-profile heat uptake value was quite similar to the η-front particle value, although the profile was obtained considering both the front and back particle reaction rates. Figure 5.18 shows the possible reason for this observation. At the dimensionless radial position of $0.85 \leq r/r_t \leq 1.00$, the local effectiveness factors were lower than the front particle values, as noted in section 5.3.1.2. Because of this, the reaction heat effects were reduced as compared to the ones obtained by the constant front and back particle effectiveness factor settings in that particular position. Therefore, as a result of the contribution of the reduced heat effects in that region to the total heat uptake,

the higher heat effects due to the η-back particle were lost with the utilization of the η-profile, which resulted in very similar heat uptake values with the η-front particle simulation.

The DPM heat uptake value, which was found to be in-between the front and back particle results, could not be obtained by the η-profile setting, although the near wall particle effectiveness was defined by that profile. This situation might be understood well when the tube wall temperatures were compared. Obviously, the near wall temperature field of DPM was not reproduced by any effectiveness factor setting as a result of not using the suitable effective thermal conductivity. The temperature profiles shown in Figure 6.7(a) represent this situation. Actually, with the parameters used in this investigation, the entire DPM radial temperature profile was not obtained. We have selected the basic, and frequently addressed P-C modeling parameters, and it was clear that, the DPM and P-C predictions were not in agreement.

Although the reactor models that we have been considering in our studies are too short in length to obtain a comparable conversion value with any experimental or industrial data, we have utilized the methane conversion as another control parameter for P-C model testing. It was observed that the conversion obtained with the η-back particle simulation was the closest one to the DPM results with 8% deviation.

Figures 6.7(b) and (c) represent the P-C modeling results of CH_4 and H_2 mass fractions respectively. The DPM profiles shown in the figure were only the bulk fluid mass fractions, as previously shown in Figure 5.14 with overall and porous pellet profiles. Since the P-C model essentially considers only the fluid region, the overall or porous pellet profiles were not the appropriate parameters to make a suitable comparison. The mass fraction profiles obtained from the P-C models with different effectiveness factors were not in agreement with the DPM profiles, and they were almost constant. The lower CH_4 and higher H_2 mass fractions were noticed for the η-back particle simulations as compared to the η-front particle and η-profile results, as a consequence of higher effectiveness value.

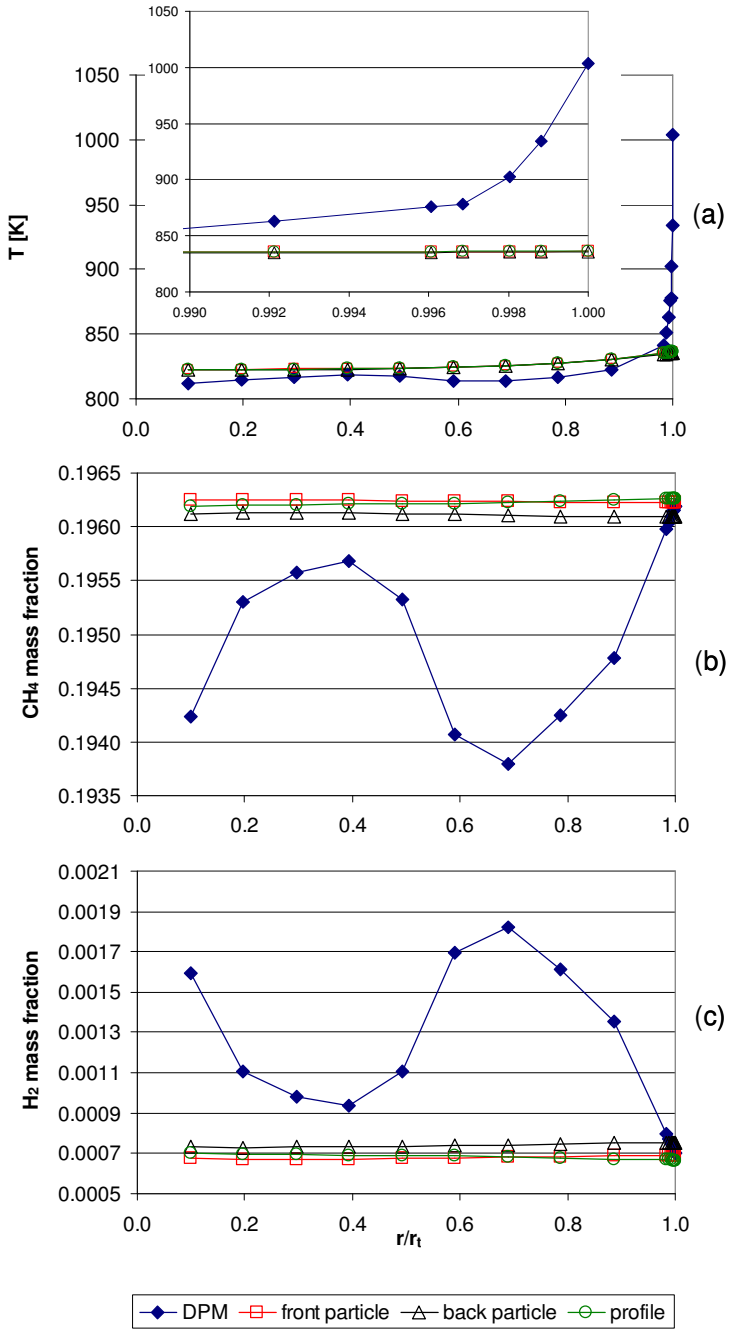

Figure 6.7 The radial profiles of (a) static temperature, (b) CH_4 mass fraction, and (c) H_2 mass fraction obtained by the P-C model with different effectiveness factor settings.

By this investigation, different effectiveness factors were compared to each other and to DPM results while considering constant effective parameters. As a next step, the bed voidage correlations were considered to create radial profiles instead of using constant values.

The bed voidage parameter investigation: The same velocity, thermal conductivity and effective diffusivity values were utilized as before. The η-profile was applied to define the diffusion limitations. The bed voidage correlations provided by Winterberg and Tsotsas (2000) and Bey and Eigenberger (2001) were considered. In addition to these correlations, the DPM bed voidage profile was re-produced by fitted polynomial functions and applied by a user-define code into the P-C model. The details of the correlations and the code are given in Appendix 7(d). The obtained voidage profiles are shown in Figure 6.8. The DPM profile presented in the figure is the one obtained from WS model, and the reproduced one by the polynomial functions was exactly the same.

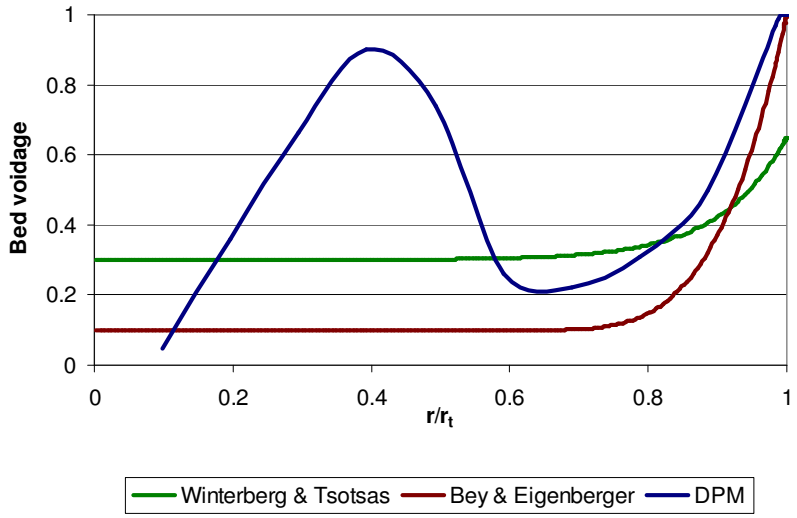

Figure 6.8 Radial bed voidage profiles obtained by the correlations, and from DPM.

As can be seen from the above figure, none of the correlations created a representative bed voidage profile. Both of them created flat profiles at the core and, an increasing trend at the wall region. The Winterberg and Tsotsas (W-T) correlation estimated very low

maxima near the wall as compared to the DPM bed voidage. The Bey and Eigenberger (B-E) correlation captured the full void region near the wall, but a steep decrease was observed for the latter part. Actually, the B-E correlation consists of two different expressions for the wall and the core regions. The bed voidage value at the center of the model can be set to a higher value than the minimum, which occurs radially almost at the half of the bed. By doing that, a sinusoidal curve would be obtained in the core of the bed, However, as can be seen in Figure 6.8, the minimum occurs at the core of the bed, not at $r/r_t \approx 0.65$ in DPM. Therefore, the core and the half of the bed voidage values were kept the same, which created a flat profile in the core.

The P-C model results with these three different bed voidage settings were compared to the DPM results in Table 6.2 for Q, TWT, and X_{CH4} values, and in Figure 6.9 for radial temperature and species profiles.

Table 6.2 P-C modeling results for different bed voidages, and DPM results.

	Winterberg & Tsotsas	Bey & Eigenberger	DPM-fitted	DPM
Q [w]	274.0	329.7	221.9	253.2
TWT [K]	835.9	835.8	836.4	1004.8
X_{CH4} [%]	0.450	0.523	0.360	0.530

The heat uptake result obtained by the P-C model with W-T correlation was lower than the one obtained by B-E correlation. The higher voidage profile obtained by W-T correlation in the core of the bed had an inductive effect on the right hand side of the equation (6.1), which reduced the magnitude of the source term. As a result of that, the reaction heat effects were reduced, and lower Q value was reached by W-T correlation.

W-T and B-E correlation models predicted 8% and 30% more heat uptake values than the DPM result respectively, whereas the value obtained by the DPM-fitted voidage

profile was lower than the DPM value by 12%. On the other hand, B-E correlation predicted the closest methane conversion value to the DPM result.

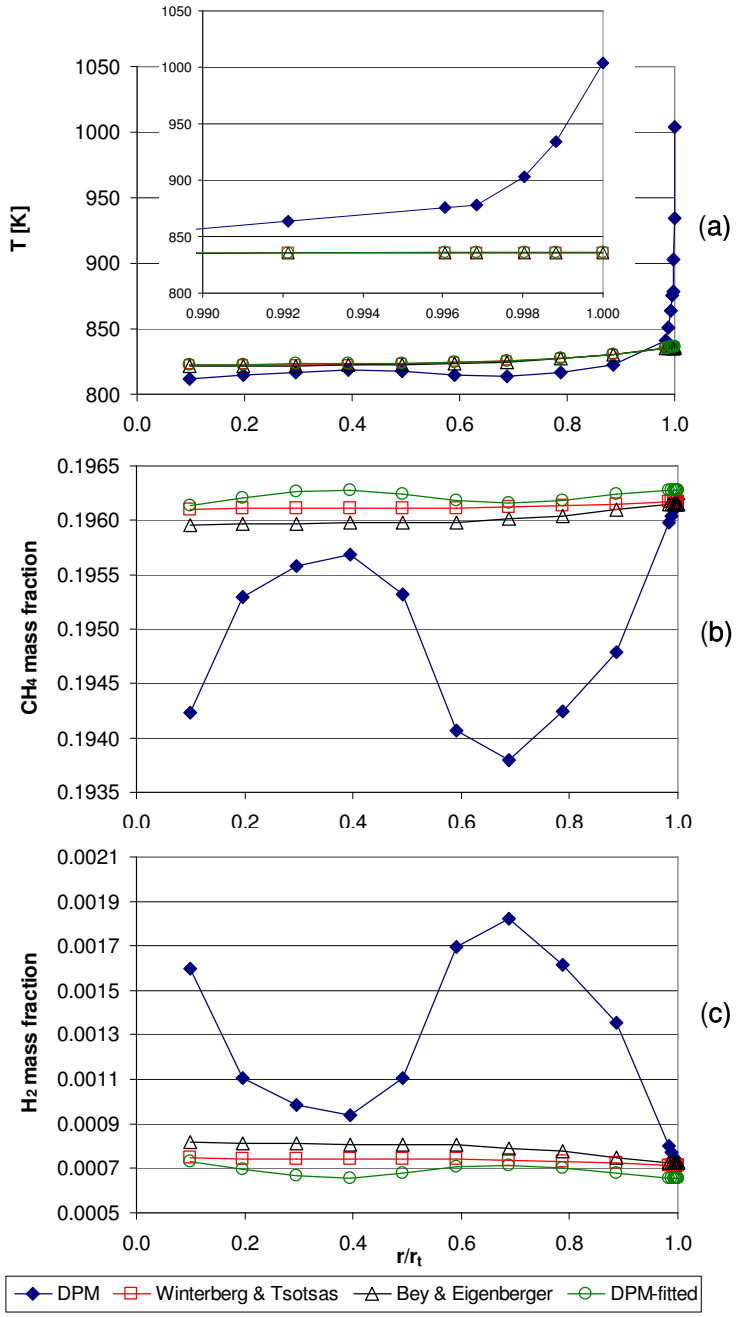

Figure 6.9 The radial profiles of (a) static temperature, (b) CH_4 mass fraction, and (c) H_2 mass fraction obtained by the P-C model with different bed voidage settings.

The TWT values and temperature profiles were different from the DPM results, as observed before.

There were slight effects of the B-E correlation on the methane and hydrogen mass fraction profiles as shown in Figure 6.9 (b) and (c) especially at the near wall region as a result of the sharp damping created there. Since the near wall bed voidage was not pronounced that much with W-T correlation, no significant variation was observed on the related profiles. Although the strong S-shape profiles were not captured, the more variation in the mass fraction profiles was seen for the DPM-fitted model predictions.

At the end of the bed voidage parameter investigation, the DPM-fitted profile was selected for the next stage where the most representative P-C model was aimed to be produced by considering the appropriate effective thermal conductivity and the DPM-fitted parameters.

The P-C model with DPM-fitted parameters: To reproduce the averaged results of the DPM, the DPM-fitted profiles were utilized for the parameters. Axial velocity and bed voidage radial profiles were already obtained above from the DPM-fitted polynomial functions. Additionally, the effective diffusivity profile was created from the DPM as shown in Figure 6.10 by taking the mass fraction weighted average of each species. The blue line presented in Figure 6.10 was reproduced by polynomial functions, and set to the P-C model with a user-defined code, which is given in Appendix 7(c).

Previously obtained effectiveness factor profile, η-profile, and the thermal conductivity profile (Winterberg and Tsotsas, 2000) were utilized. Based on the three different K_1 and K_2 pairs, the obtained Q, TWT and X_{CH4} values are given in Table 6.3 and, the temperature and methane and hydrogen profiles are shown in Figure 6.11 with the DPM results for comparison.

The heat uptake values of the P-C models were close to the DPM value with 7.5% maximum deviation. The averaged TWT was exactly re-produced by P-C (1) model where the Q value was 5.3% lower than the DPM result. In order to obtain a close Q

value to the DPM result, the P-C (2) model was created with different K_1 and K_2 pairs, which increased the TWT by 100 degrees. One can conclude that, when the DPM Q value was asymptotically reached in the P-C model with different K_1 and K_2 values, the TWT would exceed the DPM predictions by hundreds of degrees. Another parameter pair was utilized to create the P-C (3) model, which predicts the lower TWT. Although the TWT predictions were strongly affected by different K_1 and K_2 pairs, the least influence was seen on the methane conversion predictions, and the maximum deviation form DPM prediction was found as 0.082%.

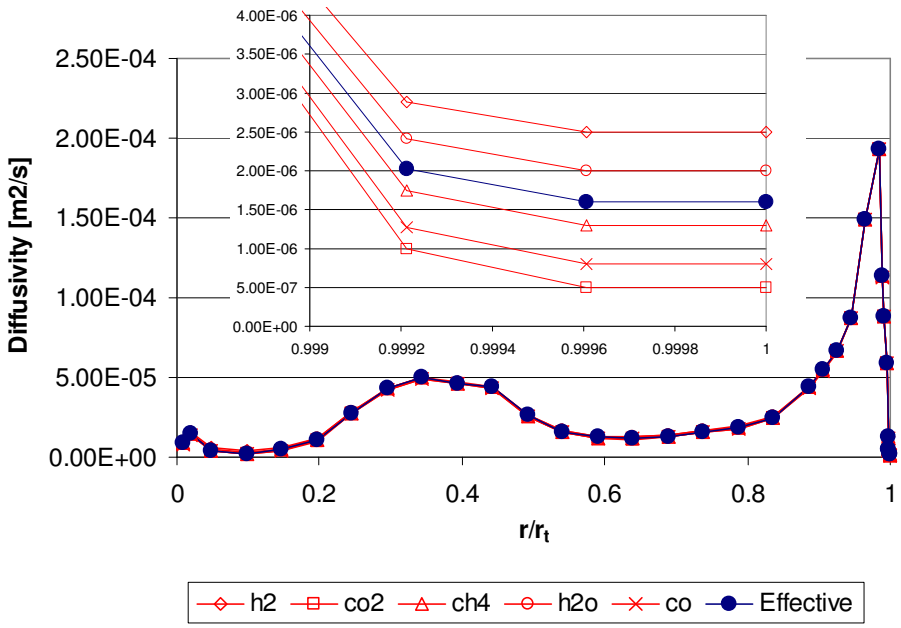

Figure 6.10 The species and effective diffusivity profiles obtained from the DPM.

Table 6.3 P-C modeling results with DPM-fitted parameters, and DPM results.

	P-C (1)	P-C (2)	P-C (3)	DPM
Q [w]	239.8	245.0	234.1	253.2
TWT [K]	1004.3	1104.1	876.4	1004.8
X_{CH4} [%]	0.600	0.596	0.612	0.530

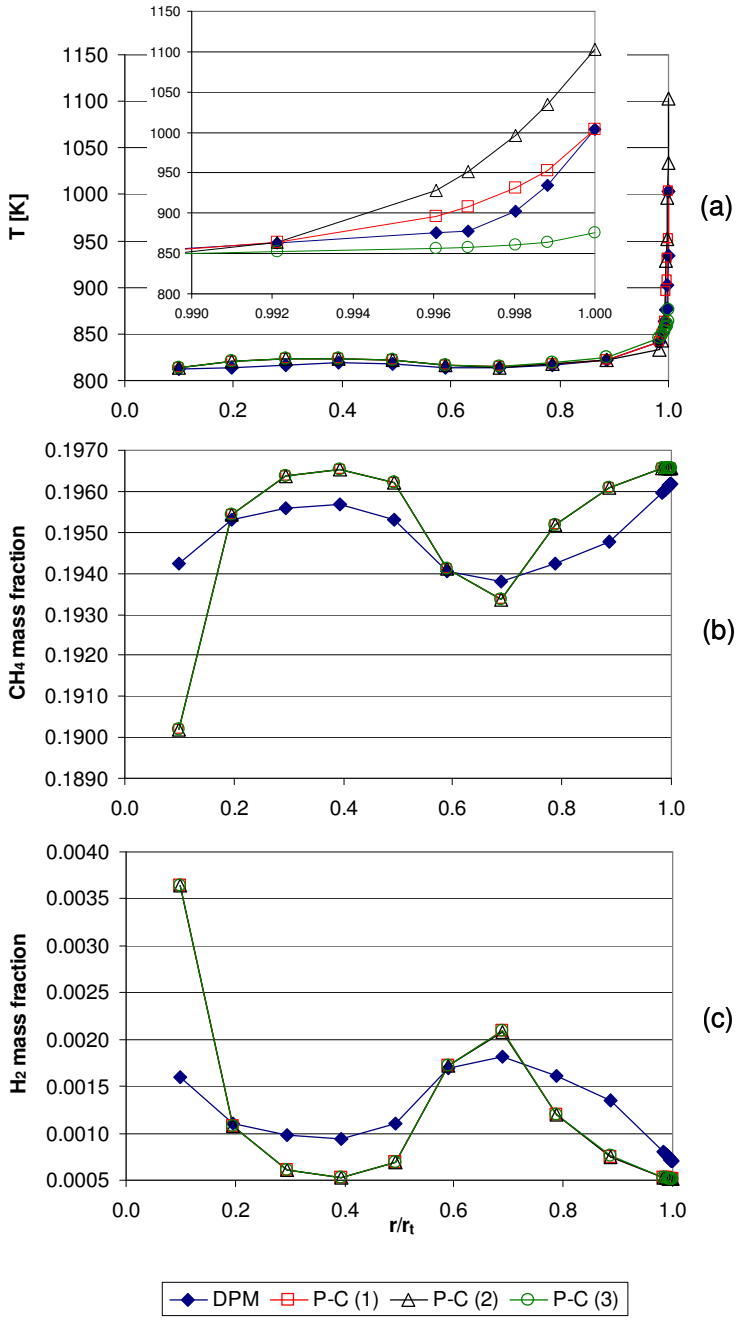

Figure 6.11 The radial profiles obtained by the DPM-fitted P-C models.

The temperature profiles, shown in Figure 6.11(a), were almost the same for all P-C models, and were in good agreement with the DPM profile. The near-wall deviation was enlarged, and the well-established TWT result was additionally seen for P-C (1) in the figure. The local deviation between the P-C (1) model prediction and the DPM profile at $0.996 \leq r/r_t \leq 0.999$, was around 20 to 30 degrees, and this was the best agreement for near-wall performance among the all P-C models considered so far. The over prediction of the P-C (2) model, and the under prediction of the P-C (3) model was observed at the near wall region which can be incorporated to the TWT values.

Although the increase in TWT is related to the total heat uptake, as creating a driving force between the bulk fluid and the wall temperatures to increase the heat transfer rate which ultimately increases the heat uptake as result of the endothermicity, the higher TWT values were not reflected by the heat uptakes in the same order of magnitude. This is because the local temperature deviation between the P-C models appears only at $0.996 \leq r/r_t \leq 1.000$, and the same temperature field is present for the rest.

The P-C model methane and hydrogen mass fraction profiles were no different than each other, and in good agreement with the DPM profiles as shown in Figure 6.11(b) and (c). When the profiles obtained here were compared to the other profiles presented in Figures 6.7 and 6.9, a drastic difference can be noticed. The reason for capturing the DPM prediction was because of considering the DPM-fitted effective diffusivity profile instead of the flat profiles. The strong S-shape P-C model mass fraction profiles were departing from the DPM results at the core of the bed. After careful investigation, this situation was understood as an artifact created by the lower velocity field at the center of the tube regarding the applied DPM-fitted axial velocity profile. In the DPM model, the velocity profile was obtained considering the entire radial surface with both fluid and solid regions, and lower bed voidage values were obtained in the core of the bed as presented in Figure 4.16(b) for the full cylinders WS model. Therefore, the contribution of zero velocities from the solid region reduced the averaged velocity value. In P-C modeling when the DPM-fitted axial profile was applied, the reduced velocity value at

that radial position was literally considered as a velocity field. So this results in the reduced effect of the first term given in the left hand side of the equation (6.2), on the species balance. Thus, the diffusive flux was the only effective term to balance the source term. The lower bed voidage and higher effectiveness factors at the core of the bed created a higher source term, and as a result, a higher composition difference. For this reason, the higher methane consumption, and higher hydrogen production were seen at that radial position. Although the effective diffusivity value at the core was an order of magnitude higher than the one of the near wall region, it was not enough to compensate for the increase in the source term to keep the compositions unaffected.

6.4 Conclusions

The comparative study was carried out regarding the pseudo-continuum (P-C) and discrete packing models (DPM). Different correlations were utilized in order to express the velocity, thermal conductivity, bed voidage, and diffusion coefficients in the P-C models either in the form of flat profiles (constant values) or in the form of expressions to define the radial position dependence.

It was observed that the flat or correlation-based effective parameter profiles were not enough to express the features of the DPM in terms of heat uptakes, tube wall temperatures, species conversions, and radial temperature and species profiles.

To create the most representative P-C model, the DPM-fitted parameters were utilized, and comparable results were obtained to the DPM predictions. It was seen that the temperature profiles were very much affected by the velocity and thermal conductivity definitions. On the other hand, species profiles were significantly influenced by properly defined effective diffusivity profiles.

The final conclusion would be that the pseudo-continuum models cannot fully reproduce the DPM results due to the complex model structure which cannot be represented by the correlations or DPM-fitted expressions in a simplified model.

7. Conclusions and Recommendations

7.1 Conclusions

At the end of this written document, we can evaluate our observations based on the different phases of the research regarding the main goal that we had in our minds at the beginning. Therefore, the interim conclusions reached at the end of the chapters will not be repeated here, and the observations will be expressed with a global point of view of the research.

Our objective was to investigate the interaction between the chemistry taking place in the particle, and the transport processes surrounding it for the low-N fixed bed tubes utilizing the CFD. Regarding the consequences of wall heat transfer in low-N tubes that have been expressed in the problem statement, generating the proper 3D geometry was the first cornerstone of our work. For this reason we have validated our smaller size geometry, which was selected due to the computational constraints.

The pseudo-continuum type of packed bed models do not account for the actual environment for the reacting particles, and therefore, almost always symmetric and sometimes uniform temperature and species distribution is assumed inside of the pellets. In our work, utilizing the benefits of the CFD, the diffusion/reaction has been introduced into the pellets within the realistic 3D reactor conditions, and contrary to the conventional approach, the non-symmetric and non-uniform intra-particle temperature and species variations have been obtained for the near wall particles, and extensively investigated in detail for the first time.

Furthermore, it has been shown that, the strong near wall gradients as observed by discrete packing models, either approximating the reaction heat effects or implementing the diffusion/reaction into the catalyst particles, cannot be captured by the simplified pseudo-continuum models.

The significance of our observations is that utilization of the conventional simplified methodology will definitely lead to an incorrect evaluation of the reaction rates, and consequently the design considerations such as tube wall temperature and pellet and reactor dimensions.

The strong impact of our findings must be expected on fundamental reaction engineering by moving away from empiricism towards a more rigorous treatment of the pellet, and on the industry by preventing the tube failure and obtaining improved reaction conversion, thus having positive consequences for the plant safety and efficiency, and for pollution prevention and sustainable engineering regarding the particular importance of methane steam reforming on the hydrogen economy.

7.2 Recommendations

In this section, we will describe some of the research areas either we have touched but not completed, and thus have not discussed in the main body of the text, or came to our attention but they were either not part of the main focus of this work or time/computational resources were not available to spend more effort on them.

7.2.1 Particle orientation

Diffusion/reaction implementation was done on the specific WS model where the test particle was located in 45 degree rotated form close to the tube wall. To answer the question if the orientation of the test particle would be important for the near wall transport processes, we re-considered the previously created WS models with different test particle orientations (Nijemeisland, 2002) with improved mesh structure on the wall-fluid contact areas by prism layers. Additionally, another WS model was generated to consider, in general all the possible basic particle placements as presented in Figure 7.1. The model numeration was started from two, regarding the model with 45 degree rotated test particle as WS-1.

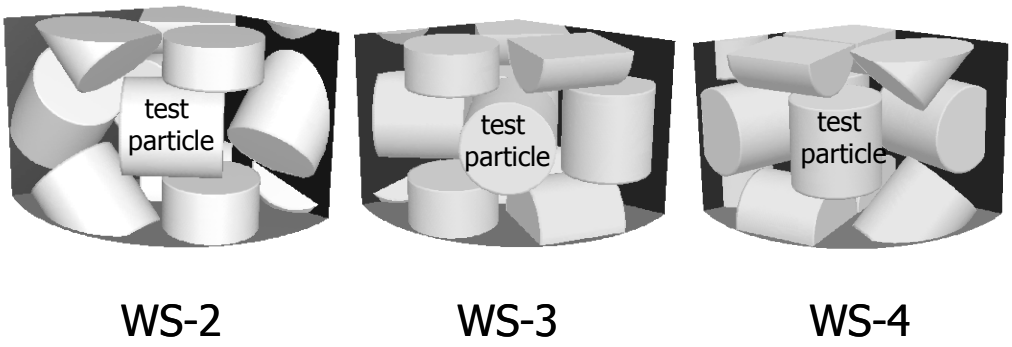

Figure 7.1 Different WS models

We have obtained the preliminary results for WS-4 model, and surface and intra-particle temperature variation is shown in Figure 7.2.

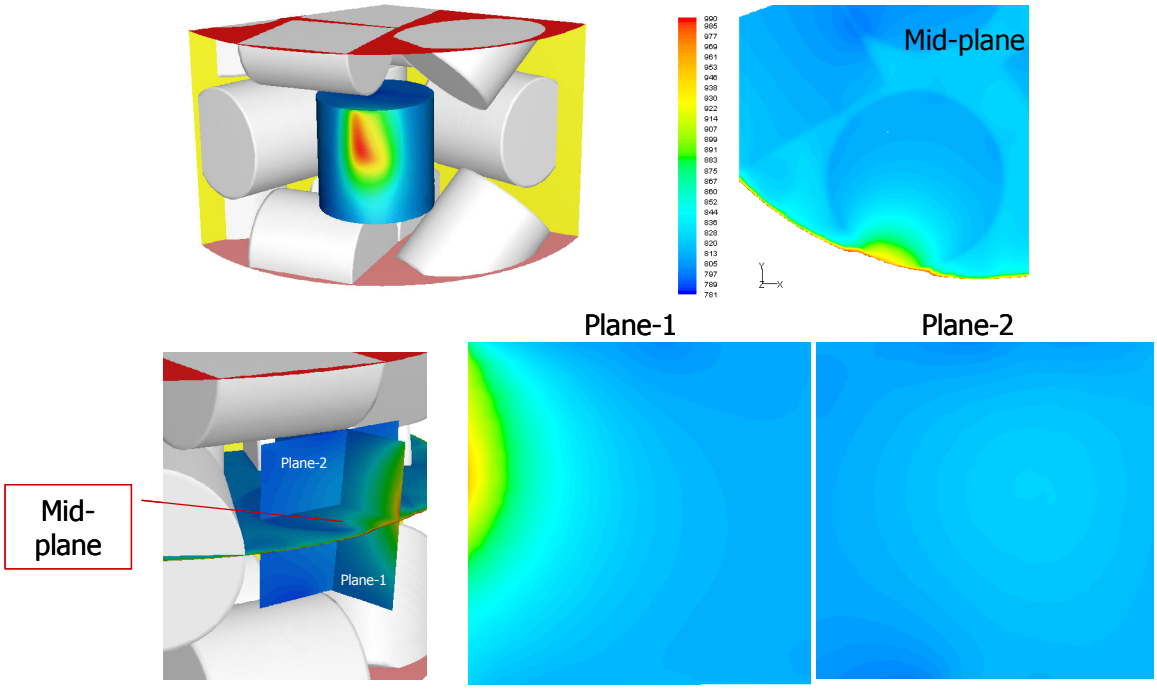

Figure 7.2 The preliminary temperature contours of test particle, model WS-4.

We have observed similar hotter sections as seen on WS-1 model test particle surface at the closest section to the tube wall. Obviously, the flow convection, which takes place between the pellet surface and the tube wall, affected the particle surface temperature, and this hotter section has occurred on the upper part of the pellet.

The effectiveness factors were calculated for front and back particles, and less effective particles were found than the WS-1 model:

$\eta_{front\ particle} = 0.06746$ $\eta_{back\ particle} = 0.07560$

Keep in mind that the back particle orientations of WS-1 and WS-4 models were also different. So, these preliminary results showed that, the particle orientation is important for both front and back particles. Therefore, it is worth to continue with WS-2 and WS-3 models to investigate up to what extent the modeling parameters such as the tube wall temperature and the particle effectiveness can be affected.

7.2.2 Wall to wall contact points

As stated in the main body of this document before, we have intentionally kept a gap between the particle to particle, and the particle to tube wall contacts, so as not to face convergence problems due to skewed elements that occur with grid generation on these contacts.

Previously, N = 2.43 tube with 10 spherical particles was modeled with contact points (Logtenberg et al., 1999), and agreement between the empirical correlations was observed in thermal conductivity predictions for high Re flows. In the later work (Nijemeisland and Dixon, 2001), for N = 2 tube with 44 spheres, the spherical particle contact points were modeled with a "near-miss" approach where as a first step, touching particles were placed and then the model was finalized by reducing their diameters 99-99.5% while keeping the same particle central coordinates to allow a gap between them. Based on the experiences of that work, the spherical packing WS model was created with 99.5% reduction.

Recently, the 0.5% overlapping spherical particle geometry was introduced (Guardo et al., 2006) without any meshing detail to prevent the convergence problems.

As a preliminary study, 99.8% reduced and 0.5% overlapping particles were created for spherical packing WS model with GAMBIT 2.2.30, and many skewed cells obtained especially for the overlapping case with UNS tetrahedral elements. Figure 7.3 presents the mid point-view of the models where particles are not colored. The 99.5% reduced particle case is also shown for comparison.

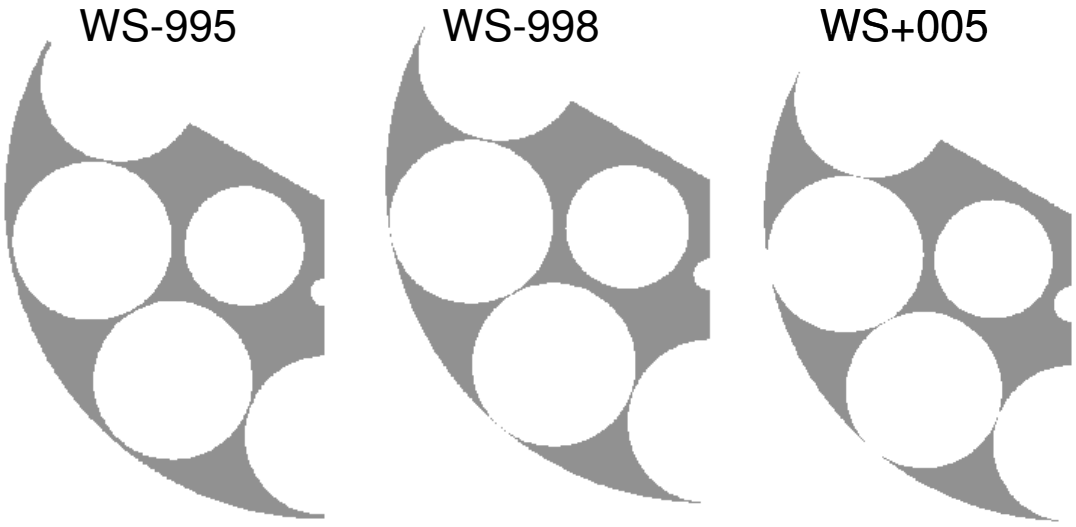

Figure 7.3 The mid-plane views of spherical packing WS models with 99.5% and 99.8% reduced, and 0.05% increased size.

The overall bed voidages of these models are 0.4147 for WS-995, 0.4062 for WS-998, and 0.3915 for WS+005. Based on our previous experiences, the momentum convergence can be achieved with very low URF's for the models with highly skewed cells. Thus, we have obtained the pressure drop values of WS-998 and WS+005 models with the same operating conditions as stated before, and normalized based on WS-995 model value:

$$\Delta P / L_{WS-998} = 1.160 \quad (Pa/m)/(Pa/m) \qquad \Delta P / L_{WS+005} = 1.740 \quad (Pa/m)/(Pa/m)$$

As can be noticed there was a dramatic difference for the overlapping model pressure drop value. Therefore, further investigation would have been performed to include the heat and mass transfer. However, the unreasonable temperature or species values that were calculated and stored for the skewed cells, due to their skewness of course, created a disastrous convergence problem.

We have not gone through these problems in the main body of the text, because our main interest was on the cylindrical packings, and there was not a convergence problem since cylindrical particles were not touching each other or the tube wall.

To solve the touching particle problem a better mesh is necessary, with suitable cell structure, and significant time has to be spent to create the model. Recently FLUENT announced that the version 6.3 has an additional feature that polyhedral cell elements can be used, which may reduce the skewness problem that occurs by tetrahedral cells. The utilization of version 6.3 would be a reasonable starting point to approach the problem, and the latest version of FLUENT became available in our institution couple of months ago.

Once the touching/overlapping particle models are created with spherical and cylindrical packings, the diffusion/reaction modeling can be performed to investigate the near wall gradients for the situation where there will be no gap between the tube wall and the particles.

7.2.3 Catalyst deactivation modeling

One of the important phenomena in catalytic reactions is the catalyst deactivation which occurs on all catalysts either gradually or fast. Among the deactivation processes, carbon formation, or fouling, is the frequently faced problem in many reactions including methane steam reforming and propane dehydrogenation. Fouling is the physically covering of active sites and/or the entire surface of the support, by carbonaceous or inorganic deposits. Severe fouling can lead to pore plugging which cuts off access to active regions and causes loss in activity. Moderate fouling causes a steady but slower

decline in activity that can reach a rather steady and acceptable level for long-term operation (Rase, 1990).

For propane dehydrogenation, carbon formation occurs very fast, and therefore it has been considered with the main reaction all the time. Technically, a carbon formation is another reaction or reactions which can be expressed with separate reaction rates. The following reaction is known as the main carbon formation reaction in the propane dehydrogenation:

$$C_3H_8 \rightarrow 3C + 4H_2 \qquad (7.1)$$

The rate equation for the carbon formation may be expressed as:

$$\frac{dC_C}{dt} = r_C^0 \Phi_C \qquad (7.2)$$

where r_C^0 is the initial coking rate (fresh catalyst), and Φ_C is an activity factor as most frequently expressed:

$$\Phi_C = \exp(-\alpha \cdot C_C) \qquad (7.3)$$

where α is the deactivation parameter which was found to be a function of temperature (Jackson and Stitt, 2004).

To model the deactivation, the catalyst activity must be related to the coke accumulation which may be obtained by integrating the equation (7.2) with a suitable initial coking rate expression. The deactivation model can be coupled to the main reaction model and implemented into the pellet by a user-defined code. By this way, the overall reaction conversion and selectivity, and temperature dependence of the carbon deposition could be investigated in detail regarding the benefits of CFD.

Nomenclature

a_v	pellet surface area per reactor volume	[m^2/m^3]
C	concentration	[$kmol/m^3$]
c_p	fluid heat capacity	[J/kg-K]
d_p	pellet diameter	[m]
d_{pv}	particle diameter equivalent to sphere volume	[m]
d_t	tube diameter	[m]
$D_{A,m}$	effective diffusivity of species A in mixture	[m^2/s]
D_{er}	effective diffusivity	[m^2/s]
D_{md}	molecular diffusivity	[m^2/s]
D_K	Knudsen diffusivity	[m^2/s]
E	energy	[J]
g	gravitational acceleration	[m/s^2]
G	mass flow rate of the fluid	[kg/m^2-s]
h	heat transfer coefficient	[W/m-K]
k_g	mass transfer coefficient	[m/s]
k_i	reaction rate constant of reaction i	[kmol/kg cat-s·kPa^n]
K_A	adsorption coefficient of species A	[kPa^{-1}]
K_j	equilibrium constant of component j	[kPa^n]
L_p	particle length	[m]
M_A	molecular weight of A	[kg/kmol]
N	tube to particle diameter ratio	[-]
P	static pressure	[kPa]
P_j	partial pressure of component j	[kPa]
q_{wall}	wall heat flux	[W/m^2]
Q	heat	[W]

r_c	cut-off ratio	[-]
r_p	particle radius	[m]
r_i	reaction rate (i=1,2,…), MSR	[kmol/kg cat-s]
r_i	reaction rate (i=1,2,…), PDH	[kmol/m^3 -s]
r_t	tube radius	[m]
R	gas constant	8.314 [J/mol-K]
S	arc length	[m]
Sm	source term	[…/m^3]
T	temperature	[K]
u,v,w	velocity components	[m/s]
U	overall heat transfer coefficient	[W/m-K]
U^+	dimensionless velocity, wall function unit	[-]
V_z	axial velocity	[m/s]
V_0	superficial velocity	[m/s]
x, y, z	cartesian coordinates	[-]
X_A	conversion of component A	[-]
y^+	dimensionless distance, wall function unit	[-]
Y_i	mass fraction of i	[-]
Z	height	[m]

Greek symbols

α	under relaxation factor	[-]
α_{ij}	stoichiometric coefficient	[-]
ϵ	bed voidage	[-]
ε	turbulence dissipation	[J/s]
ε_s	porosity of the particle	[-]

κ	turbulent kinetic energy	[J]
η	effectiveness factor	[-]
μ	viscosity	[Pa·s]
μ^t	turbulent viscosity	[Pa·s]
ρ	density	[kg/m^3]
Γ	tortuosity factor	[-]
τ	viscous stress tensor	[N/m^2]
α	under relaxation factor	[-]
ξ	radial coordinate in the catalyst (r/rp)	[-]
ΔH	enthalpy of the reaction	[kJ/mol]
$\Delta P/L$	pressure gradient	[Pa/m]
ΔT_w	temperature drop across the wall	[K]

Dimensionless numbers

Nusselt Number $Nu = \frac{hd_p}{k_f}$

Peclet Number $Pe = \frac{Gc_p d_p}{k_f}$

Prandtl Number $\mathrm{Pr} = \frac{c_p \mu}{k_f}$

Reynolds Number $\mathrm{Re} = \frac{\rho v d_p}{\mu}$

Abbreviations

B-E	Bey and Eigenberger
CFD	Computational Fluid Dynamics
CW	Complete Wall
DPM	Discrete Packing Model
EWT	Enhanced Wall Treatment
FD	Finite Difference
FE	Finite Element
FV	Finite Volume
GHSV	Gas Hourly Space Velocity
GSA	Geometric Surface Area
M-C	Multicomponent
MRI	Magnetic Resonance Imaging
MSR	Methane Steam Reforming
P-C	Pseudo-continuum
PDH	Propane Dehydrogenation
RNG	Renormalization Group
UDMI	User-defined Memory Index
UNS	Unstructured
URF	Under Relaxation Factor
TWT	Tube Wall Temperature
WGSR	Water Gas Shift Reaction
W-T	Winterberg and Tsotsas

References

Avci, A., K., Trimm, D., L., and Ilsen Onsan, Z. (2001), Heterogeneous reactor modeling for simulation of catalytic oxidation and steam reforming of methane. *Chemical Engineering Science*, **56**, 641-649.

Aparicio, L., M., (1997), Transient isotopic studies and microkinetic modeling of methane reforming over nickel catalysts. *Journal of Catalysis*, **165**, 262-274.

Balakotaiah, V., and Dommeti, S. M. S. (1999), Effective models for packed-bed catalytic reactors. *Chemical Engineering Science*, **54**, 1621-1638.

Bauer, R., and Schlunder, E. U. (1978a), Effective radial thermal conductivity of packing in gas flow. Part I. Convective transport coefficient. *International Chemical Engineering*, **18**, 181-188.

Bauer, R., and Schlunder, E. U. (1978b), Effective radial thermal conductivity of packing in gas flow. Part I. Thermal conductivity of packing fraction without gas flow. *International Chemical Engineering*, **18**, 189-204.

Bey, O., and Eigenberger, G. (2001), Gas flow and heat transfer through catalyst filled tubes. *International Journal of Thermal Science*, **40**, 152-164.

Buruno, S. P., Barreto, G. F., and Gonzalez, M. G. (1988), Effect of geometric characteristics of commercial catalysts for steam reforming. *Chemical Engineering Journal*, **39**, 147-156.

Calis, H., P., A., Nijerhuis, J., Paikert, B., C., Dautzenberg, F., M., and van den Bleek, C., M. (2001), CFD modeling and experimental validation of pessure drop and flow profile in a novel structured catalytic reactor packing. *Chemical Engineering Science*, **56**, 1713-1720.

Dalman, M., T., Merkin, J., H., and McGreavy, C. (1986), Fluid flow and heat transfer past two spheres in a cylindrical tube. *Computers & Fluids* **14**, 267-281.

Deans, H., A., and Lapidus, L. (1960), A computational model for predicting and correlating the behavior of fixed-bed reactors: I. Derivation of model for nonreactive systems. *American Institute of Chemical Engineers Journal*, **6**, 656-663.

Derkx, O., R., and Dixon, A., G. (1996), Determination of the fixed bed wall heat transfer coefficient using computational fluid dynamics. *Numerical Heat Transfer Part A*, **29**, 777-794.

Dixon, A., G., and Cresswell, D., L. (1979), Theoretical prediction of effective heat transfer parameters in packed beds. *American Institute of Chemical Engineers Journal*, **25**, 663-676

Dixon, A., G. (1988), Wall and particle shape effects on heat transfer in packed beds. *Chemical Engineering Communication*s **71**, 217-237.

Dixon, A., G., and Nijemeisland, M. (2001), CFD as a design tool for fixed-bed reactors. *Ind. Eng. Chem. Res.*, **40**, 5246-5254.

Dixon, A., G., Nijemeisland, M., and Stitt, E., H. (2003), CFD simulation of reaction and heat transfer near the wall of a fixed bed. *International Journal of Chemical Reactor Engineering*, **1**, A22.

Dixon, A., G., Nijemeisland, M., and Stitt, E., H. (2005), CFD study of heat transfer near and at the wall of a fixed bed reactor tube: effect of wall conduction. *Ind. Eng. Chem. Res.*, **44**, 6342-6353.

Dixon, A., G., Nijemeisland, M., and Stitt, E., H. (2006), Packed tubular reactor modeling and catalyst design using computational fluid dynamics. *Advances in Chemical Engineering*, **31**, 307-389.

Dixon, A., G., Taskin, M., E., Stitt, E., H., and Nijemeisland, M. (2007), 3D CFD simulations of steam reforming with resolved intraparticle reaction and gradients. *Chemical Engineering Science, in press*.

Dometti, S., M.S., Balakotaiah, V., and West, D., H. (1999), Analytical criteria for validity od pseudohomogeheous models for paked-bed catalytic reactors. *Industrial & Engineering Chemistry Research*, **38**, 767-777.

Doraiswamy, L., K., and Sharma, M., M. (1984), *Heterogeneous reactions: analysis, examples and reactor design. Volume 1: Gas-solid and solid-solid reactions*, John Wiley & Sons, New York.

Ergun, S. (1952), Fluid flow through packed columns. *Chemical Engineering Progress*, **48**, 89-94.

Esterl, S., Debus, K., Nirschl, H., Delgado, A. (1998), Three dimensional calculations of the flow through packed beds. *Fluid Dynamics and Process Automation. Eur. Comput. Fluid Dyn. Conf.*, 4th, 692-696.

Fluent (2005), User's Guide version 6.2, Fluent Inc., Lebanon, NH.

Freund, H., Zeiser, T., Huber, F., Klemm, E., Brenner, G., Durst, F., and Emig, G. (2003), Numerical simulations of single phase reacting flows in randomly packed fixed-bed reactors and experimental validation. *Chemical Engineering Science*, **58**, 903-910.

Froment, G., F. (1974) Fixed Bed Catalytic Reactors, Technological and Fundamental Aspects. *Chemie Ingenieur Technik,* **26**, 374.

Froment, G., F. (2000), Production of synthesis gas by steam- and CO_2- reforming of natural gas. *Journal of Molecular Catalysis*, **163**, 147-156.

Froment, G., F., and Bischoff, K., B. (1990), *Chemical Reactor Analysis and Design*, 2nd Edition, Wiley, New York..

Fuller, E., N., Schettler, P., D., and Giddings, J., C. (1966) A new method for prediction of binary pas-phase diffusion coefficients. *Industrial & Engineering Chemistry,* **58**, 19-27.

Gallucci, F., Paturzo, L., and Basile, A. (2004), A simulation study of the steam reforming of methane in a dense tubular membrane reactor. *International Journal of Hydrogen Energy*, **29**, 611-617.

Guardo, A., Coussirat, M., Larrayoz, M., A., Recasens, F., and Egusquiza, E. (2005), Influence of the turbulence model in CFD modeling of wall-to-fluid heat transfer in packed beds. *Chemical Engineering Science*, **60**, 1733-1742.

Guardo, A., Coussirat, M., Recasens, F., Larrayoz, M. A., and Escaler, X. (2006), CFD study on particle-to-fluid heat transfer in fixed bed reactors: Convective heat transfer at low and high pressure. *Chemical Engineering Science*, **61**, 4341-4353.

Guardo, A., Coussirat, M., Recasens, F., Larrayoz, M., A., and Escaler, X. (2007), CFD studies on particle-to-fluid mass and heat transfer in packed bed reactors: Free convection effects in supercritical fluids. *Chemical Engineering Science, in press*.

Gulijk, C., V. (1998), Using computational fluid dynamics to calculate transversal dispersion in a structured packed bed. *Computers & Chemical Engineering*, **22**, 767-770.

Gunjal, P., R., Ranade, V., V., and Chaudhari, R., V. (2005), Computational study of a single-phase flow in packed beds of spheres. *American Institute of Chemical Engineers Journal*, **51**, 365-378.

Hicks, R., E. (1970), Pressure drop in packed beds of spheres. *Ind. Eng. Chem. Fundam.*, **9**, 500-502.

Hoffmann, K., A., and Chiang, S., T. (1993), *Computational Fluid Dynamics for Engineers, Volume II*, 1st Edition, Engineering Education System, Kansas.

Hou, K., Hughes, R. (2001), The kinetics of methane steam reforming over a Ni/α-Al_2O catalyst. *Chemical Engineering Journal*, **82**, 311-328.

Hou, K., Hughes, R. (2002), A comparative simulation analysis of propane dehydrogenation in composite and microporous membrane reactors. *Journal of Chemical Technology and Biotechnology*, **78**, 35-41.

Jackson, S., D. and Stitt, E., H. (2004), Propane dehydrogenation over chromia catalysts: microcatalysis, deactivation, macrokinetics, and reactor modeling. *ChemInform*, **35**, issue 23.

Jarosch, K., El Solh, T., and de Lasa, H., I. (2002), Modeling the catalytic steam reforming of methane: discrimination between kinetic expressions using sequentially designed experiments. *Chemical Engineering Science*, **57**, 3439-3451.

Koning, G., W., Kronberg, A., E., and van Swaajj, W., P., M. (2006), Improved one-dimensional model for a tubular packed bed reactor. *Chemical Engineering Science*, **61**, 3167-3175.

Kuijpers, J., A., M. and van Swaaij, W., P., M. (1998), Computational fluid dynamics applied to chemical reaction engineering. *Advances in Chemical Engineering,* **24**, 227-328

Kvamsal, H., M., Svendsen, H., F., Hertzberg, T., and Olsvik, O. (1999), Dynamic simulation and optimization of a catalytic steam reformer. *Chemical Engineering Science*, **54**, 2697-2706.

Launder, B., E. and Spalding, D., B.(1972), *Lectures in Mathematical Models in Turbulence*. Academic Press, London.

Launder, B., E. and Spalding, D., B. (1974), The numerical computation of turbulent flows. *Computer Methods in Applied Mechanics and Engineering*, **3**, 269-289.

Laguerre, O., Ben Amera, S., Alvarez, G., and Flick, D. (2007) Transient heat transfer by free convection in a packed bed of spheres: Comparison between two modeling approaches and experimental results. *Applied Thermal Engineering*, in press.

Leising, G. (2005), *M. S. Thesis*. Worcester Polytechnic Institute, Worcester, MA.

Lloyd, B. and Boehm, R. (1994), Flow and heat transfer around a linear array of spheres. *Numerical Heat Transfer, Part A*, **26**, 237-252

Levenspiel, O. (1972), *Chemical reaction engineering*. John Wiley & Sons, 2nd ed, New York.

Logtenberg, S., A., and Dixon, A., G. (1998a), Computational fluid dynamics studies of fixed bed heat transfer. *Chemical Engineering and Processing* **37**, 7-21

Logtenberg, S., A. and Dixon, A., G. (1998b), Computational fluid dynamics studies of the effects of temperature-dependent physical properties on fixed-bed heat transfer. *Industrial and Engineering Chemistry Research* **37**, 739-747

Logtenberg, S., A., Nijemeisland, M., and Dixon, A., G. (1999), Computational fluid dynamics simulations of fluid flow and heat transfer at the wall-particle contact points in a fixed bed reactor. *Chemical Engineering Science* **54**, 2433-2439

Machac, A., Henda, R., and Nilsson, B. (2006), Modeling of heat and mass transport in a nonlinear catalytic bed reactor. *Proceedings of the 2006 Nordic COMSOL Conference.*

Magnico, P. (2003), Hydrodynamic and transport properties of packed beds in small tube-to-sphere diameter ratio: Pore scale simulation using an Eulerian and a Langrangian approach. *Chemical Engineering Science*, **58**, 5005-5024.

Mariani, N., J., Keegan, S, D., Martinez, O., M., and Barreto, G., F. (2003), A one-dimensional equivalent model to evaluate overall reaction rates in catalytic pellets. *Trans. Inst. Chem. Eng. Part A*, **81**, 1033.

McGuire, M., and Lapidus, L. (1965), On the stability of a detailed packed bed reactor. *American Institute of Chemical Engineers Journal*, **11**, 85-95.

Mears, D., E. (1971), Diagnostic criteria for hest transport limitations in fixed bed reactors. *Journal of Catalysis*, **20**, 127-131.

Molerus, O. (1977), Druckverlustg leichung für die durch-strömung von kugelschüttungen im laminaren und im übergangs bereich. *Chem. Ing. Techn.*, **49**, 675.

Navier, M. (1827), Mémorie sur les Lois du Mouvement des Fluides. *Mem. De l'Acad. De Sci.* **6**, 389.

Nijemeisland, M., and Dixon, A., G. (2001), Comparison of CFD simulations to experiment for convective heat transfer in a gas-solid fixed bed. *Chemical Engineering Journal,* **82, 1-3**, 231-246

Nijemeisland, M. (2002), *Ph. D. Thesis*. Worcester Polytechnic Institute, Worcester, MA.

Nijemeisland, M., Dixon, A., G., and Stitt, E., H. (2004), Catalyst design by CFD for heat transfer and reaction in steam reforming. *Engineering Science*, **59**, 5185-5191.

Nijemeisland, M., and Dixon, A., G.(2004), CFD study of fluid flow and wall heat transfer in a fixed bed of spheres. *American Institute of Chemical Engineers Journal*, **50**, 906-921.

Ohta, M., Yamamoto, M., and Suzuki, M. (1995), Numerical analysis of a single drop formation process under pressure pulse condition. *Chemical Engineering Science,* **50**, 2923.

Owoyemi, O., Mazzei, L., and Lettieri, P. (2007), CFD modeling of binary-fluidized suspensions and investigation of role of particle-particle drag on mixing and segregation. *American Institute of Chemical Engineers Journal*, **53**, 1924-1940.

Patankar, S., V. (1980), *Numerical Heat Transfer and Fluid Flow*, Hemisphere, Washington, D.C.

Papageorgiou, J., N., and Froment, G., F. (1995), Simulation models accounting for radial voidage profiles in fixed-bed reactors. *Chemical Engineering Science*, **50**, 3043-3056.

Pedernera, M., N., Pina, J., Borio, D., O., and Bucala, V. (2003), Use of a heterogeneous two-dimensional model to improve the primary steam reformer performance. *Chemical Engineering Journal*, **94**, 29-40.

Petre, C., F., Larachi, F., Iliuta, I., and Grandjean, B., P., A. (2003), Pressure drop through structured packings: Breakdown into the contributing mechanisms by CFD modeling. *Chemical Engineering Science*, **58**, 163-177.

Persons, I., M., and Porter K., E. (1992), Gas flow patterns in packed beds: A computational fluid dynamics model for wholly packed domains. *Gas Separation & Purification*, **6**, 221-227.

Ranade, V. (2002), *Computational Flow Modeling for Chemical Reactor Engineering*, Academic Press, New York.

Rase, H., F. (1990), *Fixed-bed reactor design and diagnostics*. Butterworths Publishers, Stoneham, MA.

Reichelt, W. (1972), Zur berechnung des druckverlustes einphasig durchströmter kugel- und zylinderschüttungen. *Chem. Ing. Techn*., **44**, 1068-1071.

Romkes, S., J., P., Dautzenberg, F., M., van den Bleek, C., M., and Calis, H., P., A. (2003), CFD Modeling and experimental validation of particle-to-fluid mass and heat transfer in a packed bed at very low channel to particle diameter ratio. *Chemical Engineering Journal*, **96**, 3-13.

Salmi, T., and Warna, J. (1991), Modeling of catalytic packed-bed reactors-comparison of different diffusion models. *Computers & Chemical Engineering*, **15**, 715-727.

Sie, S. T., Krishna, R. (1998), Process development and scale-up:II. Catalyst design strategy. *Reviews in Chemical Engineering*, **14**, 159.

Specchia, V., Balgi, G., and Sicardi, S. (1980), Heat transfer in packed bed reactors with one phase flow. *Chemical Engineering Communications*, **4**, 361-380.

Stewart, W., E. (1965), Transport phenomena in fixed-bed reactors. *Chemical Engineering Progress Symposium Series*, **61**, 61.

Stewart, W., E., Marr, D., F., Nam, T., T., and Gola-Galimidi, A., M. (1991), Transport modeling of packed-tube reactors-1. Framework for a data-based approach. *Chemical Engineering Science*, **46**, 2905-2911.

Stitt, E., H., Jackson, S., D., and King, F. (1999), Kinetic based deactivation modeling of an isothermal propane dehydrogenation reactor. *Studies in Surface Science and Catalysis*, **122**, 291-298.

Stitt, E., H., Jackson, S., D., Shipley, D., G. and King, F. (2001), Modeling propane dehydrogenation in a rotating monolith reactor. *Catalysis Today*, **69**, 217-226.

Stitt, E., H. (2005), *Reactor technology for syngas and hydrogen*. In Sustainable strategies for the upgrading of natural gas: fundamentals, challenges and opportunities, Derouane, E., Parmon, V., Lemos, F. and Ramoa-Ribiero, F. (eds.), NATO Science Series, Kluwer Press, **191**, 185.

Stokes, G., G. (1845), On the theories of internal friction of fluids in motion. *Transactions of the Cambridge Philosophical Society.* **8**, 287.

Tobis, J. (2000), Influence of bed geometry on its frictional resistance under turbulent flow conditions. *Chemical Engineering Science*, **55**, 5359-5366.

Tobis, J. (2002), Modeling of the pressure drop in the packing of complex geometry. *Industrial & Engineering Chemistry Research*, **41**, 2552-2559.

Tsotsas, E., and Schlunder, E., U. (1988), Some remarks on channeling and radial dispersion in packed beds, *Chemical Engineering Science*, **43**, 1200-1203.

Winterberg, M., and Tsotsas, E. (2000), Correlations for effective heat transport coefficients in beds packed with cylindrical particles. *Chemical Engineering Science*, **55**, 5937-5943.

van Sint Annaland, M., Scholts, H., A., R., Kuipers, J. A., M., and van Swaaij, W., P., M. (2002), A novel reverse flow reactor coupling endothermic and exothermic reactions. Part-II:Sequential reactor configuration for reversible endothermic reactions. *Chemical Engineering Science*, **57**, 855-872.

Vortmeyer, D., and Schuster, J. (1983), Evaluation of steady flow profiles in rectangular and circular packed beds by a variational method. *Chemical Engineering Science*, **38**, 1691-1699.

Xu, J., and Froment, G., F. (1989a), Methane steam reforming, methanation and water-gas shift: I. Intrinsic kinetics. *American Institute of Chemical Engineers Journal*, **35**, 88-96.

Xu, J., and Froment, G., F. (1989b), Methane steam reforming, II. Diffusional limitations and reactor simulation. *American Institute of Chemical Engineers Journal*, **35**, 97-103.

Yakhot, V., and Orszag, S.A.(1986), Renormalizarion group analysis. I. Basic theory. *Journal of Scientific Computing*, **1**, 3-51.

Zeiser, T., Lammers, P., Klemm, E., Li, Y., W., Bernsdorf, J., and Brenner, G. (2001), CFD-Calculation of flow, dispersion and reaction in a catalyst filled tube by the Lattice Boltzmann method. *Chemical Engineering Science*, **56**, 1697-1704.

Zeiser, T., Steven, M., Freund, H., Lammers, P., Brenner, G., Durst, F., and Bernsdorf, J. (2002), Analysis of the flow field and pressure drop in fixed-bed reactors with the help of Lattice Boltzmann Simulation. *Phil. Trans. R. Soc. Lond. A*, **360**, 507-520.

Appendices

Appendix 1: Particle placements of WS model

Table A.1 Placement of the particles in WS models

Particle	Placement steps		
1	R	+45	+x
	T	-1.45	+x
	R	+40	+z
2	R	-45	+x
	T	-1.45	+x
	T	+1	+z
	R	+20	+z
3	**C 1**		
	T	+2	+z
4	R	+5	+x
	T	-1.48	+x
	R	-9	+z
5	**C 4**		
	T	+2	+z
6	R	+90	+y
	T	-1.42	+y
	R	+5	+z
7	**C 6**		
	T	+2	+z
8	R	+90	+x
	T	-1.42	+y
	T	+1	+z
	R	-17.5	+z
9	R	+45	+x
	T	-1.45	+x
	T	-1	+z
	R	-40	+z
10	R	-45	+y
	T	-0.25	+x
11	**C 10**		
	T	+2	+z
12	R	+90	+x
	T	+1	+z
	T	-0.35	+y
	T	+0.2	+x

R=rotate, T=translate, C=copy

Rotations are in degrees, translations in inches, based on a 1 inch diameter, 1 inch height particle.

Appendix 2: Particle placements of CW model

Table A.2 Placement of the particles in the CW model in addition to 11 WS particles.

Particle	Placement steps		
12'	**C 12**		
	T	+0.19	+y
13	**C 2**		
	R	+105	+z
	T	-0.005	+z
14	R	+29.8	+x
	T	+1.45	+x
	R	-31	+z
15	**C 14**		
	T	+2	+z
16	**C 8**		
	R	+106.8	+z
	R	+10	+y
	T	-0.3	+x
	T	+0.26	+z
	T	-0.05	+y
17	**C 16**		
	R	+10	+z
	T	-0.09	+x
	T	+0.21	+y
	T	-1.01	+z
18	**C 17**		
	T	+2	+z
19	R	+30	+x
	T	+1.45	+x
	R	+44.7	+z
	T	+1.02	+z
20	**C 8**		
	R	+199	+z
	T	+0.03	+x
	T	-0.25	+y
	T	+0.05	+z
	R	+5	+x
21	R	-44.999	+x
	T	-1.45	+x
	R	-58	+z
22	**C 21**		
	T	+2	+z
23	R	+99.6	+z
	T	+0.055	+z
	R	+2	+x
24	**C 23**		
	T	+2	+z

Appendix 3: User-defined codes

(a) for the verification of the active region selection

Particle 2 of 4-hole cylinders model with 3% activity, as an example:

```
#include "udf.h"

DEFINE_ON_DEMAND(verif_2)
{
 Domain *d;
 int ID = 10;
 real cyl_rad, midpellet_dist, p_dist, axis_dist;
 real rc, xc, yc, zc, de, a, b, cc, den, xt, yt, zt, x[ND_ND], delta, rh, rhc;
 real xc_h1, yc_h1, zc_h1, xc_h2, yc_h2, zc_h2, xc_h3, yc_h3, zc_h3;
 real xt_h1, yt_h1, zt_h1, xt_h2, yt_h2, zt_h2, xt_h3, yt_h3, zt_h3;
 real a_h1, b_h1, c_h1, a_h2, b_h2, c_h2, a_h3, b_h3, c_h3;
 real p_dist_h1, p_dist_h2, p_dist_h3, axis_dist_h1, axis_dist_h2, axis_dist_h3;
 real xt_h4, yt_h4, zt_h4, xc_h4, yc_h4, zc_h4, a_h4, b_h4, c_h4, p_dist_h4, axis_dist_h4;

 Thread *t;
 cell_t c;

 d = Get_Domain(1);
 t = Lookup_Thread(d, ID);

 begin_c_loop(c,t)

  {
   C_CENTROID(x,c,t);

   xc = -1.36*0.0254;
   yc = -0.496*0.0254;
   zc = 1.04*0.0254;

   xt = -1.484*0.0254;
   yt = -0.163*0.0254;
   zt = 1.394*0.0254;

    a = xt-xc;
    b = yt-yc;
    cc = zt-zc;

    xc_h1 = -1.118*0.0254;
    yc_h1 = -0.407*0.0254;
    zc_h1 = 1.04*0.0254;

    xt_h1 = -1.239*0.0254;
```

```
yt_h1 = -0.075*0.0254;
zt_h1 = 1.394*0.0254;

a_h1 = xt_h1-xc_h1;
b_h1 = yt_h1-yc_h1;
c_h1 = zt_h1-zc_h1;

xc_h2 = -1.425*0.0254;
yc_h2 = -0.323*0.0254;
zc_h2 = 0.856*0.0254;

xt_h2 = -1.546*0.0254;
yt_h2 = 0.009*0.0254;
zt_h2 = 1.21*0.0254;

a_h2 = xt_h2-xc_h2;
b_h2 = yt_h2-yc_h2;
c_h2 = zt_h2-zc_h2;

xc_h3 = -1.607*0.0254;
yc_h3 = -0.585*0.0254;
zc_h3 = 1.04*0.0254;

xt_h3 = -1.728*0.0254;
yt_h3 = -0.253*0.0254;
zt_h3 = 1.394*0.0254;

a_h3 = xt_h3-xc_h3;
b_h3 = yt_h3-yc_h3;
c_h3 = zt_h3-zc_h3;

xc_h4 = -1.3*0.0254;
yc_h4 = -0.669*0.0254;
zc_h4 = 1.224*0.0254;

xt_h4 = -1.421*0.0254;
yt_h4 = -0.336*0.0254;
zt_h4 = -1.497*0.0254;

a_h4 = xt_h4-xc_h4;
b_h4 = yt_h4-yc_h4;
c_h4 = zt_h4-zc_h4;

cyl_rad = 0.5*0.0254;
rc = cut*cyl_rad;
rh = 0.1434*0.0254;

delta = (1-cut)*cyl_rad;
rhc = rh+delta;

den = a*a+b*b+cc*cc;
```

```
        de = -a*xc-b*yc-cc*zc;
        midpellet_dist = fabs((a*x[0]+b*x[1]+cc*x[2]+de)/sqrt(den));

        p_dist = sqrt((x[0]-xc)*(x[0]-xc)+(x[1]-yc)*(x[1]-yc)+(x[2]-zc)*(x[2]-zc));
        axis_dist = sqrt((p_dist*p_dist)-(midpellet_dist*midpellet_dist));

        p_dist_h1 = sqrt((x[0]-xc_h1)*(x[0]-xc_h1)+(x[1]-yc_h1)*(x[1]-yc_h1)+(x[2]-zc_h1)*(x[2]-
zc_h1));
        axis_dist_h1 = sqrt((p_dist_h1*p_dist_h1)-(midpellet_dist*midpellet_dist));

        p_dist_h2 = sqrt((x[0]-xc_h2)*(x[0]-xc_h2)+(x[1]-yc_h2)*(x[1]-yc_h2)+(x[2]-zc_h2)*(x[2]-
zc_h2));
        axis_dist_h2 = sqrt((p_dist_h2*p_dist_h2)-(midpellet_dist*midpellet_dist));

        p_dist_h3 = sqrt((x[0]-xc_h3)*(x[0]-xc_h3)+(x[1]-yc_h3)*(x[1]-yc_h3)+(x[2]-zc_h3)*(x[2]-
zc_h3));
        axis_dist_h3 = sqrt((p_dist_h3*p_dist_h3)-(midpellet_dist*midpellet_dist));

        p_dist_h4 = sqrt((x[0]-xc_h4)*(x[0]-xc_h4)+(x[1]-yc_h4)*(x[1]-yc_h4)+(x[2]-zc_h4)*(x[2]-
zc_h4));
        axis_dist_h4 = sqrt((p_dist_h4*p_dist_h4)-(midpellet_dist*midpellet_dist));

        if (midpellet_dist < rc && axis_dist < rc && axis_dist_h1 > rhc && axis_dist_h2 > rhc &&
axis_dist_h3 > rhc && axis_dist_h4 > rhc)
            C_UDMI(c,t,0)=0.0;
        else
            C_UDMI(c,t,0)=1.0;
        }
      end_c_loop(c,t)

    }
```

(b) for the application of reaction heat effects approximation

Particle 2 of 4-hole cylinders model, as an example:

```
#include "udf.h"

#define rgas 0.0083144
#define rhos 1947.0
#define delhco -140.0
#define delhh -93.4
#define delhh2o 15.9
#define E1 209.2
#define E2 15.4
#define E3 109.4
#define A1 5.922e8
#define A2 6.028e-4
#define A3 1.093e3
#define delHr1 -206100000.0
#define delHr2 41150000.0
#define delHr3 -165000000.0
#define AKco 5.127e-13
#define AKh 5.68e-10
#define AKh2o 9.251
#define Pco 1.0795
#define Ph2 10.795
#define Ph2o 1462.7225
#define Pch4 516.4326
#define Pco2 167.5383
#define cut 0.97

DEFINE_SOURCE(q_tdep_2, cell, thread, dS, eqn)
{
  real source;
  real kco, kh, kh2o, DEN, k1, Kp1, r1, k2, Kp2, r2, k3, Kp3, r3;
  real Pkin1, Prev1, Pkin2, Prev2, Pkin3, Prev3;
  real dk1dt, dKp1dt, dk2dt, dKp2dt, dk3dt, dKp3dt, dDENdt, dr1dt, dr2dt, dr3dt;
  real cell_temp, x[ND_ND], cyl_rad, midpellet_dist, p_dist, axis_dist;
  real rc, xc, yc, zc, d, a, b, c, den, xt, yt, zt;
  real delta, rh, rhc;
  real xc_h1, yc_h1, zc_h1, xc_h2, yc_h2, zc_h2, xc_h3, yc_h3, zc_h3;
  real xt_h1, yt_h1, zt_h1, xt_h2, yt_h2, zt_h2, xt_h3, yt_h3, zt_h3;
  real a_h1, b_h1, c_h1, a_h2, b_h2, c_h2, a_h3, b_h3, c_h3;
  real p_dist_h1, p_dist_h2, p_dist_h3, axis_dist_h1, axis_dist_h2, axis_dist_h3;
  real xt_h4, yt_h4, zt_h4, xc_h4, yc_h4, zc_h4, a_h4, b_h4, c_h4, p_dist_h4, axis_dist_h4;

  cell_temp = C_T(cell, thread);

  C_CENTROID(x,cell,thread);

  xc = -1.36*0.0254;
```

```
yc = -0.496*0.0254;
zc = 1.04*0.0254;

xt = -1.484*0.0254;
yt = -0.163*0.0254;
zt = 1.394*0.0254;

a = xt-xc;
b = yt-yc;
c = zt-zc;

   xc_h1 = -1.118*0.0254;
   yc_h1 = -0.407*0.0254;
   zc_h1 = 1.04*0.0254;

   xt_h1 = -1.239*0.0254;
   yt_h1 = -0.075*0.0254;
   zt_h1 = 1.394*0.0254;

   a_h1 = xt_h1-xc_h1;
   b_h1 = yt_h1-yc_h1;
   c_h1 = zt_h1-zc_h1;

   xc_h2 = -1.425*0.0254;
   yc_h2 = -0.323*0.0254;
   zc_h2 = 0.856*0.0254;

   xt_h2 = -1.546*0.0254;
   yt_h2 = 0.009*0.0254;
   zt_h2 = 1.21*0.0254;

   a_h2 = xt_h2-xc_h2;
   b_h2 = yt_h2-yc_h2;
   c_h2 = zt_h2-zc_h2;

   xc_h3 = -1.607*0.0254;
   yc_h3 = -0.585*0.0254;
   zc_h3 = 1.04*0.0254;

   xt_h3 = -1.728*0.0254;
   yt_h3 = -0.253*0.0254;
   zt_h3 = 1.394*0.0254;

   a_h3 = xt_h3-xc_h3;
   b_h3 = yt_h3-yc_h3;
   c_h3 = zt_h3-zc_h3;

   xc_h4 = -1.3*0.0254;
   yc_h4 = -0.669*0.0254;
   zc_h4 = 1.224*0.0254;
```

```
        xt_h4 = -1.421*0.0254;
        yt_h4 = -0.336*0.0254;
        zt_h4 = -1.477*0.0254;

        a_h4 = xt_h4-xc_h4;
        b_h4 = yt_h4-yc_h4;
        c_h4 = zt_h4-zc_h4;

    cyl_rad = 0.5*0.0254;
    rc = cut*cyl_rad;
    rh = 0.1434*0.0254;

    delta = (1-cut)*cyl_rad;
    rhc = rh+delta;

    den = a*a+b*b+c*c;
    d = -a*xc-b*yc-c*zc;
    midpellet_dist = fabs((a*x[0]+b*x[1]+c*x[2]+d)/sqrt(den));

    p_dist = sqrt((x[0]-xc)*(x[0]-xc)+(x[1]-yc)*(x[1]-yc)+(x[2]-zc)*(x[2]-zc));
    axis_dist = sqrt((p_dist*p_dist)-(midpellet_dist*midpellet_dist));

        p_dist_h1 = sqrt((x[0]-xc_h1)*(x[0]-xc_h1)+(x[1]-yc_h1)*(x[1]-yc_h1)+(x[2]-zc_h1)*(x[2]-
zc_h1));
        axis_dist_h1 = sqrt((p_dist_h1*p_dist_h1)-(midpellet_dist*midpellet_dist));

        p_dist_h2 = sqrt((x[0]-xc_h2)*(x[0]-xc_h2)+(x[1]-yc_h2)*(x[1]-yc_h2)+(x[2]-zc_h2)*(x[2]-
zc_h2));
        axis_dist_h2 = sqrt((p_dist_h2*p_dist_h2)-(midpellet_dist*midpellet_dist));

        p_dist_h3 = sqrt((x[0]-xc_h3)*(x[0]-xc_h3)+(x[1]-yc_h3)*(x[1]-yc_h3)+(x[2]-zc_h3)*(x[2]-
zc_h3));
        axis_dist_h3 = sqrt((p_dist_h3*p_dist_h3)-(midpellet_dist*midpellet_dist));

        p_dist_h4 = sqrt((x[0]-xc_h4)*(x[0]-xc_h4)+(x[1]-yc_h4)*(x[1]-yc_h4)+(x[2]-zc_h4)*(x[2]-
zc_h4));
        axis_dist_h4 = sqrt((p_dist_h4*p_dist_h4)-(midpellet_dist*midpellet_dist));


    if (cell_temp <= 550)
        source = dS[eqn] = 0.0;
    else if (midpellet_dist < rc && axis_dist < rc && axis_dist_h1 > rhc && axis_dist_h2 > rhc &&
axis_dist_h3 > rhc && axis_dist_h4 > rhc)
        source = dS[eqn] = 0.0;
    else
      {
        Pkin1 = Pch4*pow(Ph2o,0.5)/pow(Ph2,1.25);
        Prev1 = Pco*pow(Ph2,3.)/Pch4/Ph2o;
        Pkin2 = Pco*pow(Ph2o,0.5)/pow(Ph2,0.5);
        Prev2 = Pco2*Ph2/Pco/Ph2o;
        Pkin3 = Pch4*Ph2o/pow(Ph2,1.75);
```

```
    Prev3 = Pco2*pow(Ph2,4.)/Pch4/pow(Ph2o,2.);

    kco = AKco*exp(-delhco/(rgas*cell_temp));
    kh = AKh*exp(-delhh/(rgas*cell_temp));
    kh2o = AKh2o*exp(-delhh2o/(rgas*cell_temp));
    DEN = 1+Pco*kco+pow(Ph2,0.5)*kh+Ph2o/Ph2*kh2o;
    Kp1 = 1.198e17*exp(-26830/(cell_temp));
    Kp2 = 1.767e-2*exp(4400/(cell_temp));
    Kp3 = 2.117e15*exp(-22430/(cell_temp));

    k1 = A1*exp(-E1/(rgas*cell_temp));
    r1 = k1*Pkin1*(1-Prev1/Kp1)/pow(DEN,2.);

    k2 = A2*exp(-E2/(rgas*cell_temp));
    r2 = k2*Pkin2*(1-Prev2/Kp2)/pow(DEN,2.);

    k3 = A3*exp(-E3/(rgas*cell_temp));
    r3 = k3*Pkin3*(1-Prev3/Kp3)/pow(DEN,2.);

    source = rhos*(delHr1*r1+delHr2*r2+delHr3*r3);

    dDENdt = Pco*kco*delhco/rgas/cell_temp/cell_temp
          +pow(Ph2,0.5)*kh*delhh/rgas/cell_temp/cell_temp
          +Ph2o/Ph2*kh2o*delhh2o/rgas/cell_temp/cell_temp;

    dk1dt = k1*E1/rgas/cell_temp/cell_temp;
    dk2dt = k2*E2/rgas/cell_temp/cell_temp;
    dk3dt = k3*E3/rgas/cell_temp/cell_temp;

    dKp1dt = Kp1*26830/cell_temp/cell_temp;
    dKp2dt = Kp2*(-4400)/cell_temp/cell_temp;
    dKp3dt = Kp3*22430/cell_temp/cell_temp;

    dr1dt = dk1dt*Pkin1*(1-Prev1/Kp1)/pow(DEN,2.)
          +k1*Pkin1*(Prev1/Kp1/Kp1)*dKp1dt/pow(DEN,2.)
          -2*k1*Pkin1*(1-Prev1/Kp1)/pow(DEN,3.)*dDENdt;

    dr2dt = dk2dt*Pkin2*(1-Prev2/Kp2)/pow(DEN,2.)
          +k2*Pkin2*(Prev2/Kp2/Kp2)*dKp2dt/pow(DEN,2.)
          -2*k2*Pkin2*(1-Prev2/Kp2)/pow(DEN,3.)*dDENdt;

    dr3dt = dk3dt*Pkin3*(1-Prev3/Kp3)/pow(DEN,2.)
          +k3*Pkin3*(Prev3/Kp3/Kp3)*dKp3dt/pow(DEN,2.)
          -2*k3*Pkin3*(1-Prev3/Kp3)/pow(DEN,3.)*dDENdt;
    dS[eqn] = rhos*(delHr1*dr1dt+delHr2*dr2dt+delHr3*dr3dt);
   }
  return source;
}
```

(c) for the diffusion/reaction application of MSR

```
#include "udf.h"

#define rgas 0.0083144
#define rhos 1947.0
#define delhco -140.0
#define delhh -93.4
#define delhh2o 15.9
#define E1 209.2
#define E2 15.4
#define E3 109.4
#define A1 5.922e8
#define A2 6.028e-4
#define A3 1.093e3
#define delHr1 -206100000.0
#define delHr2 41150000.0
#define delHr3 -165000000.0
#define AKco 5.127e-13
#define AKh 5.68e-10
#define AKh2o 9.251
#define Mco 28.0
#define Mh2 2.0
#define Mh2o 18.0
#define Mch4 16.0
#define Mco2 44.0
#define Totpress 2159000.0


DEFINE_SOURCE(spe_ch4, cell, thread, dS, eqn)
{
  real source;
  real kco, kh, kh2o, DEN, k1, Kp1, r1, k2, Kp2, r2, k3, Kp3, r3;
  real Pkin1, Prev1, Pkin2, Prev2, Pkin3, Prev3;
  real dPch4dych4, dr1dPch4, dr2dPch4, dr3dPch4;
  real cell_temp, cell_press;
  real ych4, yh2, yco, yco2, yh2o, Ysum, Pch4, Ph2, Pco, Pco2, Ph2o;
  real alph1, alph2, alph3;

  cell_temp = C_T(cell, thread);
  cell_press = (Totpress+C_P(cell, thread))/1000.0;

  ych4 = C_YI(cell, thread, 0);
  yh2 = C_YI(cell, thread, 1);
  yco = C_YI(cell, thread, 2);
  yco2 = C_YI(cell, thread, 3);
  yh2o = 1.0-ych4-yh2-yco-yco2;
  Ysum = ych4/Mch4+yco/Mco+yco2/Mco2+yh2/Mh2+yh2o/Mh2o;
  Pch4 = cell_press*ych4/Mch4/Ysum;
  Ph2 = cell_press*yh2/Mh2/Ysum;
  Pco = cell_press*yco/Mco/Ysum;
```

```
Pco2 = cell_press*yco2/Mco2/Ysum;
Ph2o = cell_press*yh2o/Mh2o/Ysum;

alph1 = -1.0;
alph2 = 0.0;
alph3 = -1.0;

if (cell_temp <= 550)
   source = dS[eqn] = 0.0;
else
  {
   Pkin1 = Pch4*pow(Ph2o,0.5)/pow(Ph2,1.25);
   Prev1 = Pco*pow(Ph2,3.)/Pch4/Ph2o;
   Pkin2 = Pco*pow(Ph2o,0.5)/pow(Ph2,0.5);
   Prev2 = Pco2*Ph2/Pco/Ph2o;
   Pkin3 = Pch4*Ph2o/pow(Ph2,1.75);
   Prev3 = Pco2*pow(Ph2,4.)/Pch4/pow(Ph2o,2.);

   kco = AKco*exp(-delhco/(rgas*cell_temp));
   kh = AKh*exp(-delhh/(rgas*cell_temp));
   kh2o = AKh2o*exp(-delhh2o/(rgas*cell_temp));

   DEN = 1+Pco*kco+pow(Ph2,0.5)*kh+Ph2o/Ph2*kh2o;

   Kp1 = 1.198e17*exp(-26830/(cell_temp));
   Kp2 = 1.767e-2*exp(4400/(cell_temp));
   Kp3 = 2.117e15*exp(-22430/(cell_temp));

   k1 = A1*exp(-E1/(rgas*cell_temp));
   r1 = k1*Pkin1*(1-Prev1/Kp1)/pow(DEN,2.);

   k2 = A2*exp(-E2/(rgas*cell_temp));
   r2 = k2*Pkin2*(1-Prev2/Kp2)/pow(DEN,2.);

   k3 = A3*exp(-E3/(rgas*cell_temp));
   r3 = k3*Pkin3*(1-Prev3/Kp3)/pow(DEN,2.);

   source = rhos*(alph1*r1+alph2*r2+alph3*r3)*Mch4;

   dPch4dych4 = cell_press*(Ysum/Mch4-(ych4/Mch4)/Mch4)/Ysum/Ysum;

   dr1dPch4 = k1*pow(Ph2o,0.5)/pow(Ph2,1.25)*(1-Prev1/Kp1)/pow(DEN,2.)
        +k1*Pkin1*(Pco*pow(Ph2,3.)/Kp1/pow(Pch4,2.)/Ph2o)/pow(DEN,2.);

   dr2dPch4 = 0;

   dr3dPch4 = k3*Ph2o/pow(Ph2,1.75)*(1-Prev3/Kp3)/pow(DEN,2.)
        +k3*Pkin3*(Pco2*pow(Ph2,4.)/Kp3/pow(Pch4,2.)/pow(Ph2o,2.))/pow(DEN,2.);

   dS[eqn] = rhos*Mch4*(alph1*dr1dPch4+alph2*dr2dPch4+alph3*dr3dPch4)*dPch4dych4;
  }
```

```
  return source;
}

DEFINE_SOURCE(spe_h2, cell, thread, dS, eqn)
{
  real source;
  real kco, kh, kh2o, DEN, k1, Kp1, r1, k2, Kp2, r2, k3, Kp3, r3;
  real Pkin1, Prev1, Pkin2, Prev2, Pkin3, Prev3;
  real dPh2dyh2, dDENdPh2, dr1dPh2, dr2dPh2, dr3dPh2;
  real cell_temp, cell_press;
  real ych4, yh2, yco, yco2, yh2o, Ysum, Pch4, Ph2, Pco, Pco2, Ph2o;
  real alph1, alph2, alph3;

  cell_temp = C_T(cell, thread);
  cell_press = (Totpress+C_P(cell, thread))/1000.0;
  ych4 = C_YI(cell, thread, 0);
  yh2 = C_YI(cell, thread, 1);
  yco = C_YI(cell, thread, 2);
  yco2 = C_YI(cell, thread, 3);
  yh2o = 1.0-ych4-yh2-yco-yco2;
  Ysum = ych4/Mch4+yco/Mco+yco2/Mco2+yh2/Mh2+yh2o/Mh2o;
  Pch4 = cell_press*ych4/Mch4/Ysum;
  Ph2 = cell_press*yh2/Mh2/Ysum;
  Pco = cell_press*yco/Mco/Ysum;
  Pco2 = cell_press*yco2/Mco2/Ysum;
  Ph2o = cell_press*yh2o/Mh2o/Ysum;

  alph1 = 3.0;
  alph2 = 1.0;
  alph3 = 4.0;

  if (cell_temp <= 550)
     source = dS[eqn] = 0.0;
  else
    {
     Pkin1 = Pch4*pow(Ph2o,0.5)/pow(Ph2,1.25);
     Prev1 = Pco*pow(Ph2,3.)/Pch4/Ph2o;
     Pkin2 = Pco*pow(Ph2o,0.5)/pow(Ph2,0.5);
     Prev2 = Pco2*Ph2/Pco/Ph2o;
     Pkin3 = Pch4*Ph2o/pow(Ph2,1.75);
     Prev3 = Pco2*pow(Ph2,4.)/Pch4/pow(Ph2o,2.);

     kco = AKco*exp(-delhco/(rgas*cell_temp));
     kh = AKh*exp(-delhh/(rgas*cell_temp));
     kh2o = AKh2o*exp(-delhh2o/(rgas*cell_temp));

     DEN = 1+Pco*kco+pow(Ph2,0.5)*kh+Ph2o/Ph2*kh2o;

     Kp1 = 1.198e17*exp(-26830/(cell_temp));
     Kp2 = 1.767e-2*exp(4400/(cell_temp));
```

```
    Kp3 = 2.117e15*exp(-22430/(cell_temp));

    k1 = A1*exp(-E1/(rgas*cell_temp));
    r1 = k1*Pkin1*(1-Prev1/Kp1)/pow(DEN,2.);

    k2 = A2*exp(-E2/(rgas*cell_temp));
    r2 = k2*Pkin2*(1-Prev2/Kp2)/pow(DEN,2.);

    k3 = A3*exp(-E3/(rgas*cell_temp));
    r3 = k3*Pkin3*(1-Prev3/Kp3)/pow(DEN,2.);

    source = rhos*(alph1*r1+alph2*r2+alph3*r3)*Mh2;

    dPh2dyh2 = cell_press*(Ysum/Mh2-(yh2/Mh2)/Mh2)/Ysum/Ysum;

    dDENdPh2 = 0.5*kh/pow(Ph2,0.5)-kh2o*Ph2o/pow(Ph2,2.);

    dr1dPh2 = k1*(-1.25*Pch4*pow(Ph2o,0.5)/pow(Ph2,2.25))*(1-Prev1/Kp1)/pow(DEN,2.)
        +k1*Pkin1*(-3.0*Pco*pow(Ph2,3.)/Kp1/Pch4/Ph2o)/pow(DEN,2.)
        -2.0*k1*Pkin1*(1-Prev1/Kp1)/pow(DEN,3.)*dDENdPh2;

    dr2dPh2 = k2*(-0.25*Pco*pow(Ph2o,0.5)/pow(Ph2,1.5))*(1-Prev2/Kp2)/pow(DEN,2.)
        +k2*Pkin2*(-1.0*Pco2)/Kp2/Pco/Ph2o/pow(DEN,2.)
        -2.0*k2*Pkin2*(1-Prev2/Kp2)/pow(DEN,3.)*dDENdPh2;

    dr3dPh2 = k3*(-1.75*Pch4*Ph2o)/pow(Ph2,2.75)*(1-Prev3/Kp3)/pow(DEN,2.)
        +k3*Pkin3*(-4.0*Pco2*pow(Ph2,3.))/Kp3/Pch4/pow(Ph2o,2.)/pow(DEN,2.)
        -2.0*k3*Pkin3*(1-Prev3/Kp3)/pow(DEN,3.)*dDENdPh2;

    dS[eqn] = rhos*Mh2*(alph1*dr1dPh2+alph2*dr2dPh2+alph3*dr3dPh2)*dPh2dyh2;
   }

  return source;
}

DEFINE_SOURCE(spe_co, cell, thread, dS, eqn)
{
  real source;
  real kco, kh, kh2o, DEN, k1, Kp1, r1, k2, Kp2, r2, k3, Kp3, r3;
  real Pkin1, Prev1, Pkin2, Prev2, Pkin3, Prev3;
  real dPcodyco, dDENdPco, dr1dPco, dr2dPco, dr3dPco;
  real cell_temp, cell_press;
  real ych4, yh2, yco, yco2, yh2o, Ysum, Pch4, Ph2, Pco, Pco2, Ph2o;
  real alph1, alph2, alph3;

  cell_temp = C_T(cell, thread);
  cell_press = (Totpress+C_P(cell, thread))/1000.0;
  ych4 = C_YI(cell, thread, 0);
  yh2 = C_YI(cell, thread, 1);
  yco = C_YI(cell, thread, 2);
  yco2 = C_YI(cell, thread, 3);
```

```
yh2o = 1.0-ych4-yh2-yco-yco2;
Ysum = ych4/Mch4+yco/Mco+yco2/Mco2+yh2/Mh2+yh2o/Mh2o;
Pch4 = cell_press*ych4/Mch4/Ysum;
Ph2 = cell_press*yh2/Mh2/Ysum;
Pco = cell_press*yco/Mco/Ysum;
Pco2 = cell_press*yco2/Mco2/Ysum;
Ph2o = cell_press*yh2o/Mh2o/Ysum;

alph1 = 1.0;
alph2 = -1.0;
alph3 = 0.0;

if (cell_temp <= 550)
   source = dS[eqn] = 0.0;
else
  {
   Pkin1 = Pch4*pow(Ph2o,0.5)/pow(Ph2,1.25);
   Prev1 = Pco*pow(Ph2,3.)/Pch4/Ph2o;
   Pkin2 = Pco*pow(Ph2o,0.5)/pow(Ph2,0.5);
   Prev2 = Pco2*Ph2/Pco/Ph2o;
   Pkin3 = Pch4*Ph2o/pow(Ph2,1.75);
   Prev3 = Pco2*pow(Ph2,4.)/Pch4/pow(Ph2o,2.);

   kco = AKco*exp(-delhco/(rgas*cell_temp));
   kh = AKh*exp(-delhh/(rgas*cell_temp));
   kh2o = AKh2o*exp(-delhh2o/(rgas*cell_temp));

   DEN = 1+Pco*kco+pow(Ph2,0.5)*kh+Ph2o/Ph2*kh2o;

   Kp1 = 1.198e17*exp(-26830/(cell_temp));
   Kp2 = 1.767e-2*exp(4400/(cell_temp));
   Kp3 = 2.117e15*exp(-22430/(cell_temp));


   k1 = A1*exp(-E1/(rgas*cell_temp));
   r1 = k1*Pkin1*(1-Prev1/Kp1)/pow(DEN,2.);

   k2 = A2*exp(-E2/(rgas*cell_temp));
   r2 = k2*Pkin2*(1-Prev2/Kp2)/pow(DEN,2.);

   k3 = A3*exp(-E3/(rgas*cell_temp));
   r3 = k3*Pkin3*(1-Prev3/Kp3)/pow(DEN,2.);

   source = rhos*(alph1*r1+alph2*r2+alph3*r3)*Mco;

   dPcodyco = cell_press*(Ysum/Mco-(yco/Mco)/Mco)/Ysum/Ysum;

   dDENdPco = kco;

   dr1dPco = k1*Pkin1*(-1.0*pow(Ph2,3.)/Kp1/Pch4/Ph2o)/pow(DEN,2.)
        -2.0*k1*Pkin1*(1-Prev1/Kp1)/pow(DEN,3.)*dDENdPco;
```

```
    dr2dPco = k2*pow(Ph2o,0.5)/pow(Ph2,0.5)*(1-Prev2/Kp2)/pow(DEN,2.)
          +k2*Pkin2*(Ph2*Pco2)/Kp2/pow(Pco,2.)/Ph2o/pow(DEN,2.)
          -2.0*k2*Pkin2*(1-Prev2/Kp2)/pow(DEN,3.)*dDENdPco;

    dr3dPco = -2.0*k3*Pkin3*(1-Prev3/Kp3)/pow(DEN,3.)*dDENdPco;

    dS[eqn] = rhos*Mco*(alph1*dr1dPco+alph2*dr2dPco+alph3*dr3dPco)*dPcodyco;
   }

 return source;
}

DEFINE_SOURCE(spe_co2, cell, thread, dS, eqn)
{
 real source;
 real kco, kh, kh2o, DEN, k1, Kp1, r1, k2, Kp2, r2, k3, Kp3, r3;
 real Pkin1, Prev1, Pkin2, Prev2, Pkin3, Prev3;
 real dPco2dyco2, dr1dPco2, dr2dPco2, dr3dPco2;
 real cell_temp, cell_press;
 real ych4, yh2, yco, yco2, yh2o, Ysum, Pch4, Ph2, Pco, Pco2, Ph2o;
 real alph1, alph2, alph3;

 cell_temp = C_T(cell, thread);
 cell_press = (Totpress+C_P(cell, thread))/1000.0;
 ych4 = C_YI(cell, thread, 0);
 yh2 = C_YI(cell, thread, 1);
 yco = C_YI(cell, thread, 2);
 yco2 = C_YI(cell, thread, 3);
 yh2o = 1.0-ych4-yh2-yco-yco2;
 Ysum = ych4/Mch4+yco/Mco+yco2/Mco2+yh2/Mh2+yh2o/Mh2o;
 Pch4 = cell_press*ych4/Mch4/Ysum;
 Ph2 = cell_press*yh2/Mh2/Ysum;
 Pco = cell_press*yco/Mco/Ysum;
 Pco2 = cell_press*yco2/Mco2/Ysum;
 Ph2o = cell_press*yh2o/Mh2o/Ysum;

 alph1 = 0.0;
 alph2 = 1.0;
 alph3 = 1.0;

 if (cell_temp <= 550)
    source = dS[eqn] = 0.0;
 else
   {
    Pkin1 = Pch4*pow(Ph2o,0.5)/pow(Ph2,1.25);
    Prev1 = Pco*pow(Ph2,3.)/Pch4/Ph2o;
    Pkin2 = Pco*pow(Ph2o,0.5)/pow(Ph2,0.5);
    Prev2 = Pco2*Ph2/Pco/Ph2o;
    Pkin3 = Pch4*Ph2o/pow(Ph2,1.75);
    Prev3 = Pco2*pow(Ph2,4.)/Pch4/pow(Ph2o,2.);
```

```
    kco = AKco*exp(-delhco/(rgas*cell_temp));
    kh = AKh*exp(-delhh/(rgas*cell_temp));
    kh2o = AKh2o*exp(-delhh2o/(rgas*cell_temp));

    DEN = 1+Pco*kco+pow(Ph2,0.5)*kh+Ph2o/Ph2*kh2o;

    Kp1 = 1.198e17*exp(-26830/(cell_temp));
    Kp2 = 1.767e-2*exp(4400/(cell_temp));
    Kp3 = 2.117e15*exp(-22430/(cell_temp));

    k1 = A1*exp(-E1/(rgas*cell_temp));
    r1 = k1*Pkin1*(1-Prev1/Kp1)/pow(DEN,2.);

    k2 = A2*exp(-E2/(rgas*cell_temp));
    r2 = k2*Pkin2*(1-Prev2/Kp2)/pow(DEN,2.);

    k3 = A3*exp(-E3/(rgas*cell_temp));
    r3 = k3*Pkin3*(1-Prev3/Kp3)/pow(DEN,2.);

    source = rhos*(alph1*r1+alph2*r2+alph3*r3)*Mco2;

    dPco2dyco2 = cell_press*(Ysum/Mco2-(yco2/Mco2)/Mco2)/Ysum/Ysum;

    dr1dPco2 = 0;

    dr2dPco2 = k2*Pkin2*(-1.0*Ph2)/Kp2/Pco/Ph2o/pow(DEN,2.);

    dr3dPco2 = k3*Pkin3*(-1.0*pow(Ph2,4.)/Kp3/Pch4/pow(Ph2o,2.))/pow(DEN,2.);

    dS[eqn] = rhos*Mco2*(alph1*dr1dPco2+alph2*dr2dPco2+alph3*dr3dPco2)*dPco2dyco2;
   }

  return source;
}

DEFINE_SOURCE(q_tdep, cell, thread, dS, eqn)
{
  real source;
  real kco, kh, kh2o, DEN, k1, Kp1, r1, k2, Kp2, r2, k3, Kp3, r3;
  real Pkin1, Prev1, Pkin2, Prev2, Pkin3, Prev3;
  real dk1dt, dKp1dt, dk2dt, dKp2dt, dk3dt, dKp3dt, dDENdt, dr1dt, dr2dt, dr3dt;
  real cell_temp, cell_press;
  real ych4, yh2, yco, yco2, yh2o, Ysum, Pch4, Ph2, Pco, Pco2, Ph2o;

  cell_temp = C_T(cell, thread);
  cell_press = (Totpress+C_P(cell, thread))/1000.0;
  ych4 = C_YI(cell, thread, 0);
  yh2 = C_YI(cell, thread, 1);
  yco = C_YI(cell, thread, 2);
  yco2 = C_YI(cell, thread, 3);
```

```
yh2o = 1.0-ych4-yh2-yco-yco2;
Ysum = ych4/Mch4+yco/Mco+yco2/Mco2+yh2/Mh2+yh2o/Mh2o;
Pch4 = cell_press*ych4/Mch4/Ysum;
Ph2 = cell_press*yh2/Mh2/Ysum;
Pco = cell_press*yco/Mco/Ysum;
Pco2 = cell_press*yco2/Mco2/Ysum;
Ph2o = cell_press*yh2o/Mh2o/Ysum;

if (cell_temp <= 550)
   source = dS[eqn] = 0.0;
else
  {
   Pkin1 = Pch4*pow(Ph2o,0.5)/pow(Ph2,1.25);
   Prev1 = Pco*pow(Ph2,3.)/Pch4/Ph2o;
   Pkin2 = Pco*pow(Ph2o,0.5)/pow(Ph2,0.5);
   Prev2 = Pco2*Ph2/Pco/Ph2o;
   Pkin3 = Pch4*Ph2o/pow(Ph2,1.75);
   Prev3 = Pco2*pow(Ph2,4.)/Pch4/pow(Ph2o,2.);

   kco = AKco*exp(-delhco/(rgas*cell_temp));
   kh = AKh*exp(-delhh/(rgas*cell_temp));
   kh2o = AKh2o*exp(-delhh2o/(rgas*cell_temp));

   DEN = 1+Pco*kco+pow(Ph2,0.5)*kh+Ph2o/Ph2*kh2o;

   Kp1 = 1.198e17*exp(-26830/(cell_temp));
   Kp2 = 1.767e-2*exp(4400/(cell_temp));
   Kp3 = 2.117e15*exp(-22430/(cell_temp));

   k1 = A1*exp(-E1/(rgas*cell_temp));
   r1 = k1*Pkin1*(1-Prev1/Kp1)/pow(DEN,2.);

   k2 = A2*exp(-E2/(rgas*cell_temp));
   r2 = k2*Pkin2*(1-Prev2/Kp2)/pow(DEN,2.);

   k3 = A3*exp(-E3/(rgas*cell_temp));
   r3 = k3*Pkin3*(1-Prev3/Kp3)/pow(DEN,2.);

   source = rhos*(delHr1*r1+delHr2*r2+delHr3*r3);

   dDENdt = Pco*kco*delhco/rgas/cell_temp/cell_temp
         +pow(Ph2,0.5)*kh*delhh/rgas/cell_temp/cell_temp
         +Ph2o/Ph2*kh2o*delhh2o/rgas/cell_temp/cell_temp;

   dk1dt = k1*E1/rgas/cell_temp/cell_temp;
   dk2dt = k2*E2/rgas/cell_temp/cell_temp;
   dk3dt = k3*E3/rgas/cell_temp/cell_temp;

   dKp1dt = Kp1*26830/cell_temp/cell_temp;
   dKp2dt = Kp2*(-4400)/cell_temp/cell_temp;
   dKp3dt = Kp3*22430/cell_temp/cell_temp;
```

```
    dr1dt = dk1dt*Pkin1*(1-Prev1/Kp1)/pow(DEN,2.)
          +k1*Pkin1*(Prev1/Kp1/Kp1)*dKp1dt/pow(DEN,2.)
          -2*k1*Pkin1*(1-Prev1/Kp1)/pow(DEN,3.)*dDENdt;

    dr2dt = dk2dt*Pkin2*(1-Prev2/Kp2)/pow(DEN,2.)
          +k2*Pkin2*(Prev2/Kp2/Kp2)*dKp2dt/pow(DEN,2.)
          -2*k2*Pkin2*(1-Prev2/Kp2)/pow(DEN,3.)*dDENdt;

    dr3dt = dk3dt*Pkin3*(1-Prev3/Kp3)/pow(DEN,2.)
          +k3*Pkin3*(Prev3/Kp3/Kp3)*dKp3dt/pow(DEN,2.)
          -2*k3*Pkin3*(1-Prev3/Kp3)/pow(DEN,3.)*dDENdt;

    dS[eqn] = rhos*(delHr1*dr1dt+delHr2*dr2dt+delHr3*dr3dt);
   }

 return source;
}
```

(d) for the MSR reaction rate calculation in particle 2

```
include "udf.h"

#define rgas 0.0083144
#define rhos 1947.0
#define delhco -140.0
#define delhh -93.4
#define delhh2o 15.9
#define E1 209.2
#define E2 15.4
#define E3 109.4
#define A1 5.922e8
#define A2 6.028e-4
#define A3 1.093e3
#define delHr1 -206100000.0
#define delHr2 41150000.0
#define delHr3 -165000000.0
#define AKco 5.127e-13
#define AKh 5.68e-10
#define AKh2o 9.251
#define Mco 28.0
#define Mh2 2.0
#define Mh2o 18.0
#define Mch4 16.0
#define Mco2 44.0
#define Totpress 2159000.0

FILE *fp = NULL;

DEFINE_ON_DEMAND(part2)
{
  Domain *d;
  int ID = 13;

  real kco, kh, kh2o, DEN, k1, Kp1, r1, k2, Kp2, r2, k3, Kp3, r3;
  real Pkin1, Prev1, Pkin2, Prev2, Pkin3, Prev3;
  real dPch4dych4, dr1dPch4, dr2dPch4, dr3dPch4;
  real cell_temp, cell_press, cell_vol;
  real ych4, yh2, yco, yco2, yh2o, Ysum, Pch4, Ph2, Pco, Pco2, Ph2o;
  real alph1, alph2, alph3;
  real r1ave, r2ave, r3ave, rch4, vol_tot;
  real x[ND_ND];

  Thread *t;
  cell_t c;

  d = Get_Domain(1);
  t = Lookup_Thread(d, ID);

 fp = fopen("data.txt","w");
```

```
begin_c_loop(c,t)

  {
cell_temp = C_T(c, t);
cell_press = (Totpress+C_P(c, t))/1000.0;
C_CENTROID(x,c,t);
cell_vol = C_VOLUME(c, t);

ych4 = C_YI(c, t, 0);
yh2 = C_YI(c, t, 1);
yco = C_YI(c, t, 2);
yco2 = C_YI(c, t, 3);
yh2o = 1.0-ych4-yh2-yco-yco2;
Ysum = ych4/Mch4+yco/Mco+yco2/Mco2+yh2/Mh2+yh2o/Mh2o;
Pch4 = cell_press*ych4/Mch4/Ysum;
Ph2 = cell_press*yh2/Mh2/Ysum;
Pco = cell_press*yco/Mco/Ysum;
Pco2 = cell_press*yco2/Mco2/Ysum;
Ph2o = cell_press*yh2o/Mh2o/Ysum;

alph1 = -1.0;
alph2 = 0.0;
alph3 = -1.0;

   Pkin1 = Pch4*pow(Ph2o,0.5)/pow(Ph2,1.25);
   Prev1 = Pco*pow(Ph2,3.)/Pch4/Ph2o;
   Pkin2 = Pco*pow(Ph2o,0.5)/pow(Ph2,0.5);
   Prev2 = Pco2*Ph2/Pco/Ph2o;
   Pkin3 = Pch4*Ph2o/pow(Ph2,1.75);
   Prev3 = Pco2*pow(Ph2,4.)/Pch4/pow(Ph2o,2.);

   kco = AKco*exp(-delhco/(rgas*cell_temp));
   kh = AKh*exp(-delhh/(rgas*cell_temp));
   kh2o = AKh2o*exp(-delhh2o/(rgas*cell_temp));

   DEN = 1+Pco*kco+pow(Ph2,0.5)*kh+Ph2o/Ph2*kh2o;

   Kp1 = 1.198e17*exp(-26830/(cell_temp));
   Kp2 = 1.767e-2*exp(4400/(cell_temp));
   Kp3 = 2.117e15*exp(-22430/(cell_temp));

   k1 = A1*exp(-E1/(rgas*cell_temp));
   r1 = k1*Pkin1*(1-Prev1/Kp1)/pow(DEN,2.);

   k2 = A2*exp(-E2/(rgas*cell_temp));
   r2 = k2*Pkin2*(1-Prev2/Kp2)/pow(DEN,2.);

   k3 = A3*exp(-E3/(rgas*cell_temp));
   r3 = k3*Pkin3*(1-Prev3/Kp3)/pow(DEN,2.);
```

```
      vol_tot += C_VOLUME(c,t);

      r1ave += r1*cell_vol;
      r2ave += r2*cell_vol;
      r3ave += r3*cell_vol;
      }
  end_c_loop(c,t)
  fclose(fp);

      r1ave /= vol_tot;
      r2ave /= vol_tot;
      r3ave /= vol_tot;

      rch4 = r1ave+r3ave;
     printf("%15e %15e %15e\n", r3ave, r2ave, r1ave);
}
```

(e) for the diffusion/reaction application of PDH

```
#include "udf.h"

#define rgas 8.3144
#define rhos 1000.0
#define ka 9.94
#define kb 72000
#define KA 16.749
#define KB 130000
#define delH -124300000.0
#define Mc3h8 44.0
#define Mc3h6 42.0
#define Mh2 2.0
#define Totpress 101500.0



DEFINE_SOURCE(spe_c3h6, cell, thread, dS, eqn)
{
 real source;
 real k, Ke, r;
 real dPc3h6dyc3h6, drdPc3h6;
 real cell_temp, cell_press;
 real yc3h8, yc3h6, yh2, Ysum, Pc3h8, Pc3h6, Ph2;

 cell_temp = C_T(cell, thread);
 cell_press = (Totpress+C_P(cell, thread))/1000.0;

 yc3h6 = C_YI(cell, thread, 0);
 yh2 = C_YI(cell, thread, 1);
 yc3h8 = C_YI(cell, thread, 2);
 Ysum = yc3h6/Mc3h6+yh2/Mh2+yc3h8/Mc3h8;

 Pc3h6 = cell_press*yc3h6/Mc3h6/Ysum;
 Ph2 = cell_press*yh2/Mh2/Ysum;
 Pc3h8 = cell_press*yc3h8/Mc3h8/Ysum;

 if (cell_temp <= 550)
    source = dS[eqn] = 0.0;
 else
   {
    k = exp(ka - kb/(rgas*cell_temp));
    Ke = cell_press/(rgas*cell_temp)*exp(KA - KB/(rgas*cell_temp));

    r = k*(Pc3h8/rgas/cell_temp - Pc3h6*Ph2/(rgas*rgas*cell_temp*cell_temp*Ke));

     source = r*Mc3h6;

    dPc3h6dyc3h6 = cell_press*(Ysum/Mc3h6-(yc3h6/Mc3h6)/Mc3h6)/Ysum/Ysum;
```

```
    drdPc3h6 = -k*Ph2/(Ke*rgas*rgas*cell_temp*cell_temp);

    dS[eqn] = Mc3h6*drdPc3h6*dPc3h6dyc3h6;
   }

 return source;
}

DEFINE_SOURCE(spe_h2, cell, thread, dS, eqn)
{
 real source;
 real k, Ke, r;
 real dPh2dyh2, drdPh2;
 real cell_temp, cell_press;
 real yc3h8, yc3h6, yh2, Ysum, Pc3h8, Pc3h6, Ph2;

 cell_temp = C_T(cell, thread);
 cell_press = (Totpress+C_P(cell, thread))/1000.0;

 yc3h6 = C_YI(cell, thread, 0);
 yh2 = C_YI(cell, thread, 1);
 yc3h8 = C_YI(cell, thread, 2);
 Ysum = yc3h6/Mc3h6+yh2/Mh2+yc3h8/Mc3h8;

 Pc3h6 = cell_press*yc3h6/Mc3h6/Ysum;
 Ph2 = cell_press*yh2/Mh2/Ysum;
 Pc3h8 = cell_press*yc3h8/Mc3h8/Ysum;

 if (cell_temp <= 550)
    source = dS[eqn] = 0.0;
 else
   {
    k = exp(ka - kb/(rgas*cell_temp));
    Ke = cell_press/(rgas*cell_temp)*exp(KA - KB/(rgas*cell_temp));

    r = k*(Pc3h8/rgas/cell_temp - Pc3h6*Ph2/(rgas*rgas*cell_temp*cell_temp*Ke));

     source = r*Mh2;

    dPh2dyh2 = cell_press*(Ysum/Mh2-(yh2/Mh2)/Mh2)/Ysum/Ysum;

    drdPh2 = -k*Pc3h6/(Ke*rgas*rgas*cell_temp*cell_temp);

    dS[eqn] = Mh2*drdPh2*dPh2dyh2;
   }

 return source;
}


DEFINE_SOURCE(q_tdep, cell, thread, dS, eqn)
```

```
{
 real source;
 real k, Ke, r;
 real dkdt, dKedt, drdt;
 real cell_temp, cell_press;
 real yc3h8, yc3h6, yh2, Ysum, Pc3h8, Pc3h6, Ph2;
 real rgs, cts;

 cell_temp = C_T(cell, thread);
 cell_press = (Totpress+C_P(cell, thread))/1000.0;

 yc3h6 = C_YI(cell, thread, 0);
 yh2 = C_YI(cell, thread, 1);
 yc3h8 = C_YI(cell, thread, 2);
 Ysum = yc3h6/Mc3h6+yh2/Mh2+yc3h8/Mc3h8;

 Pc3h6 = cell_press*yc3h6/Mc3h6/Ysum;
 Ph2 = cell_press*yh2/Mh2/Ysum;
 Pc3h8 = cell_press*yc3h8/Mc3h8/Ysum;

  if (cell_temp <= 550)
    source = dS[eqn] = 0.0;
 else
   {
     k = exp(ka - kb/(rgas*cell_temp));
    Ke = cell_press/(rgas*cell_temp)*exp(KA - KB/(rgas*cell_temp));

    r = k*(Pc3h8/rgas/cell_temp - Pc3h6*Ph2/(rgas*rgas*cell_temp*cell_temp*Ke));

     source = delH*r;

    dkdt = k*kb/rgas/cell_temp/cell_temp;

    dKedt = Ke*(KB/rgas/cell_temp/cell_temp-1/cell_temp);

    rgs = rgas*rgas;
    cts = cell_temp*cell_temp;

   drdt = dkdt*(Pc3h8/rgas/cell_temp - Pc3h6*Ph2/(rgs*cts*Ke))-k*(Pc3h8/(rgas*cts)-
2*Pc3h6*Ph2/(rgs*cts*cell_temp*Ke)+Pc3h6*Ph2/(rgs*cts*Ke*Ke)*dKedt);

    dS[eqn] = delH*drdt;
   }

 return source;
}
```

Appendix 4: Mesh structures of the WS models used in diffusion /reaction application

Table A.3 full cylinders packing grid details

	1st prism height x10^3 (m)	*b/a**	Number of layers	Total prism height x10^3 (m)	UNS x10^3 (m)
Fluid side					0.7620
Particle 1	0.0254	1.2	3	0.09246	
Particle 2	0.0254	1.2	3	0.09246	
Particle 3	0.0254	1.2	3	0.09246	
Particle 4	0.0254	1.2	3	0.09246	
Particle 5	0.0254	1.2	3	0.09246	
Particle 6	0.0254	1.0	3	0.07620	
Particle 7	0.0254	1.0	3	0.07620	
Particle 8	0.0254	1.2	2	0.05588	
Particle 9	0.0254	1.2	3	0.09246	
Particle 10	0.0254	1.0	3	0.07620	
Particle 11	0.0254	1.0	3	0.07620	
Particle 12	0.0254	1.0	3	0.07620	
Tube wall	0.0254	1.2	4	0.13635	
Solid side (all particles)	0.0762	1.2	4	0.40904	0.7620

* The *b/a* represents the growth factor where *b* is the distance between the first and second rows at a given edge node, and *a* is the height of the first row at the node. The distance between any two rows in the boundary layer at a given edge node is equal to the distance between the preceding two rows times the growth factor.

Table A.4 4-holel cylinders packing grid details

	1st prism height x10^3 (m)	*b/a*	Number of layers	Total prism height x10^3 (m)	UNS x10^3 (m)
Fluid side					0.7620
Particle 1	0.0254	1.0	2	0.05080	
Particle 2	0.0254	1.0	3	0.07620	
Particle 3	0.0254	1.0	2	0.05080	
Particle 4	0.0254	1.0	2	0.05080	
Particle 5	0.0254	1.0	2	0.05080	
Particle 6	0.0254	1.0	1	0.02540	
Particle 7	0.0254	1.0	1	0.02540	
Particle 8	0.0254	1.0	1	0.02540	
Particle 9	0.0254	1.0	3	0.09246	
Particle 10	-	-	-	-	
Particle 11	-	-	-	-	
Particle 12	0.0254	1.0	2	0.07620	
Tube wall	0.0254	1.2	4	0.13635	
Solid side					
Particle 2	0.127	1.0	6	0.762	0.5588
Particle 10	-	-	-	-	0.3302
Particle 11	-	-	-	-	0.3302
All others	-	-	-	-	0.7620

Appendix 5: Effective diffusivity calculations

(a) Methane steam reforming reaction:

Mole fractions:

$y_{CH4} = 0.2392$ $y_{H2} = 0.005$ $y_{CO} = 0.0005$ $y_{CO2} = 0.0776$ $y_{CH4} = 0.6777$

For the inlet operating conditions, the dominant reaction is:

$$CH_4 + 2H_2O \Leftrightarrow CO_2 + 4H_2 \qquad \text{(A-5. 1)}$$

Binary diffusivities may be calculated by the expression introduced by Fuller, Schettler, and Giddings (1966):

$$D_{AB} = \frac{0.001T^{1.75}[(M_A + M_B)/(M_A M_B)]^{0.5}}{P[(\sum v)_A^{1/3} + (\sum v)_B^{1/3}]^2} \qquad \text{cm}^2/\text{s} \qquad \text{(A-5. 2)}$$

where T = 824.15 K, and P = 21.3 atm. The molecular weight of components, M_A, and, the molecular volumes of the components, $(\sum v)_A$, are given in Table A.5.

Table A.5 Molecular volumes, and molecular weights of components, MSR reaction

Species	$(\sum v)_i$	M_i
CH_4	24.42	16
H_2	7.07	2
CO	18.9	28
CO_2	26.9	44
H_2O	12.7	18

The calculated binary diffusivities according to equation (A.2) are given in Table A.6.

Table A.6 Binary diffusivities for MRS reaction (cm^2/s)

	H_2	CO	CO_2	H_2O
CH_4	0.192	0.060	0.050	0.075
H_2		0.208	0.178	0.246
CO			0.045	0.072
CO_2				0.059

The Knudsen diffusivity can be calculated with the following equation:

$$D_{K,A} = 9.70\times10^3 \overline{r_p}\left(\frac{T}{M_A}\right)^{0.5} \qquad \text{cm}^2/\text{s} \qquad \text{(A-5. 3)}$$

where the average pore radius, $\overline{r_p}$, was taken as 10^3 $\overset{o}{A}$ (Hou and Hughes, 2001). The calculated Knudsen diffusivities were:

$D_{K,CH4} = 0.696$ $D_{K,H2} = 1.969$ $D_{K,CO} = 0.526$ $D_{K,CO2} = 0.420$ $D_{K,H2O} = 0.656$

Molecular diffusivities can be calculated with the following equation:

$$\frac{1}{D_{A,md}} = \frac{\sum_{K=1}^{N}\frac{1}{D_{A,K}}(y_K - y_A\frac{N_K}{N_A})}{1 - y_A\sum_{K=1}^{N}\frac{N_K}{N_A}} \qquad \text{(A-5. 4)}$$

The calculated molecular diffusivities were:

$D_{CH4,md} = 0.123$ cm^2/s [$N_{H2}/N_{CH4} = -4$, $N_{CO}/N_{CH4} = 0$, $N_{CO2}/N_{CH4} = -1$, $N_{H20}/N_{CH4} = 2$]

$D_{H2,md} = 0.225$ cm^2/s [$N_{CH4}/N_{H2} = -1/4$, $N_{CO}/N_{H2} = 0$, $N_{CO2}/N_{H2} = 1/4$, $N_{H20}/N_{H2} = -1/2$]

$D_{CO2,md} = 0.049$ cm^2/s [$N_{CH4}/N_{CO2} = -1$, $N_{CO}/N_{CH4} = 0$, $N_{H2}/N_{CO2} = 4$, $N_{H20}/N_{CO2} = -2$]

$D_{H2O,md} = 0.209$ cm^2/s [$N_{CH4}/N_{H2O} = -4$, $N_{CO}/N_{H2O} = 0$, $N_{CO2}/N_{H2O} = -1/2$, $N_{H2}/N_{H2O} = -2$]

CO is not in the reaction. Therefore, $N_{CO} = 0$. So, $D_{CO,H20} = 0.072$ was used for $D_{CO,md.}$

Effective diffusivities were calculated by : $1/D_A = 1/D_{A,md} + 1/D_{K,A}$, and corrected using the pellet tortuosity and porosity as:

$$D_{A,eff} = \frac{\varepsilon}{\tau} D_A \qquad \text{cm}^2/\text{s} \qquad \text{(A-5. 5)}$$

where $\varepsilon = 0.44$ (Hou and Hughes, 2001), and $\tau = 3.54$ (Xu and Froment, 1989b). The effective diffusivities were:

$D_{CH4,eff} = 1.3 \times 10^{-6}$ m^2/s
$D_{H2,eff} = 2.5 \times 10^{-6}$ m^2/s
$D_{CO,eff} = 8.0 \times 10^{-7}$ m^2/s
$D_{CO2,eff} = 5.0 \times 10^{-7}$ m^2/s
$D_{H2O,eff} = 2.0 \times 10^{-6}$ m^2/s

(b) Propane dehydrogenation reaction:

Mole fractions:

$y_{C3H8} = 0.4385$ $y_{H2} = 0.5360$ $y_{C3H6} = 0.0255$

The reaction is:

$$C_3H_8 \Leftrightarrow C_3H_6 + H_2 \qquad \text{(A-5. 6)}$$

The molecular volumes and molecular weights of the compounds are given in Table A.7.

Table A.7 Molecular volumes, and molecular weights of components, PDH reaction

Species	$(\sum v)_i$	M_i
C_3H_8	65.34	44
H_2	7.07	2
C_3H_6	61.38	42

Operating T = 874.15 K, and P = 1.0 atm. The calculated binary diffusivities according to equation (A.2) are given in Table A.8.

Table A.8 Binary diffusivities for PDH reaction (cm^2/s)

	H_2	C_3H_6
C_3H_8	2.873	0.477
H_2		2.958

The Knudsen diffusivities were calculated with equation (A.3) with the average pore radius, $\overline{r_p} = 10^3 \ \mathring{A}$ (Hou and Hughes, 2001). The calculated Knudsen diffusivities were:

$D_{K,C3H8} = 0.432 \quad D_{K,H2} = 2.028 \quad D_{K,C3H6} = 0.443 \ \ (cm^2/s)$

Molecular diffusivities were be calculated with equation (A.4) and found to be:

$D_{C3H8,md} = 1.431 \ cm^2/s$ [$N_{C3H8}/N_{C3H6} = -1$, $N_{C3H8}/N_{H2} = -1$]

$D_{H2,md} = 6.002 \ cm^2/s$ [$N_{H2}/N_{C3H8} = -1$, $N_{H2}/N_{C3H6} = 1$]

$D_{C3H6,md} = 0.873 \ cm^2/s$ [$N_{C3H6}/N_{C3H8} = -1$, $N_{C3H6}/N_{H2} = 1$]

Effective diffusivities were calculated by: $1/D_A = 1/D_{A,md} + 1/D_{K,A}$, and corrected equation (A.5) using the same pellet tortuosity and porosity values as used for MRS reaction. The effective diffusivities were:

$D_{C3H8,eff} = 4.127 \times 10^{-6} \ m^2/s$

$D_{H2,eff} = 1.884 \times 10^{-5} \ m^2/s$

$D_{C3H6,eff} = 3.650 \times 10^{-6} \ m^2/s$

Appendix 6: Monitoring the convergence in diffusion/reaction simulations

(a) MSR reaction full cylinders model

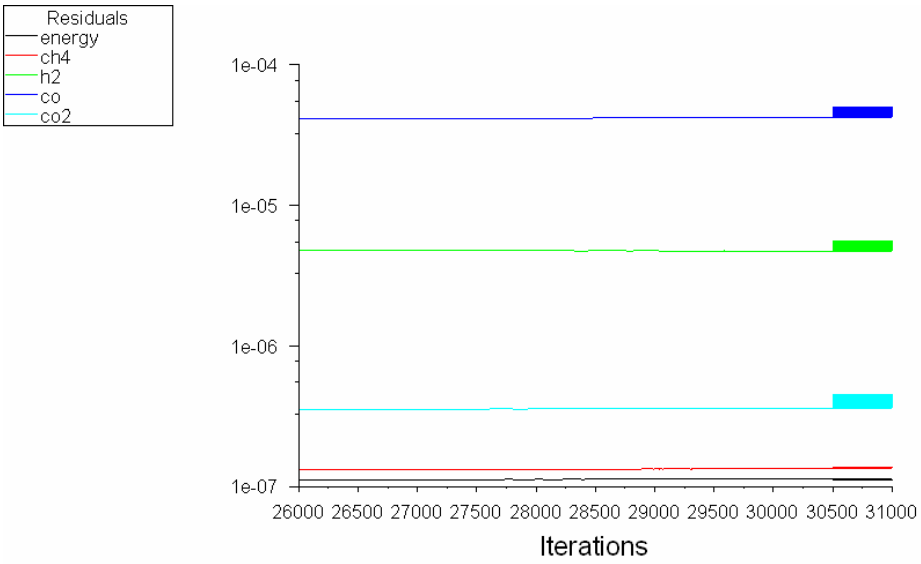

Figure A.1 MRS, full cylinders model residuals plot

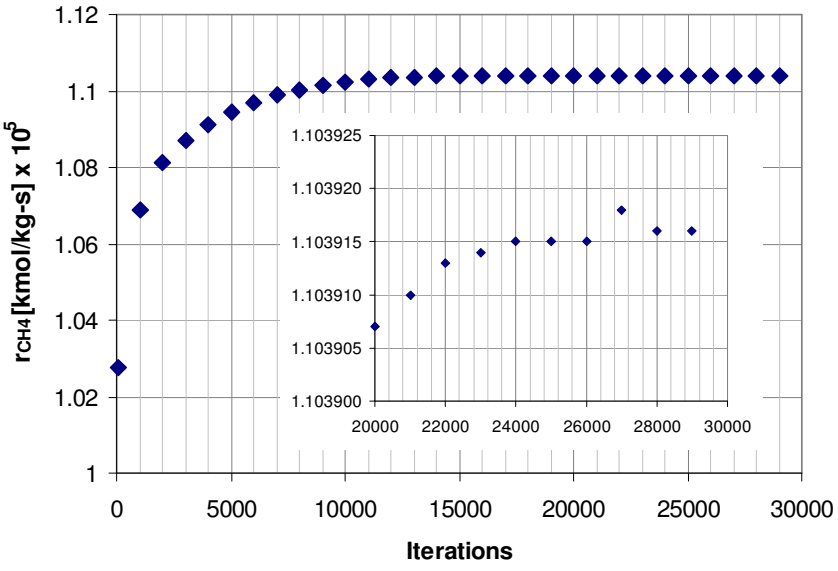

Figure A.2 MSR, full cylinders model CH_4 consumption rate plot

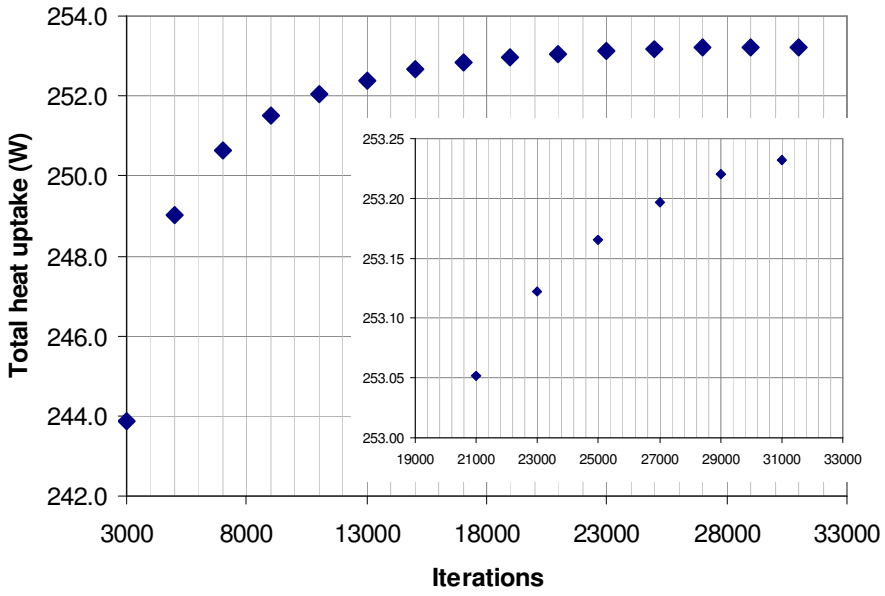

Figure A.3 MSR, full cylinders model total heat uptake plot

(b) MSR reaction, 4-hole cylinders model

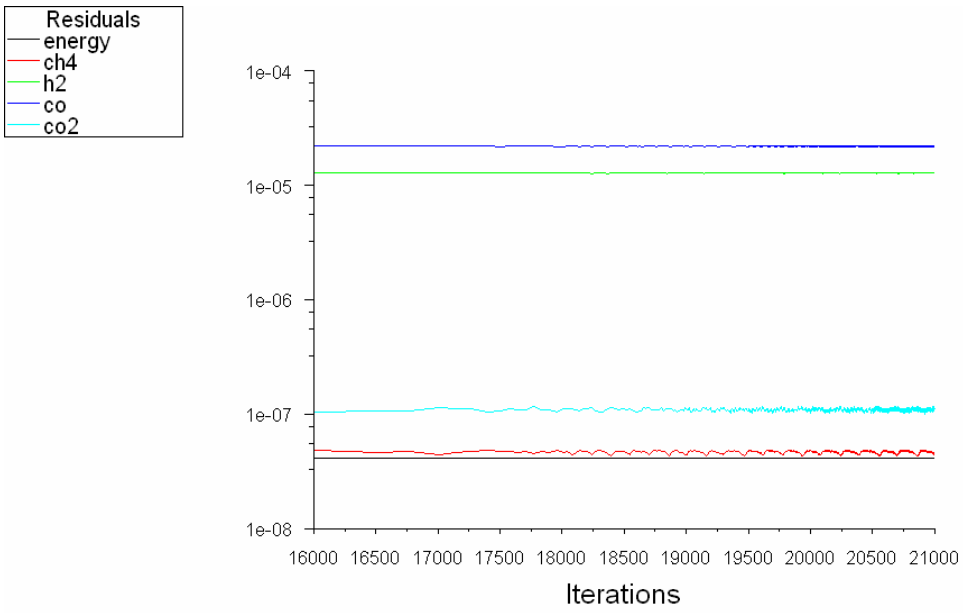

Figure A.4 MRS, 4-hole cylinders model residuals plot

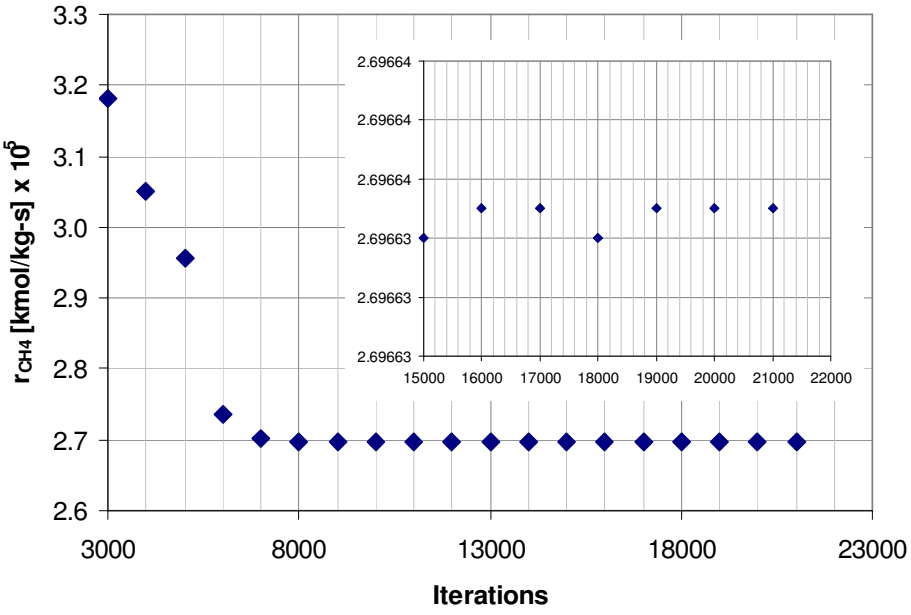

Figure A.5 MSR, 4-hole cylinders model CH_4 consumption rate plot

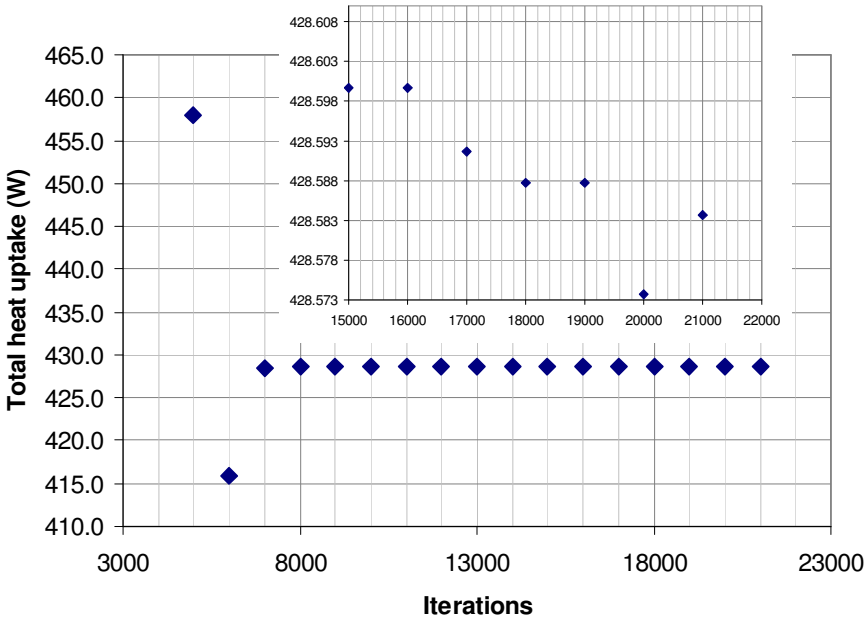

Figure A.6 MSR, 4-hole cylinders model total heat uptake plot

Appendix 7: Correlations

(a) Axial velocity, v_z:

Tsotsas and Schlunder (1988)

$$\frac{u}{u_0} = \beta\left\{1-\exp\left[aR^*\left(1-\frac{r}{r_t}\right)\right]\left[1-nR^*\left(1-\frac{r}{r_t}\right)\right]\right\} \qquad \text{(A-7. 1)}$$

)

$$\beta = \frac{R^{*2}}{2}\left[\frac{R^{*2}}{2}-\frac{(nR^*-1)(aR^*+1)}{a^2}+n\left(\frac{R^{*2}}{a}+\frac{2R^*}{a^2}+\frac{2}{a^3}\right)-\frac{\exp(aR^*)}{a^2}\left(1-nR^*+\frac{2n}{a}\right)\right]^{-1} \qquad \text{(A-7. 2)}$$

$$R^* = d_t / d_p \qquad \text{(A-7. 3)}$$

$$a = 4n/(4-n) \qquad \text{(A-7. 4)}$$

$n = 27$ for Re > 1000.

u is the superficial velocity at a radial position r, u_0 is the average superficial velocity, r_t is tube radius, d_t is tube diameter, and d_p is particle diameter.

The above equations were obtained from the extended Brinkman expression which is in the highly nonlinear 2D partial differential form, by minimizing an integral in the region of interest rather than solving the differential equation. The details can be found in the above reference as well as Vortmeyer and Schuster (1983).

User-defined code

```
DEFINE_PROFILE(w_correlation, t, i)
{
   cell_t c;
   real x[ND_ND], r, a, n, beta, Rstar;
   n = 27.0;
   a = -4.696;
   beta = 0.691;
   Rstar = 4.0;
   begin_c_loop(c, t)
```

```
        {
         C_CENTROID(x, c, t);
         r = sqrt(pow(x[0],2)+pow(x[1],2));
         F_PROFILE(c, t, i) = 1.6135*beta*(1-exp(a*Rstar*(1-r/0.0508))*(1-n*Rstar*(1-r/0.0508)));
         }
         end_c_loop(c, t)
}
```

DPM-fitted v_z profile

User-defined code

```
DEFINE_PROFILE(w_vel, t, i)
{
   cell_t c;
   real x[ND_ND], r;
   begin_c_loop(c, t)
    {
     C_CENTROID(x, c, t);
     r = sqrt(pow(x[0],2)+pow(x[1],2));

     if (r < 0.024 && r > 0.0)
          F_PROFILE(c, t, i) =    0.06519580821 - 107.5259898 * r + 39974.32809 * pow(r,2) -
1511078.848 * pow(r,3) + 17341425.55 * pow(r,4);
      else if (r < 0.049 && r > 0.024)
     F_PROFILE(c, t, i) = 2899.277922 - 476087.7234 * r + 32533409.72 * pow(r,2) - 1183163544
* pow(r,3) + 2.413565553E+010 * pow(r,4) - 2.617091926E+011 * pow(r,5) + 1.178111244E+012 *
pow(r,6);
    else if (r < 0.05064 && r > 0.049)
      F_PROFILE(c, t, i) =     58650.66725 - 3550922.107 * r + 71641034.24 * pow(r,2) -
481623231.5 * pow(r,3);
    else if (r < 0.0507 && r > 0.05064)
      F_PROFILE(c, t, i) =    -19821.86269 * r + 1008.305437;
    else if (r < 0.05072 && r > 0.0507)
      F_PROFILE(c, t, i) = -34180.53712 * r + 1736.29023;
    else if (r < 0.05076 && r > 0.05072)
```

```
    F_PROFILE(c, t, i) = -24857.55232 * r + 1263.428442;
  else
    F_PROFILE(c, t, i) =   -41477.14193 * r + 2107.03881;
    }
    end_c_loop(c, t)
}
```

(b) Thermal conductivity, k_{er}:

Dixon correlation (Dixon and Cresswell, 1979; Dixon, 1988)

$$k_{er} = \frac{d_p u_s \rho c_p}{Pe_{er}} \tag{A-7. 5}$$

$$\frac{1}{Pe_{er}} = \frac{1}{Pe_{fr}} + \frac{k_{rs}/k_f}{\mathrm{Re}\cdot\mathrm{Pr}}\left[\frac{Bi_f + 4}{Bi_f}\right]\left[\frac{8}{N_s} + \frac{Bi_s + 4}{Bi_s}\right]^{-1} \quad (\mathrm{Re}>50) \tag{A-7. 6}$$

$$\frac{1}{Pe_{er}} = \frac{1}{Pe_{fr}}\left[\frac{Bi_s + 4}{Bi_s}\right]\left[\frac{8}{N_F} + \frac{Bi_f + 4}{Bi_f}\right]^{-1} + \frac{k_{rs}/k_f}{\mathrm{Re}\cdot\mathrm{Pr}} \quad (\mathrm{Re}<50) \tag{A-7. 7}$$

$$\frac{1}{Pe_{rf}} = \frac{1}{Pe_{rf(\infty)}} + \frac{0.74\varepsilon}{\mathrm{Re}\cdot\mathrm{Pr}} \tag{A-7. 8}$$

$$Pe_{rf(\infty)} = \begin{cases} 12 & spheres \\ 7 & cylinders \\ 6 & hollow\ cylinders \end{cases} \tag{A-7. 9}$$

$$\frac{k_{rs}}{k_f} = \sqrt{1-\varepsilon}\,\frac{2}{M}\left[\frac{B(k_s-1)}{M^2 k_s}\ln\left(\frac{k_s}{B}\right) - \frac{B+1}{2} - \frac{B-1}{M}\right] \tag{A-7. 10}$$

$$M = \frac{k_s - B}{k_s} \qquad k_s = \frac{k_{solid}}{k_f} \qquad B = C\left(\frac{1-\varepsilon}{\varepsilon}\right)^{10/9} \tag{A-7. 11}$$

$$Bi_f = Nu_{wf}\,(d_t / d_{pv})(Pe_{rf}\,/(\mathrm{Re}\,\mathrm{Pr})) \tag{A-7. 12}$$

$$Nu_{fs} = \frac{0.225}{\varepsilon}\,\mathrm{Pr}^{1/3}\,\mathrm{Re}^{0.67} \tag{A-7. 13}$$

$$Nu_{wf} = 0.523(1 - d_{pv}/d_t)\,\mathrm{Pr}^{1/3}\,\mathrm{Re}^{0.738} \tag{A-7. 14}$$

$$Bi_s = \begin{cases} 2.41 + 0.156(d_t/d_{pv} - 1)^2 & spheres \\ 0.48 + 0.192(d_t/d_{pv} - 1)^2 & cylinders \end{cases} \tag{A-7. 15}$$

$$\beta_s = \frac{k_{rs}/k_f}{\dfrac{8}{N_s} + \dfrac{Bi_s + 4}{Bi_s}} \tag{A-7. 16}$$

$$N_s = \frac{0.25(1-\varepsilon)\dfrac{A_p}{V_p}\dfrac{d_t^2}{d_{pv}}}{k_{rs}/k_f\left[\dfrac{1}{Nu_{fs}} + \dfrac{1}{\beta}\dfrac{k_f}{k_{solid}}\right]} \tag{A-7. 17}$$

$$N_F = \frac{0.25(1-\varepsilon)\dfrac{A_p}{V_p}\dfrac{d_t^2}{d_{pv}}}{\dfrac{\mathrm{Re}\,\mathrm{Pr}}{Pe_{rf}}\left[\dfrac{1}{Nu_{fs}} + \dfrac{1}{\beta}\dfrac{k_f}{k_{solid}}\right]} \tag{A-7. 18}$$

$$\beta = \begin{cases} 10 & spheres \\ 8 & cylinders \end{cases} \tag{A-7. 19}$$

$$C = \begin{cases} 1.25 & spheres \\ 2.5 & cylinders \end{cases} \tag{A-7. 20}$$

Bauer and Schlunder correlation (1978a, 1978b)

$$\frac{k_{er}}{k_f} = \frac{k_{convection}}{k_f} + \frac{k_{conduction,radiation}}{k_f} \tag{A-7. 21}$$

$$\frac{k_{convection}}{k_f} = \frac{\rho u_s c_p}{k_f} \frac{X_F}{8\left[2-\left(1-2d_{pv}/d_t\right)^2\right]} \tag{A-7. 22}$$

$$\frac{k_{conduction,radiation}}{k_f} = (1-\sqrt{1-\varepsilon})\left(1+\varepsilon\frac{k_{radiation}}{k_f}\right) + \sqrt{1-\varepsilon}\left(\frac{k_{rs}}{k_f}\right) \tag{A-7. 23}$$

$$\frac{k_{radiation}}{k_f} = 2.27\times10^{-7}\frac{e}{2-e}T^3\frac{d_{pv}}{k_f} \tag{A-7. 24}$$

$$\frac{k_{rs}}{k_f} = \frac{2}{N}\left[\frac{B(k_s+k_r-1)}{N^2k_s}\ln\left(\frac{k_s+k_r}{B}\right) + \frac{B+1}{2B}(k_r-B) - \frac{B-1}{N}\right] \tag{A-7. 25}$$

$$N = \frac{k_s+k_r-B}{k_s} \qquad B = C\left(\frac{1-\varepsilon}{\varepsilon}\right)^{10/9} \tag{A-7. 26}$$

$$k_s = \frac{k_{solid}}{k_f} \qquad k_s = \frac{k_{radiation}}{k_f} \tag{A-7. 27}$$

X_F is the effective mixing length, $X_F = Fd_{pv}$

e is emmisivity

$$F = \begin{cases} 1.15 & spheres \\ 1.75 & cylinders \end{cases} \tag{A-7. 28}$$

$$C = \begin{cases} 1.25 & spheres \\ 2.5 & cylinders \end{cases} \tag{A-7. 29}$$

Winterberg and Tsotsas correlation (2000)

$$k_{er}(r) = k_{bed}(r) + K_1 Pe_0 \frac{u_c}{u_0} f(r_t - r) k_f \qquad \text{(A-7. 30)}$$

$$f(r_t - r) = \begin{cases} \left(\dfrac{r_t - r}{K_2 dp} \right)^2 & for\ 0 \le r_t - r \le K_2 dp \\ 1 & for\ K_2 dp < r_t - r \le r_t \end{cases} \qquad \text{(A-7. 31)}$$

u_c is the superficial velocity at the core of the bed, and k_{bed} is the effective thermal conductivity without fluid flow. $k_{bed}(r)$ was obtained from full cylinders WS model averaging the thermal conductivity vales of fluid and solid regions on the radial planes. By the polynomial functions, k_{bed} was re-produced, and utilized.

Recommended $K_1 = 0.16$, $K_2 \approx 0.40$ for high Re.

The used K_1 and K_2 values:

Section 6.2,	Case-3(a)	$K_1 = 0.16$, $K_2 = 0.40$
	Case-3(b)	$K_1 = 0.10$, $K_2 = 0.50$
	Case-3(c)	$K_1 = 0.20$, $K_2 = 0.10$
	Case-4(a)	$K_1 = 0.16$, $K_2 = 0.40$
	Case-4(b)	$K_1 = 0.10$, $K_2 = 0.40$
	Case-4(c)	$K_1 = 0.20$, $K_2 = 0.20$
Section 6.3,	P-C (1)	$K_1 = 0.16$, $K_2 = 0.13$
	P-C (2)	$K_1 = 0.16$, $K_2 = 0.70$
	P-C (3)	$K_1 = 0.16$, $K_2 = 0.01$

User-defined code

```
DEFINE_PROPERTY(k_eff_corr, c, t)
{
 real lambda, epsilon, lambda_bed;
 real x[ND_ND], r, K1, K2, fRr, B;
```

```
C_CENTROID(x, c, t);
r = sqrt(pow(x[0],2)+pow(x[1],2));
if (r < 0.0225 && r > 0.0)
    lambda_bed = 0.8909162768+8.085091273*r-2782.777489*pow(r,2)+74084.89133*pow(r,3)-
1207081.61*pow(r,4);
else if (r < 0.0505 && r > 0.0225)
    lambda_bed = 2.455137547-1289.139629*r+124089.7465*pow(r,2)-
4726488.002*pow(r,3)+81043504.61*pow(r,4)-523908173.5*pow(r,5);
else
    lambda_bed = 0.0876;
K1 = 0.16;
K2 = 0.05;
fRr = (0.0508-r)/(K2*0.029);
B = 0.0508-K2*0.029;
if (r <= 0.0508 && r>= B)
    lambda = lambda_bed+K1*7883.7*0.33/1.6135*fRr*0.0876;
else
    lambda = lambda_bed+K1*7883.7*0.33/1.6135*1*0.0876;
return lambda;
}
```

(c) Effective diffusivity, D_{er} :

Specia et al. correlation (1980)

$$D_{er} = \frac{u_s dp}{8.65\left[1+19.4\left(\frac{dp}{d_t}\right)^2\right]} \qquad \text{(A-7. 32)}$$

Bauer and Schlunder correlation (1978)

$$D_{er} = \frac{u_s X_F}{8\left[2-(1-2d_{pv}/d_t)^2\right]} \qquad \text{(A-7. 33)}$$

X_F is the effective mixing length, $X_F = Fd_{pv}$

$$F = \begin{cases} 1.15 & spheres \\ 1.75 & cylinders \end{cases} \qquad \text{(A-7. 34)}$$

Rase correlation (1990)

$$D_{er} = \frac{u_s dp}{\varepsilon}\left(\frac{1}{m}+\frac{0.38}{\mathrm{Re}}\right) \qquad \text{for } dp/d_t > 0.1 \qquad \text{(A-7.35)}$$

$$D_{er} = \frac{u_s dp}{\varepsilon}\left(\frac{1}{m}+\frac{0.38}{\mathrm{Re}}\right)\Big/\left[1+19.4\left(\frac{dp}{d_t}\right)^2\right] \qquad \text{for } dp/d_t < 0.1 \qquad \text{(A-7. 36)}$$

$$m = \begin{cases} 11 & \mathrm{Re} > 400 \\ 57.85 - 35.36\log \mathrm{Re} + 6.68(\log \mathrm{Re})2 & 20 < \mathrm{Re} < 400 \end{cases} \qquad \text{(A-7. 37)}$$

DPM-fitted D_{er}

User-defined code

```
DEFINE_PROPERTY(D_effective, c, t)
{
  real D;
  real x[ND_ND], r;
```

```
C_CENTROID(x, c, t);
r = sqrt(pow(x[0],2)+pow(x[1],2));
    if (r < 0.015 && r > 0.0)
      D = 1.196112713E-005 - 0.001466495288 * r - 0.4915808717 * pow(r,2) + 91.48866752 *
pow(r,3) - 2476.890131 * pow(r,4) - 26135.46626 * pow(r,5);
     else if (r < 0.0275 && r > 0.015)
      D = 0.0008337534968 - 0.1783691592 * r + 14.49173144 * pow(r,2) - 500.293758 * pow(r,3) +
6176.32268 * pow(r,4);
     else if (r < 0.046 && r > 0.0275)
      D = 0.00360563988 - 0.4129531021 * r + 17.74026682 * pow(r,2) - 338.0363024 * pow(r,3) +
2414.242821 * pow(r,4);
     else if (r < 0.05 && r > 0.046)
      D = 0.2597300077 - 15.95463436 * r + 325.8040534 * pow(r,2) - 2210.511931 * pow(r,3);
     else if (r < 0.0504 && r > 0.05)
      D =  1.735095509 - 68.86031822 * r + 683.2454095 * pow(r,2);
    else if (r < 0.0506 && r > 0.0504)
     D =  -0.1447889841 * r + 0.007385494923;
     else if (r < 0.05072 && r > 0.0506)
      D = -0.4564763148 * r + 0.0231567335;
     else if (r < 0.05074 && r > 0.05072)
      D = 4.96e-6;
     else if (r < 0.05076 && r > 0.05074)
      D = -0.1463608966 * r + 0.00743130848;
     else if (r < 0.05078 && r > 0.05076)
      D = -0.02155790996 * r + 0.00109630888;
     else
      D = 1.6e-6;
    return D;}
```

(d) Bed voidage profile, $\varepsilon(r)$:

Winterberg and Tsotsas correlation (2000)

$$\varepsilon(r) = \varepsilon_{\infty}\left(1 + A\exp\left[-B\frac{r_t - r}{d_{pv}}\right]\right) \quad \text{(A-7. 38)}$$

$$A = \frac{0.65}{\varepsilon_{\infty}} - 1 \text{ and } B = 6.0 \quad \text{(A-7. 39)}$$

ε_{∞} is voidage of the infinitely extended bed which was set to 0.1 based on the observations in DPM.

Bey and Eigenberger (2000)

Two different expressions have used for near wall region and bed core.

$$\varepsilon_{wall}(r) = \varepsilon_{\min,C} + (1 - \varepsilon_{\min,C})(r')^4 \qquad \text{for } r' < 0 \quad \text{(A-7. 40)}$$

$$\varepsilon_{core}(r) = \varepsilon_{0,C} + (\varepsilon_{\min,C} - \varepsilon_{0,C})\exp\left(-\frac{r'}{c}\right)\cos\left(\frac{\pi}{b}r'\right) \quad \text{for } r' \geq 0 \quad \text{(A-7. 41)}$$

$$r' = a_0\frac{r_t - r}{dp_{eq}} - 1, \qquad a_0 = 1.8 - 2\frac{dp}{dt} - 1, \quad \text{b} = 0.876, \qquad \text{c} = 2 \quad \text{(A-7. 42)}$$

DPM-fitted $\varepsilon(r)$

User-defined code

```
if (r < 0.0504 && r > 0.0225)
    epsilon = -225.073+40524.003*r-2939272.509*pow(r,2)+110717936.25*pow(r,3)-
2293882086.17*pow(r,4)+24853102253.985*pow(r,5)-110180930973.904*pow(r,6);
  else if (r < 0.0225 && r > 0.0)
    epsilon = 0.052463+28.00127*r-23580.3522*pow(r,2)+5594741.763*pow(r,3)-
475768235.634*pow(r,4)+17863076450.73*pow(r,5)-251062548976.676*pow(r,6);
  else
    epsilon = 1.0;
```